

MBE GROWTH OF NITRIDE-ARSENIDES FOR LONG
WAVELENGTH OPTO-ELECTRONICS

A DISSERTATION
SUBMITTED TO THE DEPARTMENT OF MATERIALS SCIENCE AND
ENGINEERING
AND THE COMMITTEE ON GRADUATE STUDIES
OF STANFORD UNIVERSITY
IN PARTIAL FULFILLMENT OF THE REQUIREMENTS
FOR THE DEGREE OF
DOCTOR OF PHILOSOPHY

Sylvia Gabrielle Spruytte

April 2001

© Copyright by Sylvia Spruytte 2001
All rights Reserved

I certify that I have read this dissertation and that in my opinion it is fully adequate, in scope and quality, as a dissertation for the degree of Doctor of Philosophy.

James S. Harris, Jr.
(Principal Adviser)

I certify that I have read this dissertation and that in my opinion it is fully adequate, in scope and quality, as a dissertation for the degree of Doctor of Philosophy.

Charles B. Musgrave

I certify that I have read this dissertation and that in my opinion it is fully adequate, in scope and quality, as a dissertation for the degree of Doctor of Philosophy.

William D. Nix

Approved for the University Committee on Graduate Studies:

Abstract

Until recently, the operating wavelength of opto-electronic devices on GaAs has been limited to below 1 μm due to the lack of III-V materials with close lattice match to GaAs that have a bandgap below 1.24 eV. To enable devices operating at 1.3 μm on GaAs, MBE growth of a new III-V material formed by adding small amounts of nitrogen to InGaAs was developed. The role of nitrogen is two fold: the nitrogen causes the bulk bandgap to decrease dramatically and the smaller lattice constant of GaN results in less strain in GaInNAs compared to InGaAs.

The growth of group III-nitride-arsenides (GaInNAs) is complicated by the divergent properties of the alloy constituents and the difficulty of generating a reactive nitrogen species. Nitride-arsenide materials are grown by molecular beam epitaxy (MBE) using a radio frequency (rf) nitrogen plasma source. The plasma conditions that maximize the amount of atomic nitrogen versus molecular nitrogen are determined using the emission spectrum of the plasma. To avoid phase segregation, nitride-arsenides must be grown at relatively low temperatures and high arsenic overpressures. It is shown that the group III growth rate controls the nitrogen concentration in the film.

Absorption measurements allow the establishment of a range of GaInNAs alloys yielding 1.3 μm emission. The optical properties of GaInNAs and GaNAs quantum wells (QWs) are investigated with photoluminescence (PL) measurements. The peak PL intensity increases and peak wavelength shifts to shorter wavelengths when annealing. Device quality material is obtained only after a rapid thermal anneal at 760 $^{\circ}\text{C}$ for 1 min. The increase in luminescence efficiency results from a decrease in non-radiative recombination centers. As the impurity concentration in the GaInNAs films is low, crystal defects associated with nitrogen incorporation were investigated and

improvements in crystal quality after anneal were observed. Nuclear reaction channeling measurements show that as-grown nitride-arsenides contain a considerable amount of interstitial nitrogen and that a substantial fraction of the non-substitutional nitrogen disappears during anneal. Secondary ion mass spectroscopy depth profiling on GaInNAs quantum wells shows that during anneal, the nitrogen diffusion is more pronounced than indium diffusion, hence nitrogen diffusion is also the major cause of the shift during the anneal process of GaInNAs QWs.

To limit nitrogen diffusion, the GaInNAs QWs were inserted between GaAsN barriers. This also resulted in longer wavelength emission due to decreased carrier confinement energy. This new active region resulted in devices emitting at 1.3 μm .

Acknowledgements

This work would not have been possible without the support, advice, friendship and help of a number of people. I wish I could do more than merely say: “Thank You”.

First and foremost, I would like to thank my advisor, Prof. James Harris or “Coach”. He creates an unique research environment by giving the incredible freedom to choose and pursue your own research project, and by bringing together great people from different departments. At the same time, he is very supportive of your work and helps building up collaborations with other labs. This environment not only enabled me to make technical progress, but it also allowed me to develop the necessary skills to be successful in future endeavors.

I would like to thank a number of past and present Harris’ group members for their wisdom, insight, support, and friendship. The insights and efforts of Mike Larson and Chris Coldren made this project possible. Chris taught me the practicalities of MBE, made me appreciate the physics of opto-electronic devices, and was also great resource to discuss materials issues. I like to thank Mike for his listening ear and great inputs. Wayne Martin was not only the computer guru but also our get-the-lab-equipment-working guru. I would like to thank Chien-Chung Lin, Thierry Pinguet, Mark Wistey, Xian Liu, Vincent Gambin, and Vijit Sabnis for their always available helping hand in the MBE lab. Tzu-Fang Huang and Cheng-Yu Hung taught me how to apply the core classes to III-V materials. Thorsten Hesjedal helped me with great insights especially when I thought I had reached a dead end. Serguei Komarov and Barden Shimbo helped me with my occasional AFM measurements.

I would like to thank Dr. Ann Marshall for helping me out even when she was really busy. I would like to thank Prof. Mike Kelly for learning me how to combine experiment and theory.

I would also like to thank my collaborators outside Stanford University: Dr. Peter Krispin, Dr. Klaus Ploog, Dr. Manfred Ramsteiner, and Dr. William Wampler.

I would like to thank Gail Chun Creech for endless patience with my last minute requests.

I am grateful to Prof. Bent, Prof. Musgrave, Prof. Nix, and Prof. Wang for serving on my oral defense committee and on my reading committee. Their insightful and supportive feedback has been helpful in shaping the final form of this work and in focusing me onto many details that I would otherwise have overlooked.

Finally, I would like to thank my parents for learning me the discipline and giving me the support and education to get so far. I would like to thank Pieter for believing in me when I did not believe in myself and for making our dream come true...

Table of Contents

| | | |
|--|---|-------------|
| ABSTRACT | | IV |
| ACKNOWLEDGEMENTS | | VI |
| TABLE OF CONTENTS | | VIII |
| LIST OF TABLES | | XI |
| LIST OF ILLUSTRATIONS | | XII |
| CHAPTER 1: INTRODUCTION | | 1 |
| 1.1 | GOAL..... | 1 |
| 1.2 | TECHNOLOGICAL IMPLICATIONS OF THE WORK | 4 |
| 1.2.1 | <i>Characteristics of a hetero-structure pin laser diode and Vertical Cavity Surface Emitting Laser (VCSEL)</i> | 4 |
| 1.2.2 | <i>Application of 1.3 μm VCSELs in fiber communication</i> | 6 |
| 1.2.3 | <i>Application of 1.3 μm lasers to improve eye safety</i> | 9 |
| 1.2.4 | <i>Other DBR devices operating at 1.3 μm</i> | 10 |
| 1.3 | ALTERNATIVE MATERIAL SYSTEMS FOR 1.3 μm EMISSION..... | 10 |
| 1.4 | PROPERTIES OF NITRIDES AND ARSENIDES | 13 |
| 1.5 | OUTLINE OF THE DISSERTATION | 14 |
| 1.6 | SUMMARY | 15 |
| CHAPTER 2: MOLECULAR BEAM EPITAXY GROWTH OF NITRIDE-ARSENIDES | | 16 |
| 2.1 | GROWTH OF III-V MATERIALS FOR HETERO-JUNCTION DEVICES | 16 |
| 2.1.1 | <i>Molecular Beam Epitaxy</i> | 16 |
| 2.1.2 | <i>Lattice Mismatch</i> | 22 |
| 2.2 | OPTIMIZATION OF THE RADIO FREQUENCY PLASMA..... | 25 |
| 2.3 | CONTROL OF NITROGEN CONCENTRATION | 29 |

| | | |
|-------------------|---|-----------|
| 2.4 | GROWTH TEMPERATURE AND PHASE SEGREGATION | 34 |
| 2.4.1 | <i>Regular solution model</i> | 35 |
| 2.4.2 | <i>Stability of a regular solution</i> | 37 |
| 2.4.3 | <i>Growth conditions resulting in non-phase segregated material</i> | 41 |
| 2.4.4 | <i>Spinodal decomposition calculations</i> | 49 |
| 2.4.5 | <i>Ordering</i> | 50 |
| 2.5 | MBE VERSUS MOCVD GROWTH OF NITRIDE-ARSENIDES | 51 |
| 2.6 | CONCLUSION | 52 |
| CHAPTER 3: | OPTICAL PROPERTIES OF NITRIDE-ARSENIDES | 53 |
| 3.1 | DEPENDENCE OF GaNAs BANDGAP ON COMPOSITION..... | 53 |
| 3.1.1 | <i>Theoretical background for absorption measurements</i> | 53 |
| 3.1.2 | <i>Experimental determination of GaNAs bandgap versus nitrogen concentration</i> | 57 |
| 3.2 | PHOTOLUMINESCENCE FROM NITRIDE-ARSENIDES..... | 60 |
| 3.2.1 | <i>Theoretical background for photoluminescence measurements</i> | 60 |
| 3.2.2 | <i>Model for energy levels and absorption in a quantum well</i> | 64 |
| 3.2.3 | <i>Photoluminescence from GaNAs and GaInNAs quantum wells and effect of anneal</i> | 69 |
| 3.2.4 | <i>Origin of intensity increase when annealing GaNAs</i> | 73 |
| 3.2.5 | <i>Origin of wavelength shift when annealing GaNAs and GaInNAs</i> | 82 |
| 3.2.6 | <i>Conclusion</i> | 85 |
| 3.3 | CONCLUSION | 87 |
| CHAPTER 4: | NEW ACTIVE LAYER DESIGN ENABLING EMISSION AT 1.3 μM. | 88 |
| 4.1 | PHOTOLUMINESCENCE FROM GaInNAs QWS WITH GaNAs AND GaAs BARRIERS..... | 88 |
| 4.2 | COMPARISON OF GaNAs AND GaAs BARRIERS | 90 |
| 4.3 | BROAD AREA EDGE-EMITTING LASER AT 1.3 μ M USING GaNAs BARRIERS | 92 |
| 4.3.1 | <i>Introduction broad area edge-emitting laser operation</i> | 92 |
| 4.3.2 | <i>Description of laser structure and room temperature performance</i> | 93 |
| 4.3.3 | <i>Thermal properties of broad area edge-emitting laser with GaNAs barriers</i> | 95 |
| 4.4 | CONCLUSION | 96 |
| CHAPTER 5: | SUMMARY AND FUTURE WORK..... | 97 |
| 5.1 | SUMMARY | 97 |
| 5.2 | SUGGESTIONS FOR FUTURE WORK | 98 |
| 5.2.1 | <i>Exploring the growth of nitride-arsenides</i> | 98 |
| 5.2.2 | <i>Investigating the properties of nitride-arsenides</i> | 98 |
| 5.2.3 | <i>Contributing to better understanding of nitride-arsenides through computer simulation</i> | 99 |

| | | |
|-------------------|---|------------|
| 5.2.4 | <i>Building opto-electronic devices operating at 1.3 μm</i> | 99 |
| CHAPTER 6: | REFERENCES | 100 |

List of Tables

| | |
|---|----|
| TABLE 1: PROPERTIES OF NITRIDES AND ARSENIDES. | 13 |
| TABLE 2: PROPERTIES OF ARSENIC AND NITROGEN. | 14 |
| TABLE 3: DESCRIPTION OF VARIOUS SEMI-EMPIRICAL MODELS OF SOLUTIONS AND THEIR CORRESPONDING MOLAR ENTHALPIES AND ENTROPIES OF MIXING. THE MOLAR GIBBS FREE ENERGY OF MIXING IS THUS $G_M = H_M - TS_M$. | 35 |
| TABLE 4: NRA SIGNAL FROM ANNEALED AND AS-GROWN $\text{GaN}_{0.03}\text{As}_{0.97}$ FILM. ANNEALING WAS DONE FOR 1 MIN AT 760 °C UNDER ARGON AMBIENT WITH PROXIMITY CAPPING. | 81 |

List of Illustrations

| | |
|--|----|
| FIGURE 1: BANDGAP ENERGY AND OPERATING WAVELENGTH VERSUS LATTICE CONSTANT FOR VARIOUS III-V MATERIALS. LINES CONNECTING BINARY COMPOUNDS REPRESENT TERNARY ALLOYS..... | 2 |
| FIGURE 2: SCHEMATIC DIAGRAM OF BAND LINE-UP FOR INGAAS AND GANAS..... | 3 |
| FIGURE 3: ASPECTS OF THE DOUBLE-HETERO-STRUCTURE DIODE LASER: (A) SCHEMATIC OF THE MATERIAL STRUCTURE (B) ENERGY DIAGRAM OF THE CONDUCTION AND VALENCE BANDS VERSUS TRANSVERSE DISTANCE. | 4 |
| FIGURE 4: ELECTRONIC TRANSITION BETWEEN THE CONDUCTION AND VALENCE BANDS: (A) NON-RADIATIVE RECOMBINATION PROCESSES (B) SPONTANEOUS EMISSION (C) ABSORPTION (D) STIMULATED EMISSION. | 5 |
| FIGURE 5: (A) BROAD AREA EDGE-EMITTING LASER (B) VCSEL..... | 6 |
| FIGURE 6: CHARACTERISTICS OF OPTICAL FIBER: (A) ATTENUATION IN AN ALL-GLASS FIBER (B) DISPERSION IN AN ALL-GLASS FIBER | 7 |
| FIGURE 7: MAXIMUM TRANSMISSION DISTANCE VERSUS BIT RATE FOR SEVERAL TYPES OF OPTICAL FIBER COMMUNICATION SYSTEMS | 8 |
| FIGURE 8: LASER POWER LEVELS FOR APPROVED EYE SAFE OPERATION..... | 9 |
| FIGURE 9: SOLID VERSUS VAPOR COMPOSITION FOR ARSENIDE-PHOSPHIDE ALLOYS FOR DIFFERENT SUBSTRATE TEMPERATURES | 11 |
| FIGURE 10: FORMATION OF QUANTUM DOTS..... | 13 |
| FIGURE 11: SCHEMATIC ILLUSTRATION OF THE PROCESSES OCCURRING DURING MBE. | 17 |
| FIGURE 12: PLANAR VIEW OF THE AS-RICH GAAS (100) (2×4) SURFACE UNIT CELL. THE AS ATOMS (■) FORM THREE DIMERS PER UNIT CELL. THE DIMER VACANCY EXPOSES FOUR GALLIUM ATOMS (●) IN THE SECOND LAYER. | 19 |
| FIGURE 13: MBE GROWTH CHAMBER..... | 20 |
| FIGURE 14: NITROGEN, HYDROGEN, OXYGEN, CARBON, AND BORON CONCENTRATION PROFILE MEASURED BY SIMS IN AN CAMECA IMS 4.5F INSTRUMENT USING CESIUM ION BOMBARDMENT. THE SAMPLE STRUCTURE CONSISTS OF A GAAS SUBSTRATE, GAAS BUFFER LAYER, GANAS LAYER GROWN WITH RF PLASMA RUNNING BUT SHUTTER IN FRONT OF IT CLOSED, GAAS BUFFER LAYER, AND GANAS LAYER GROWN WITH RF PLASMA RUNNING AND SHUTTER IN FRONT OF IT OPEN. | 21 |

| | |
|---|----|
| FIGURE 15: DEFECT CONCENTRATION VERSUS DEPTH IN A GAAS/GAN _{0.03} AS _{0.97} /GAAS STRUCTURE MEASURED BY DEEP LEVEL TRANSIENT SPECTROSCOPY (DLTS)..... | 22 |
| FIGURE 16: (A) HIGH RESOLUTION TEM IMAGE OF A GA _{0.8} IN _{0.2} N _{0.015} AS _{0.985} QUANTUM WELLS WITH GAAS BARRIERS. (B) INTENSITY IN THE IMAGE SUMMED OVER THE WIDTH OF THE PICTURE. THE OSCILLATIONS INDICATE THE POSITION OF THE ATOM PLANES..... | 23 |
| FIGURE 17: SCHEMATIC ILLUSTRATION OF THE CRITICAL THICKNESS CONCEPT FOR THE CASE OF A FILM WITH A BIGGER LATTICE PARAMETER THAN THE SUBSTRATE..... | 24 |
| FIGURE 18: SCHEMATIC PICTURE OF THE NITROGEN GAS SUPPLY. | 26 |
| FIGURE 19: EMISSION SPECTRUM OF THE RF NITROGEN PLASMA FOR A NITROGEN SUPPLY OF 0.25 SCCM AND POWER OF 300 W..... | 27 |
| FIGURE 20: PLASMA OPERATION AS FUNCTION OF NITROGEN FLOW AND PLASMA POWER. THE AMOUNT OF EXCITED NITROGEN IN THE PLASMA AS FUNCTION OF (A) NITROGEN FLOW AND (B) PLASMA POWER. THE RATIO OF ATOMIC VERSUS MOLECULAR NITROGEN CONCENTRATION IN THE PLASMA AS FUNCTION OF (C) NITROGEN FLOW AND (D) PLASMA POWER. THE GRAY POINTS IN (A) AND (C) ARE DATA OBTAINED WHEN THE NITROGEN FLOW WAS TURNED DOWN TO 0.15 SCCM AND THEN BACK TO 0.25 SCCM. | 28 |
| FIGURE 21: CONCENTRATION OF NITROGEN IN GANAS FILMS AS FUNCTION OF THE GAAS GROWTH RATE. THE NITROGEN CONCENTRATION WAS MEASURED BY HRXRD, SIMS, AND ELECTRON MICROPROBE ANALYSIS. THE NITROGEN PLASMA WAS OPERATED WITH A POWER OF 300 W AND A NITROGEN FLOW OF 0.25 SCCM. | 30 |
| FIGURE 22: (A) REGION OF THE RECIPROCAL SPACE MAP NEAR THE (224) RECIPROCAL LATTICE POINT (B) RECIPROCAL SPACE CONTOUR MAP OF 2500 Å THICK, GAN _{0.025} AS _{0.975} ON GAAS. | 32 |
| FIGURE 23: XPS SIGNAL FROM A 650 Å GAN _{0.1} AS _{0.9} FILM ON GAAS SUBSTRATE BEFORE AND AFTER ARGON SPUTTERING..... | 33 |
| FIGURE 24: ESCAPE DEPTH OF ELECTRONS DURING AES OR XPS..... | 34 |
| FIGURE 25: EMISSION PROBABILITY OF AN AUGER ELECTRON (A) OR PHOTON (X)..... | 34 |
| FIGURE 26: TYPICAL TEMPERATURE DEPENDENCE OF THE MOLAR FREE ENERGY OF A REGULAR SOLUTION . | 39 |
| FIGURE 27: CRITERION OF STABILITY FOR A HOMOGENEOUS SOLUTION. (A) $\frac{\delta^2 g}{\delta x^2} > 0$: STABLE SOLUTION.(B) $\frac{\delta^2 g}{\delta x^2} < 0$: UNSTABLE SOLUTION; (C) $\frac{\delta^2 g}{\delta x^2} > 0$: SPINODAL POINT..... | 40 |
| FIGURE 28: EXAMPLE OF A MISCIBILITY GAP AND A SPINODAL LINE IN THE CASE OF A REGULAR SOLUTION .. | 40 |
| FIGURE 29: (A) THE PRODUCT OF EQUIVALENT PRESSURES OF (AS ₂) ^{1/2} AND GA FOR WHICH THE GAAS REACTION OCCURS IN GANAS, AND (B) THE PRODUCT OF THE EQUIVALENT PRESSURES OF GA AND ATOMIC N FOR WHICH THE GAN REACTION OCCURS IN GANAS. THE SHADED BOX INDICATES THE POSSIBLE GROWTH CONDITIONS..... | 43 |
| FIGURE 30: (A) THE PRODUCT OF EQUIVALENT PRESSURES OF (AS ₂) ^{1/2} AND GA FOR WHICH THE GAAS REACTION OCCURS IN GAN _{0.05} AS _{0.95} (B) HRXRD 2THETA/OMEGA CURVE FROM A 400 Å GAN _{0.05} AS _{0.95} | |

| | |
|--|----|
| FILM GROWN AT 500°C AND A FILM GROWN UNDER SAME GROUP III AND GROUP V FLUXES AT 700°C. | 44 |
| FIGURE 31: (A) THE PRODUCT OF EQUIVALENT PRESSURES OF $(As_2)^{1/2}$ AND GA FOR WHICH THE GAAS REACTION OCCURS IN $Ga_yIn_{1-y}N_xAs_{1-x}$, (B) THE PRODUCT OF THE EQUIVALENT PRESSURES OF GA AND ATOMIC N FOR WHICH THE GAN REACTION OCCURS IN $Ga_yIn_{1-y}N_xAs_{1-x}$, (C) THE PRODUCT OF EQUIVALENT PRESSURES OF $(As_2)^{1/2}$ AND IN FOR WHICH THE INAS REACTION OCCURS IN $Ga_yIn_{1-y}N_xAs_{1-x}$, (D) THE PRODUCT OF THE EQUIVALENT PRESSURES OF IN AND ATOMIC N FOR WHICH THE INN REACTION OCCURS IN $Ga_yIn_{1-y}N_xAs_{1-x}$, THE POSSIBLE GROWTH CONDITIONS ARE INDICATED BY THE SHADED BOX. | 47 |
| FIGURE 32: ATOMIC STRUCTURE OF THE DIMERIZED (001) SURFACE. THE SOLID DOTS REPRESENT CATIONS, WHILE THE OPEN AND HATCHED DOTS REPRESENT ANIONS ON THE α AND β SITES RESPECTIVELY. | 48 |
| FIGURE 33: A CONTOUR PLOT OF THE MISCIBILITY GAP IN $Ga_yIn_{1-y}N_xAs_{1-x}$ ON A GAAS SUBSTRATE (A) NEGLECTING STRAIN EFFECTS AND (B) INCLUDING STRAIN EFFECTS. THE NUMBERS IN THE FIGURE SHOW THE CRITICAL TEMPERATURES ABOVE WHICH THE MATERIAL IS META-STABLE. | 50 |
| FIGURE 34: DIAGRAM OF EXPERIMENTAL SETUP FOR ABSORPTION MEASUREMENT. | 54 |
| FIGURE 35: (A) ILLUSTRATION OF DIRECT OPTICAL TRANSITIONS BETWEEN AN ELECTRON STATE IN THE VALENCE BAND TO A STATE IN THE CONDUCTION BAND WITH THE SAME MOMENTUM (B) RESULTING ABSORPTION FOR THESE DIRECT OPTICAL TRANSITIONS. | 57 |
| FIGURE 36: (A) SYMMETRIC HRXRD SCANS SHOWING GAAS AND GANAS 004 PEAK (B) ABSORPTION MEASUREMENT FROM THE SAME SAMPLE. | 58 |
| FIGURE 37: INDIUM AND NITROGEN CONCENTRATION FOR $GaInNAs$ ALLOYS RESULTING IN BULK 1.3 μm EMISSION. | 60 |
| FIGURE 38: EXPERIMENTAL SETUP USED FOR PL MEASUREMENT. | 61 |
| FIGURE 39: SCHEMATIC OF PL PROCESSES IN SEMICONDUCTORS. | 62 |
| FIGURE 40: (A) MAIN PARTS OF A NEAR-BAND-EDGE PL SPECTRUM, AND (B) SCHEMATIC REPRESENTATION OF THE CORRESPONDING RECOMBINATIONS. | 62 |
| FIGURE 41: SPONTANEOUS EMISSION SPECTRUM FOR A GAAS-LIKE SEMICONDUCTOR. ENERGY UNITS ARE $k_B T$. | 64 |
| FIGURE 42: (A) A QW WITH A WIDTH L AND AN INFINITE BARRIER $V_0 = \infty$. (B) THE ENERGY DISPERSION IN THE k_x OR k_y SPACE. | 65 |
| FIGURE 43: (A) A QW WITH A WIDTH L AND A FINITE BARRIER HEIGHT V_0 . THE ENERGY LEVELS FOR $n=1$ AND $n=2$ AND THEIR CORRESPONDING WAVE FUNCTIONS ARE SHOWN. (B) A GRAPHICAL SOLUTION FOR THE DECAYING CONSTANT α AND WAVE NUMBER k OF A QW WITH FINITE BARRIERS. | 66 |
| FIGURE 44: THE ELECTRON DENSITY OF STATES $\rho_{2D}(E)$ (SOLID LINE) FOR A TWO-DIMENSIONAL QW STRUCTURE COMPARED WITH THE THREE-DIMENSIONAL DENSITY OF STATES $\rho_{3D}(E)$. | 68 |

| | |
|---|----|
| FIGURE 45: (A) SAMPLE STRUCTURE AND (B) PHOTOLUMINESCENCE SPECTRUM OF AS-GROWN AND ANNEALED 70 Å $\text{Ga}_{0.7}\text{In}_{0.3}\text{N}_{0.02}\text{As}_{0.98}$ QWS WITH GAAS BARRIERS. THE SAMPLES WERE PROXIMITY CAPPED WITH GAAS AND ANNEALED FOR 60 SECONDS AT 760 °C UNDER A N_2 AMBIENT..... | 70 |
| FIGURE 46: ROOM-TEMPERATURE PHOTOLUMINESCENCE INTENSITY AND WAVELENGTH SHIFT OF 70Å $\text{Ga}_{0.7}\text{In}_{0.3}\text{N}_{0.02}\text{As}_{0.98}$ /GAAS QUANTUM WELLS AS FUNCTION OF (A) ANNEAL TIME FOR ANNEAL TEMPERATURE OF 660 °C AND (B) ANNEAL TEMPERATURE FOR AN ANNEAL TIME OF 60 SECONDS. EXCITATION WAS FROM THE 514NM LINE OF AN Ar^+ ION LASER. SAMPLES WERE PROXIMITY CAPPED AND ANNEALED UNDER N_2 AMBIENT. | 71 |
| FIGURE 47: (A) SAMPLE STRUCTURE AND (B) PHOTOLUMINESCENCE SPECTRUM OF AS-GROWN AND ANNEALED 70 Å $\text{GaN}_{0.02}\text{As}_{0.98}$ QUANTUM WELLS WITH GAAS BARRIERS. THE SAMPLE WAS PROXIMITY CAPPED AND ANNEALED FOR 60 SECONDS AT 760 °C UNDER A N_2 AMBIENT..... | 72 |
| FIGURE 48: (A) SAMPLE STRUCTURE AND (B) PHOTOLUMINESCENCE SPECTRUM OF AS-GROWN 65 Å $\text{Ga}_{0.7}\text{In}_{0.3}\text{N}_{0.012}\text{As}_{0.988}$ AND $\text{Ga}_{0.7}\text{In}_{0.3}\text{N}_{0.02}\text{As}_{0.98}$ QUANTUM WELLS WITH GAAS BARRIERS. | 73 |
| FIGURE 49: (A) SAMPLE STRUCTURE AND (B) FREE HOLE PROFILE OF A P-DOPED AS-GROWN AND ANNEALED 500 Å $\text{GaN}_{0.03}\text{As}_{0.97}$ QUANTUM WELL WITH GAAS BARRIERS. THE SAMPLE WAS PROXIMITY CAPPED AND ANNEALED FOR 60 SECONDS AT 760 °C UNDER A N_2 AMBIENT, (C) SAMPLE STRUCTURE AND (B) FREE ELECTRON PROFILE OF A N-DOPED AS-GROWN AND ANNEALED 500 Å $\text{GaN}_{0.03}\text{As}_{0.97}$ QUANTUM WELL WITH GAAS BARRIERS. THE SAMPLE WAS PROXIMITY CAPPED AND ANNEALED FOR 60 SECONDS AT 760 °C UNDER A N_2 AMBIENT. | 75 |
| FIGURE 50: HRXRD ROCKING CURVE OF THE 004 PEAK FROM A 2500 Å $\text{GaN}_{0.025}\text{As}_{0.975}$ FILM ON GAAS. THE SAMPLE WAS PROXIMITY CAPPED AND ANNEALED FOR 5 MIN AT 760 °C UNDER A N_2 AMBIENT. .. | 76 |
| FIGURE 51: HRXRD ROCKING CURVE FROM AN ANNEALED AND AS-GROWN 6 PERIOD 70 Å $\text{GaN}_{0.05}\text{As}_{0.95}$ /130 Å GAAS SUPERLATTICE. ANNEALING WAS DONE FOR 10 SECONDS AT 775 °C. | 77 |
| FIGURE 52: LATTICE PARAMETER OF DIFFERENT GaNAs FILMS AS FUNCTION OF NITROGEN CONCENTRATION. THE LATTICE PARAMETER OF THE FILMS WAS DETERMINED USING HRXRD IN A PHILIPS MATERIALS RESEARCH DIFFRACTOMETER. THE NITROGEN CONCENTRATION WAS MEASURED BY SIMS IN A CAMECA IMS 4.5F INSTRUMENT. | 78 |
| FIGURE 53: XPS SIGNAL FROM N(1s) PEAK FROM ANNEALED AND AS-GROWN $\text{GaN}_{0.06}\text{As}_{0.94}$ FILM MEASURED IN A PHI 5800 INSTRUMENT. THE GALLIUM AUGER PEAK AROUND 398 eV WAS REMOVED BY DIVIDING THE OBTAINED SPECTRUM BY THE SPECTRUM OF A GAAS REFERENCE SAMPLE. ANNEALING WAS DONE FOR 30 SECONDS AT 775 °C UNDER A N_2 AMBIENT WITH PROXIMITY CAPPING..... | 78 |
| FIGURE 54: SAMPLE STRUCTURE FOR THE NRA MEASUREMENTS..... | 81 |
| FIGURE 55: NITROGEN DISTRIBUTION AFTER ANNEALING COMPARED WITH THE AS-GROWN STARTING PROFILE. COMPUTER-SIMULATED CURVES DEMONSTRATE THE VALIDITY OF THE KICK-OUT MECHANISM AS WELL AS THE FAILURE OF THE DISSOCIATIVE MECHANISM, THE INTERSTITIAL MECHANISM, AND OTHER GAUSSIAN-LIKE BROADENING | 83 |

| | |
|---|----|
| FIGURE 56: SIMS PROFILE OF (A) INDIUM, (B) NITROGEN AND (C) NITROGEN IN 70Å $\text{Ga}_{0.7}$ $\text{In}_{0.3}\text{N}_{0.02}\text{As}_{0.98}$ /GAAS QUANTUM WELLS WITH STRUCTURE SHOWN IN FIGURE 45(A). THE SAMPLE WAS PROXIMITY CAPPED AND ANNEALED FOR 1 MIN AT 760 °C UNDER N_2 AMBIENT. | 84 |
| FIGURE 57: PHOTOLUMINESCENCE SPECTRUM OF AS-GROWN AND ANNEALED 70 Å $\text{Ga}_{0.7}\text{In}_{0.3}\text{N}_{0.02}\text{As}_{0.98}$ QWS WITH GAAS BARRIERS WITH STRUCTURE SHOWN IN FIGURE 45(A). THE SAMPLES WERE PROXIMITY CAPPED AND ANNEALED FOR 1 MIN OR 5 MIN AT 760 °C UNDER A N_2 OR ARGON AMBIENT. | 85 |
| FIGURE 58: (A) SAMPLE STRUCTURE AND (B) PHOTOLUMINESCENCE SPECTRUM OF AS-GROWN AND ANNEALED GaInNAs QWS WITH GAAS BARRIERS. THE SAMPLES WERE PROXIMITY CAPPED AND ANNEALED FOR 60 SECONDS AT 760 °C UNDER A N_2 AMBIENT. | 86 |
| FIGURE 59: (A) SAMPLE STRUCTURE, (B) AND (C) PHOTOLUMINESCENCE SPECTRA OF AS-GROWN AND ANNEALED 65 Å $\text{Ga}_{0.65}\text{In}_{0.35}\text{N}_{0.02}\text{As}_{0.98}$ QWS WITH GAAS OR GaNAs BARRIERS. THE SAMPLES WERE PROXIMITY CAPPED AND ANNEALED FOR 60 SECONDS AT 760 °C UNDER A N_2 AMBIENT. | 89 |
| FIGURE 60: SCHEMATIC OF THE QW STRUCTURE FOR (A) GAAS AND (B) GaNAs BARRIERS. | 91 |
| FIGURE 61: ILLUSTRATION OF OUTPUT POWER VS. CURRENT FOR A DIODE LASER (L-I CURVE). BELOW THRESHOLD ONLY SPONTANEOUS EMISSION IS IMPORTANT; ABOVE THRESHOLD THE STIMULATED EMISSION POWER INCREASES WHILE THE SPONTANEOUS EMISSION IS CLAMPED AT ITS THRESHOLD VALUE. | 93 |
| FIGURE 62: (A) STRUCTURE, (B) L-I CURVE AND (C) EMISSION SPECTRUM OF AN BROAD AREA EDGE- EMITTING LASER WITH GaNAs BARRIERS AND GaInNAs QWS. | 94 |
| FIGURE 63: THRESHOLD CURRENT AS FUNCTION OF TEMPERATURE FOR THE DEVICE SHOWN IN FIGURE 62(A). THE MEASURED VALUE FOR T_0 IS 164 K. | 95 |

Chapter 1: Introduction

The development of broadband low cost local and metropolitan-area fiber communication networks can be accelerated by the development of 1.3 μm vertical cavity surface emitting lasers (VCSELs). Due to materials limitations, low cost commercially available VCSELs have only been realized on GaAs substrates. The goal of this thesis is the development of GaInNAs alloys to enable devices operating at 1.3 μm on GaAs substrates. We first give an overview of the state-of-the-art approach and other alternative approaches for 1.3 μm emission. Subsequently, the differences between the properties of the nitrides and arsenides will be outlined and related to the challenges encountered during the growth of nitride-arsenides.

1.1 Goal

Until recently, the operating wavelength of opto-electronic devices on GaAs substrates has been limited to below 1 μm due to the lack of III-V materials that are sufficiently close lattice match to GaAs to avoid misfit dislocations and simultaneously have a bandgap below 1.24 eV. This work describes the development of a new III-V material formed by adding small amounts of nitrogen to InGaAs; this GaInNAs alloy will enable opto-electronic devices operating at 1.3 μm on GaAs substrates.

A linear interpolation between the bandgap of GaAs and GaN (indicated by the dotted line in Figure 1) predicts a larger bandgap for $\text{GaN}_y\text{As}_{1-y}$ than for GaAs. In 1992, Weyers et al. [1] demonstrated experimentally that this expected behavior is not valid and that there is a significant downward bowing of the bandgap between GaAs and GaN. Local density approximation calculations by Wei et al. [2] and Neugebauer et al. [3]

show that the large differences between atomic orbital energies and sizes of the alloyed arsenic and nitrogen atoms result in charge exchange and structural relaxation. These localize the valence band on the arsenic sublattice and the conduction band on the nitrogen sublattice, and cause the bandgap of GaNAs to be smaller than the bandgap of GaAs. Figure 1 shows that the alloys GaNAs and GaInNAs are interesting because the addition of small amounts of nitrogen can significantly lower the band gap and make band gap wavelengths longer than 1.3 μm with lattice match to GaAs possible.

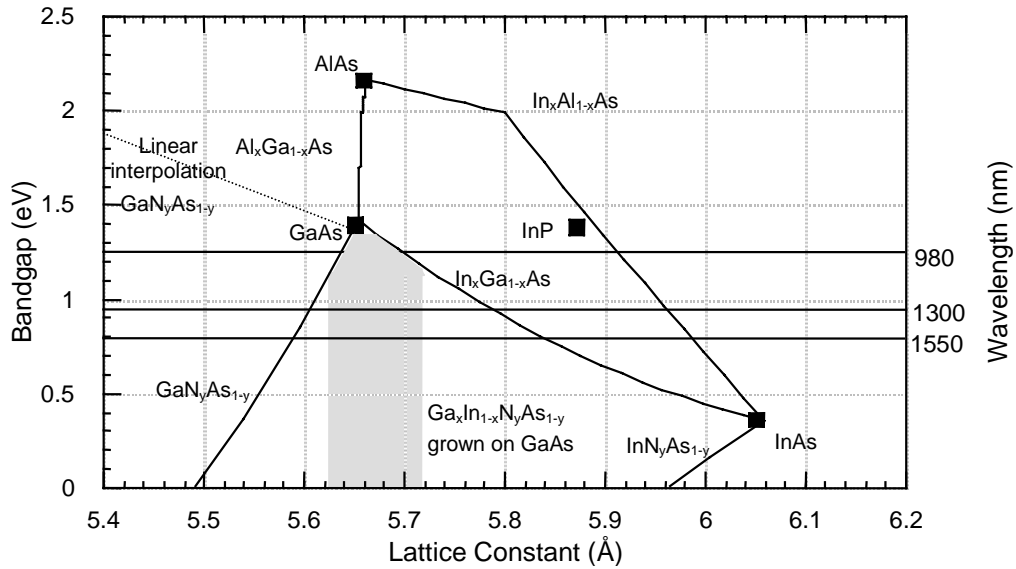


Figure 1: Bandgap energy and operating wavelength versus lattice constant for various III-V materials. Lines connecting binary compounds represent ternary alloys.

To allow the growth of dislocation-free devices on GaAs, the lattice parameter of GaInNAs must be closely matched to GaAs. Adding indium to GaAs, i.e., making a $\text{In}_x\text{Ga}_{1-x}\text{As}$ alloy, increases the lattice constant, while adding nitrogen to GaAs, i.e. making a $\text{GaN}_y\text{As}_{1-y}$ alloy, decreases the lattice constant. $\text{Ga}_x\text{In}_{1-x}\text{N}_y\text{As}_{1-y}$ can therefore be lattice matched to GaAs by adjusting the indium and nitrogen contents so that $(1-x) \approx 2.5y$. When increasing the compressive strain by increasing the indium concentration, the light hole band shifts up with respect to the heavy hole band [4]. This improves the gain of opto-electronic devices [4] but limits the thickness of the quantum well layer to below the critical thickness for dislocation formation (see section 2.1.2).

Another important materials parameter determining opto-electronic device operation is the band line-up and electron confinement. When applying a material in the quantum well active layer, a type I band lineup is essential to confine both electrons and

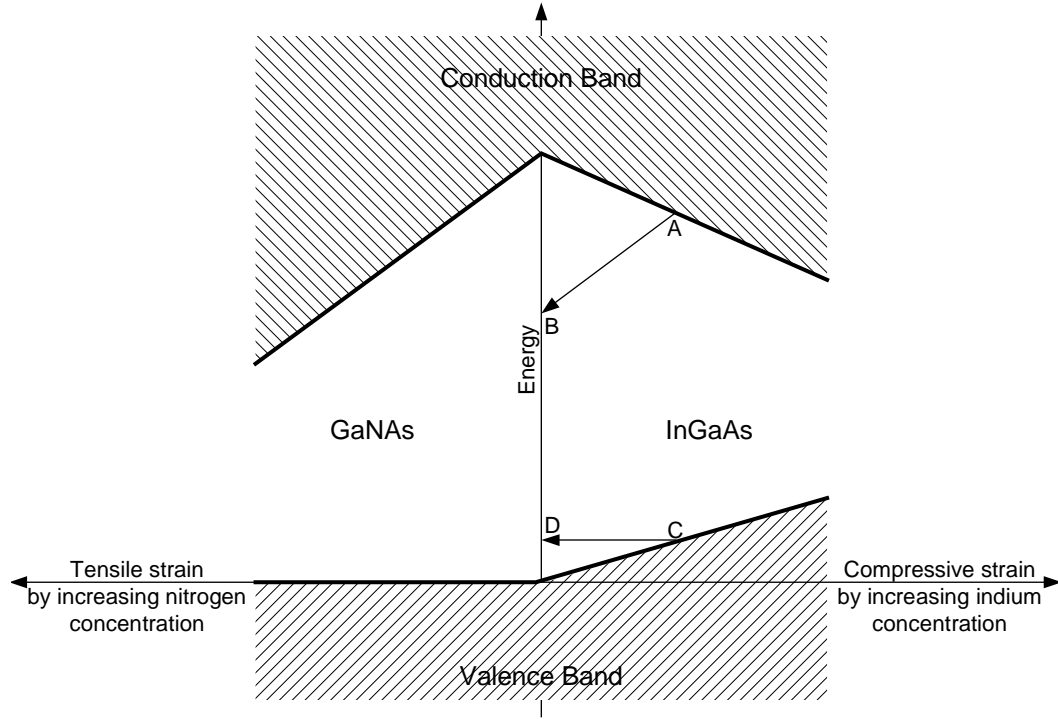


Figure 2: Schematic diagram of band line-up for InGaAs and GaNAs [5].

holes in the quantum well. A big conduction band offset is necessary to confine the electrons. Most of the band gap decrease resulting from adding nitrogen to GaAs occurs in the conduction band. We have experimentally verified that the valence band offset between GaNAs and GaAs is very small: the valence band in $\text{GaN}_{0.03}\text{As}_{0.97}$ is 11 meV higher than the valence band in GaAs [6]. Hence, increasing the nitrogen content in GaNAs, i.e. increasing the tensile strain, will lower the conduction band significantly and leave the valence band practically constant (as shown in Figure 2). Increasing the indium content in InGaAs, i.e. increasing the compressive strain, lowers the conduction band and raises the valence band. If nitrogen is added to InGaAs to form GaInNAs, the conduction and valence bands will be moved from A to B and from C to D in Figure 2. At the alloy composition lattice matched to GaAs most of the band gap difference occurs in the conduction band resulting in excellent electron confinement. The conduction band offset between $\text{Ga}_{0.7}\text{In}_{0.3}\text{N}_{0.02}\text{As}_{0.98}$ and GaAs is roughly $\Delta E_c = 0.7\Delta E_g$. By combining GaInNAs with wide gap materials such as GaAs or AlGaAs, a type I band lineup with a big conduction band offset is easily achieved. The large offset maintains electron confinement at elevated temperatures thus enabling the fabrication of lasers with better thermal properties.

Unfortunately, the different size and electron affinity of nitrogen and arsenic responsible for these beneficial bandgap properties, also result in immiscibility and spinodal decomposition of nitride-arsenide alloys [3,7]. The equilibrium bulk solubility of nitrogen in GaAs and InAs is only a fraction of a percent. A higher nitrogen concentration must be obtained by growing under non-equilibrium conditions and freezing this high nitrogen concentration in as the crystal grows. Therefore, the growth of these nitride-arsenides is expected to be difficult.

1.2 Technological implications of the work

1.2.1 Characteristics of a hetero-structure pin laser diode and vertical cavity surface emitting laser (VCSEL)

The smaller bandgap GaInNAs material can be used in a range of semiconductor devices. One of them is a hetero-structure pin vertical cavity surface emitting laser diode (see Figure 3). Like all lasers, this laser consists of two major components: an active gain region in which population inversion is possible and mirrors for feedback.

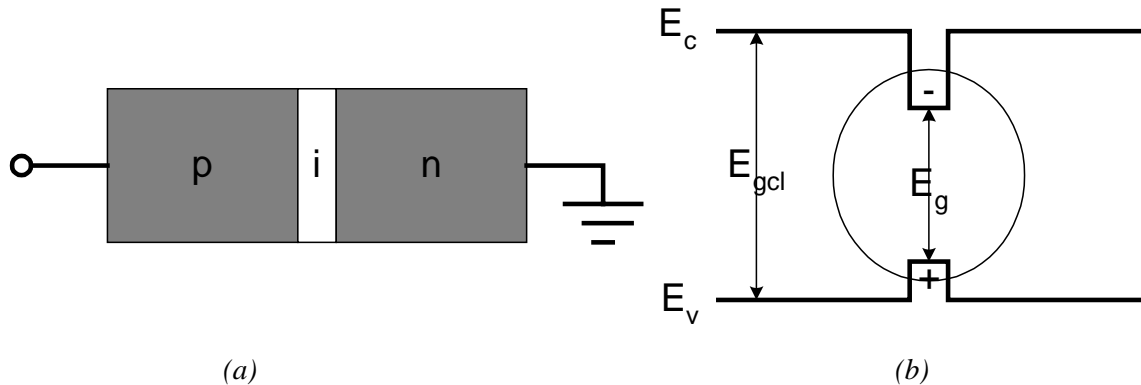


Figure 3: Aspects of the double-hetero-structure diode laser: (a) Schematic of the material structure (b) Energy diagram of the conduction and valence bands versus transverse distance.

In a pin hetero-structure diode, forward biasing the device leads to the population inversion. When the diode is biased, electrons flow from the wide bandgap n-region to the left but they get captured in the smaller bandgap intrinsic region. At the same time, holes move from the wide bandgap p-region to the right and get trapped in the smaller bandgap intrinsic region. Hence, the concentration of electrons and holes in the small bandgap intrinsic region or quantum well (QW) is higher than the equilibrium

concentration. The concentration of carriers in the smaller bandgap region is a function of the current injected into the diode. This high concentration of electrons and holes that are spatially close together will relax to the equilibrium concentration through a number of processes (see Figure 4). During spontaneous emission, an electron and hole recombine by emitting a photon (see Figure 4(b)). When a photon is incident on the material, either absorption or stimulated emission can occur. Absorption occurs when the photon stimulates an electron transition from the valence band to the conduction band (see Figure 4(c)). Stimulated emission occurs when the photon stimulates the recombination of an electron and hole simultaneously generating a new photon (see Figure 4(d)). Stimulated emission is responsible for the optical gain in the material. It will take place when the Fermi-Dirac distribution for electrons in the valence band is smaller than the Fermi-Dirac distribution for electrons in the conduction band, a condition known as population inversion limit. Below population inversion, absorption is the dominant process. The two non-radiative processes are Auger recombination and recombination of electrons and holes through a defect level in the energy gap (see Figure 4(a)) caused by impurities or crystal defects (point defects or dislocations). These non-radiative processes reduce the number of carriers that are available for stimulated emission. Hence, one of the big challenges when developing new materials for lasers is eliminating defects that result in non-radiative recombination.

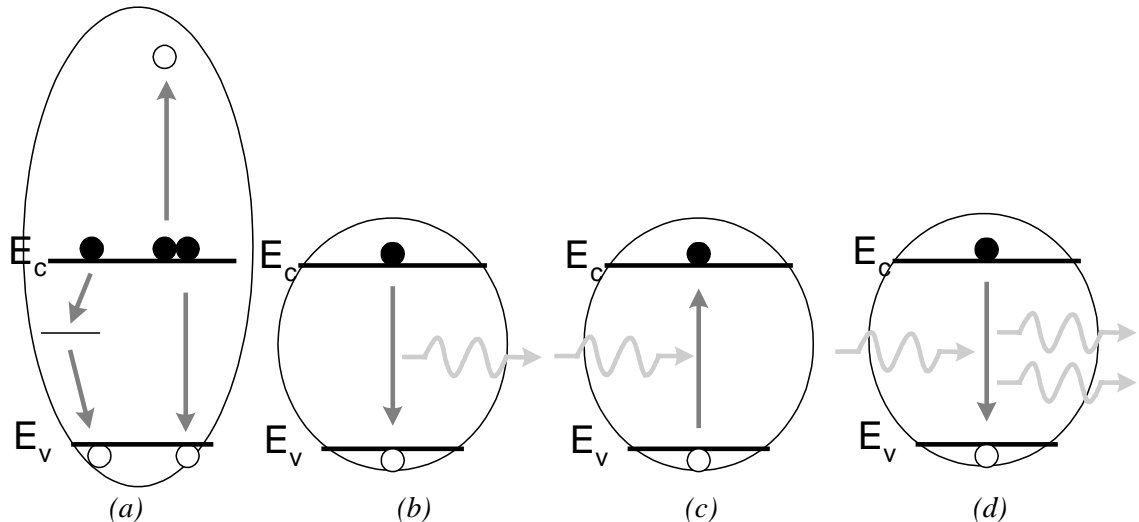


Figure 4: Electronic transition between the conduction and valence bands: (a) Non-radiative recombination processes (b) Spontaneous emission (c) Absorption (d) Stimulated emission.

The photon that triggers the stimulated emission is provided by photon feedback. For that purpose, mirrors must be placed at the two ends of the laser. Two configurations are possible (see Figure 5). The broad area edge-emitting laser is accomplished with a simple cleaved-facet mirror. It has lateral dimensions of a few microns. In the vertical cavity surface emitting laser (VCSEL), the optical wave is traveling up and down through the cavity. In this latter configuration, the path-length of the optical wave through the gain material is extremely short and the maximum gain is small. To reduce the losses in the cavity below the achievable gain, the mirrors on the top and the bottom have to be nearly 100 % reflective. Typically, this is done by stacking quarter wavelength layers of materials of alternating index of refraction, i.e. by creating a distributed Bragg reflector (DBR) mirror. The best developed DBR mirrors are based on GaAs/AlAs layers.

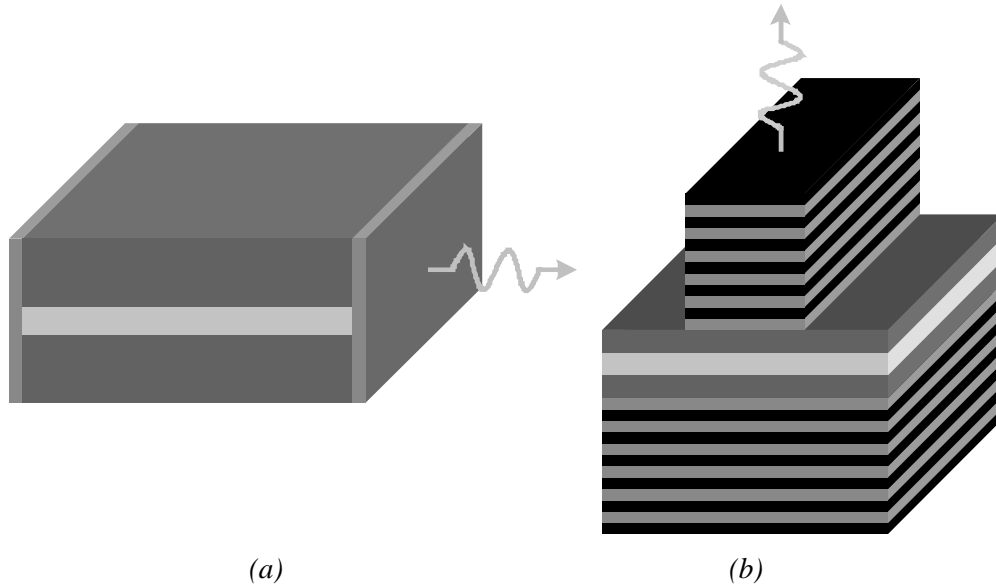


Figure 5: (a) Broad area edge-emitting laser (b) VCSEL.

1.2.2 Application of 1.3 μm VCSELs in fiber communication

VCSELs have significant advantages over broad-area edge emitting broad area lasers in fiber communication. They can be made inexpensively using IC processing techniques and the manufacturing and packaging costs are lower [8]. Furthermore, they couple easily into optical fibers reducing alignment and testing costs. Moreover, they have lower power dissipation and higher reliability. VCSELs can also be grown in two-dimensional arrays to maximize density and bandwidth performance. Hence, VCSELs

are the ideal source for metropolitan-area networks provided they emit at the right wavelength.

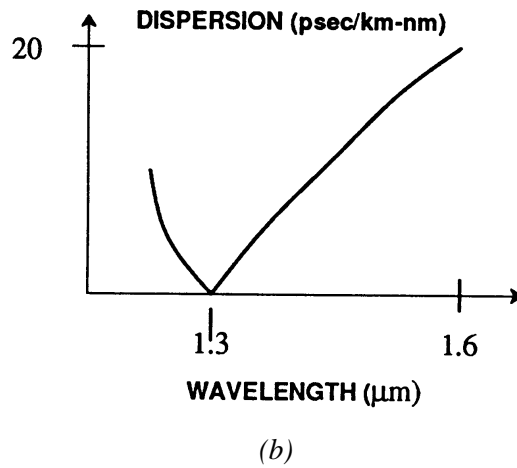
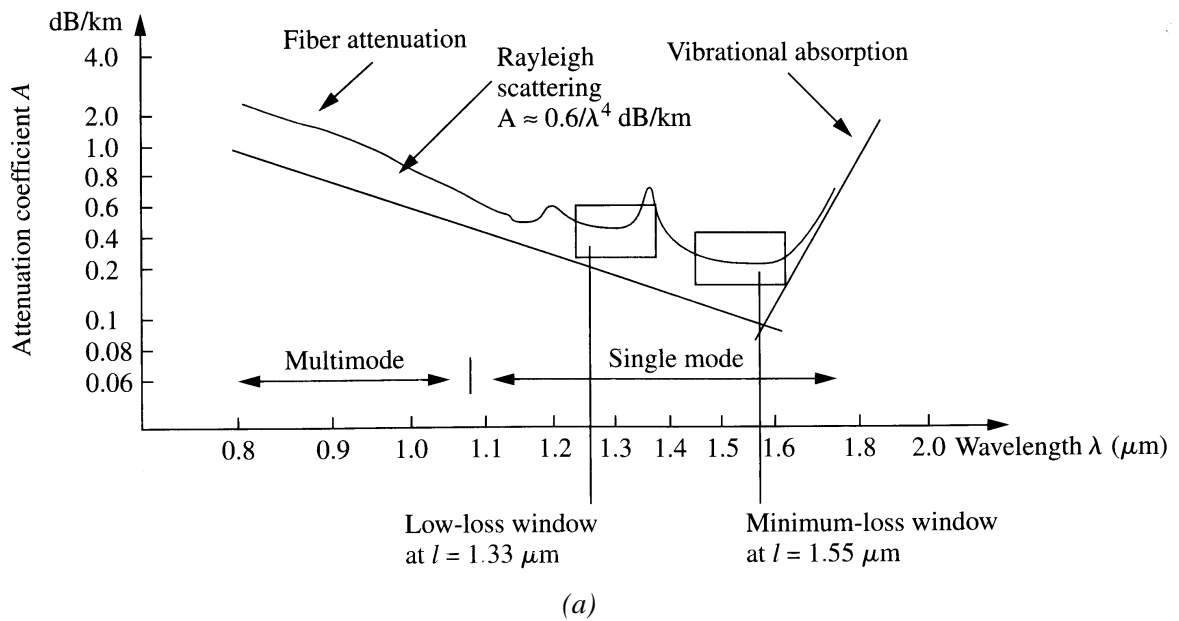


Figure 6: Characteristics of optical fiber: (a) Attenuation in an all-glass fiber [9] (b) Dispersion in an all-glass fiber [10].

The properties of fiber optical cable used in metropolitan-area networks are such that certain regions of wavelengths carry light farther than others (see Figure 6). Fiber optic transmission systems use the wavelength regions where light travels the farthest. The two most common wavelength regions used in carrier networks are 1.3 μm and 1.55 μm . 1.55 μm corresponds in a minimum loss in the optical fiber and 1.3 μm corresponds to zero dispersion (see Figure 6). Metropolitan-area transport and data communication systems today use 1.3 μm optics extensively because they provide the best distance-to-

cost tradeoffs. 1.55 μm is used extensively in long-distance systems, where the extra cost for the more expensive components is balanced by the reduced need to re-transmit the signal as it loses intensity. Long-haul telecommunication systems use the 1.55 μm region to transmit multiple signals because Erbium Doped Fiber Amplifiers (EDFAs) used to optically regenerate signals to travel greater distances operate only in the 1.55 μm region. The improved performance of 1.3 μm and 1.55 μm systems over 0.85 μm systems is clearly visible in Figure 7. For Gigabit Ethernet applications, 0.85 μm systems are limited to distances below 2 km; while 1.3 μm systems have a range of up to 150 km. As systems are evolving towards higher bit rates, the limits of 0.85 μm systems will be reached but 1.3 μm systems still have plenty potential.

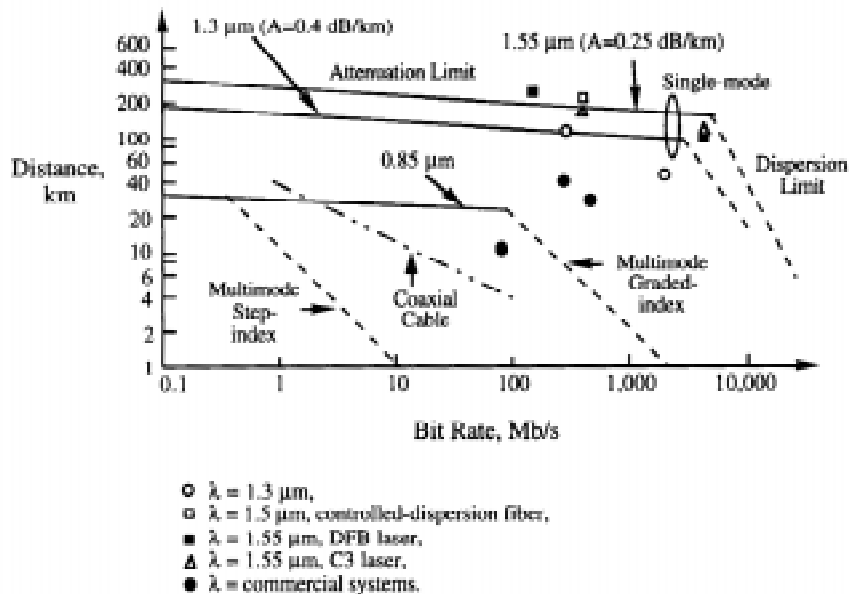


Figure 7: Maximum transmission distance versus bit rate for several types of optical fiber communication systems [11].

Currently commercially available VCSELs are based on GaAs substrates with AlAs/GaAs DBR mirrors. While they can launch signals down optical fibers at gigabit rates, they only emit 0.85 μm light. The poor match with the optical properties of the fiber limit the effective distance of transmission. Therefore, these shorter-wavelength diodes have been limited to Ethernet and Fiber Channel applications, where distances traveled are less than a few hundred meters.

The current boom in Internet traffic will require significant expansion of the metropolitan-area and data communication networks. The development of low cost VCSELs and other opto-electronic devices at 1.3 μm is necessary to enable this growth of the metropolitan-area networks. The GaInNAs materials system is very promising for this application as it allows the fabrication of VCSELs at 1.3 μm by combining a 1.3 μm active region with the already well-developed AlAs/GaAs mirror technology.

1.2.3 Application of 1.3 μm lasers to improve eye safety

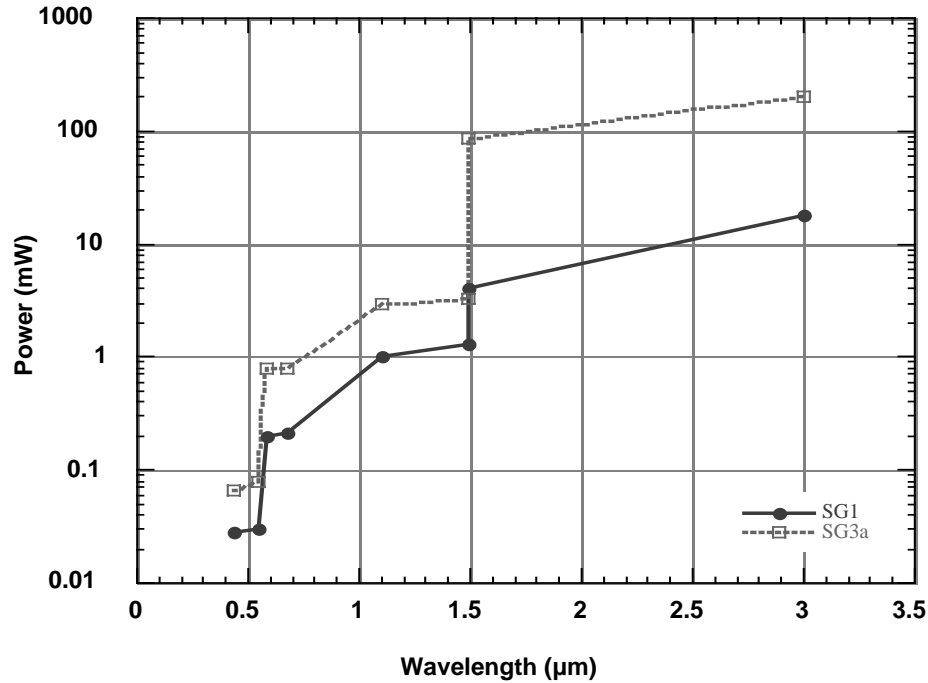


Figure 8: Laser power levels for approved eye safe operation.

Another restriction of the only commercially available VCSELs is the need to meet stringent eye-safety standards as they operate at 0.85 μm . Currently, safety standards limit the power output of laser-diodes, which has an impact on the level of performance that can be achieved. The output power of 0.85 μm VCSELs is limited to 0.4 mW. As the longer-wavelength light is less damaging to the eye at a given power level, it is easier to meet the standard while preserving a specified performance level. The accessible power level at 1.3 μm is greater than at 0.85 μm by almost an order of magnitude (see Figure 8). Moreover, for the same power level, 1.3 μm lasers results in 60 % more photons than 0.85 μm lasers.

1.2.4 Other DBR devices operating at 1.3 μm

Mass production of quarter wavelength DBRs is far more easily achieved in GaAs/AlAs alloys compared to alternative choices, other devices that require quarter wavelength DBRs can be extended to 1.3 μm by using GaInNAs alloys as active regions. Examples of these are tunable VCSELs, quantum well modulators, detectors, and wavelength sensitive fiber coupled devices.

1.3 Alternative material systems for 1.3 μm emission

The state-of-the-art material system used for 1.3 μm emission is $\text{Ga}_{0.2}\text{In}_{0.8}\text{As}_{0.6}\text{P}_{0.4}$ on InP substrates. It is most commonly grown by metal organic chemical vapor deposition (MOCVD). However, it has some serious drawbacks and has not yet been applied in commercial VCSELs due to fundamental materials limitations. Hence, a number of alternative material systems and structures are being investigated.

The most serious limitation of the GaInAsP system is the lack of index of refraction contrast between possible mirror materials lattice matched to InP substrates: GaInAsP/InP or GaAlInAs/AlInAs. Particularly at 1.3 μm , the growth of DBR mirrors based on these alloys is challenging, as they require a very large number (50 or more) of low loss mirror pairs. 20 mirror pairs are enough for AlGaAs/GaAs DBRs. Several alternatives for these GaInAsP/InP and GaAlInAs/AlInAs DBR mirrors have been investigated. The first approach is based on wafer fusion of a GaAs wafer with an AlAs/GaAs DBR mirror onto the InP wafer. Unfortunately, the interface is a source of defects for non-radiative recombination, carrier scattering and absorption, and the combined additional epitaxial growth and fusion steps drive up the fabrication cost [12]. Another approach is growing AlGaAs/GaAs metamorphic DBR mirrors [13]. Preventing propagation of dislocations from the DBR mirror into the QWs and avoiding excessive loss in the mirror is a challenge. A third approach is depositing dielectric mirrors after the epitaxial MOCVD growth. Dielectric mirrors based on ZnSe/MgF, $\text{SiO}_2/\text{TiO}_2$, Si/SiO₂, and Si/Al₂O₃ have been used [14], but these do not conduct electrical current and have low thermal conductivity. Hence, current injection into the active region and heat conduction away from the active region is difficult. A final approach is based on

AlGaAsSb mirrors [15]. The growth of these materials is challenging as lattice matching of AlGaAsSb and AlAsSb on InP requires a composition at the edge of the miscibility gap and the control of arsenic and antimony concentration is difficult. Moreover, quaternary alloys have a lower thermal and electrical conductivity than binary alloys like AlAs/GaAs resulting in heating of the device and larger voltage drops across the mirrors. These difficulties in making DBR mirrors are largely responsible for the fact that VCSELs based on GaInAsP active regions have only been demonstrated in research environments. They have a relatively modest performance over unacceptably small temperature ranges.

A second challenge in the GaInAsP material system is the control of the phosphorus concentration (see Figure 9). For group III-AsP alloys grown by MOCVD, both thermodynamics and kinetics play a significant role in determining the phosphorus concentration. At normal growth temperatures, the pyrolysis of the hydride sources is incomplete. As the pyrolysis rate is lower for PH_3 than for AsH_3 , temperature variations over the wafer during the growth give rise to composition variations over the wafer. This significantly reduces the yield and gives rise to the high cost (\$8,000-\$10,000) of edge-emitting communication lasers based on GaInAsP active regions.

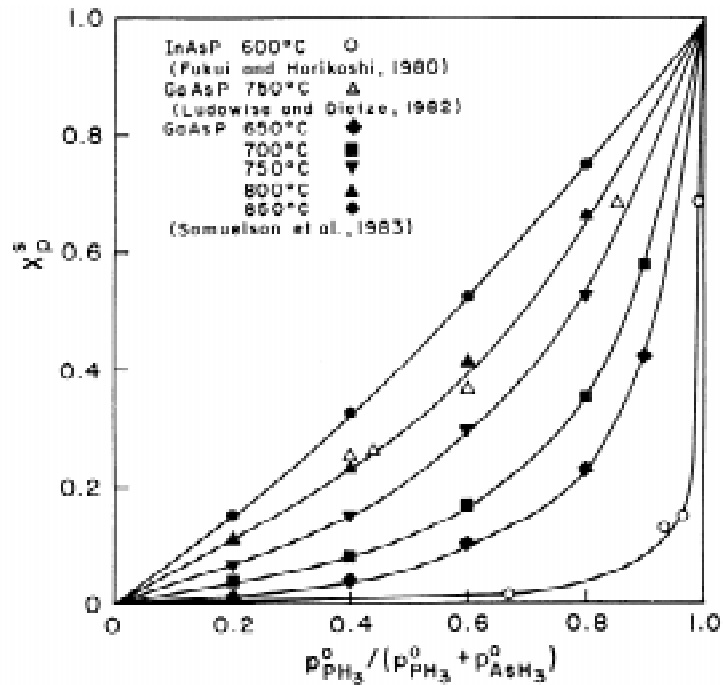


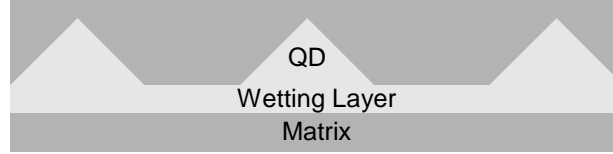
Figure 9: Solid versus vapor composition for arsenide-phosphide alloys for different substrate temperatures [16].

Finally, thermal degradation limits the operating range of these devices. The conduction band offset between GaInAsP and InP is small: $\Delta E_c = 0.4\Delta E_g$. Hence, electrons can escape from the quantum well when they have enough thermal energy. Moreover, the thermal conductivity of the DBR mirrors used on InP substrates is low. Therefore, the heat generated in a VCSEL is not efficiently removed. As the temperature increases, more electrons leak out of the well and the Auger recombination rate increases. This reduces the available gain. As the gain decreases, more carriers need to be injected to sustain population inversion; the resulting current increase will heat up the device even more. To avoid these degradation mechanisms, increases in the junction operating temperature must be avoided.

The conduction band offset and thermal properties can be improved by using GaAlInAs alloys on InP substrates [17]. Unfortunately, GaAlInAs alloys are difficult to grow due to phase segregation, ordering, and surface segregation. Moreover, the growth of DBR mirrors is still a challenge in this material system.

There are two additional competing material systems that are similar to GaInNAs because they are also grown on GaAs substrates. They thus also benefit from the well developed AlAs/GaAs DBR mirror technology.

The first of these is InAs or InGaAs quantum dots on GaAs. Due the lattice mismatch between InAs or the InGaAs alloy that produce 1.3 μm emission and GaAs, growth of InGaAs on GaAs results in Stranski-Krastanov mode growth with a very thin ($\sim 7\text{\AA}$) wetting layer and islands, also known as quantum dots (QDs) (see Figure 10). The threshold current of a QD laser has been predicted to be temperature independent due to the delta-function-like density of states of an ideal QD. However, it is found that the leakage of charge carriers out of the QDs into the states of the wetting layer is responsible for poorer than predicted operation at room temperature [18]. As the QDs are spontaneously nucleated, their size can not be actively controlled. The resulting size fluctuations in the QD ensemble cause wavelength variations. The low QD density also results in a smaller gain than in quantum well active regions. Finally, non-radiative recombination due to defects caused by the lattice mismatch can decrease the laser performance and lifetime.



GaAs Substrate

Figure 10: Formation of quantum dots.

The final alloy that can be grown lattice matched to GaAs is GaAsSbN [19]. The emission wavelength from GaAsSb QWs can reach out to 1.25 μm , and adding a small quantity of nitrogen is enough to achieve 1.3 μm emission. However, the size difference between antimony and nitrogen is bigger than the size difference between arsenic and nitrogen, thus it is expected that GaAsSbN alloys will be more prone to phase segregation than GaInNAs [20]. This alloy is also a mixture of three group V elements and compositional control will likely be more challenging than alloys with either one or two group V elements.

1.4 Properties of nitrides and arsenides

The properties of nitrides and arsenides are significantly different (see Table 1) and result from the significant size and electro-negativity differences between nitrogen and arsenic atoms. These differences result in phase segregation, hence the challenge in the development of group III nitride-arsenides is avoiding phase segregation during growth and consequent thermal processing treatments.

| | GaN | GaAs | InN | InAs |
|---|--------------------------|--------------------------|------------------------------|-------------------------------|
| Crystal structure | Wurtzite | Zinc-Blende | Wurtzite | Zinc-Blende |
| Lattice Parameter | a = 3.18 Å c = 5.16 Å | a = 5.6533 Å | a = 3.5446 Å c = 5.7034 Å | a = 6.0583 Å |
| Energy Gap | 3.44 eV | 1.428 eV | 2.07 eV | 0.358 eV |
| Electron Mobility | 440 cm ² /Vs | 9300 cm ² /Vs | 250 cm ² /Vs | 2000-3300 cm ² /Vs |
| Free Energy of Formation (ΔG_f^0) | -33.04 kcal/mol | -16.97 kcal/mol | -22.96 kcal/mol | -10.22 kcal/mol |

Table 1: Properties of nitrides and arsenides [21].

Nitrides and arsenides have different equilibrium crystal structures: wurtzite and zinc-blende, respectively. Arsenides have a larger volume per atom than nitrides and hence a smaller bandgap. They also have a smaller energy of formation. These different

properties for nitrides and arsenides can be explained by the different properties of nitrogen and arsenic atoms (see Table 2).

Nitrogen has a smaller atomic number than arsenic, and hence a much smaller atomic size. As the valence band configuration is the same, the size difference results a larger electro-negativity for nitrogen, which causes stronger bonds and larger bandgaps in the nitrides.

| | N | As |
|----------------------------------|------------------|--|
| Atomic Number | 7 | 33 |
| Electron Configuration | $1s^2 2s^2 2p^3$ | $1s^2 2s^2 2p^6 3s^2 3p^6 3d^{10} 4s^2 4p^3$ |
| Non-Polar Covalent Radius | 0.75 Å | 1.18 Å |
| Electro-Negativity | 3.05 | 2.18 |

Table 2: Properties of arsenic and nitrogen [22].

1.5 Outline of the Dissertation

The outline of this thesis is as follows:

Chapter 2 presents the growth of nitride-arsenide materials. It begins by describing the growth technique used, molecular beam epitaxy (MBE), and lattice mismatch issues encountered during growth of III-V hetero-junctions. Next, we discuss more specifics related to nitride-arsenide growth i.e. generation of atomic nitrogen, control of nitrogen composition, and avoiding phase segregation. We conclude by contrasting MBE with other growth techniques.

Chapter 3 discusses the optical and crystal quality of these nitride-arsenides. First the change of bandgap with nitrogen concentration will be determined. It will be shown that nitride-arsenides have to be annealed to increase the luminescence efficiency but that this anneal also shifts the emission to shorter wavelengths. Mechanisms responsible for this behavior will be discussed.

Chapter 4 will use the observations of Chapter 3 to design a structure that enables 1.3 μm emission.

Finally, Chapter 5 concludes with a summary and suggestions for future work.

1.6 Summary

GaInNAs alloys have important applications as they enable opto-electronic devices emitting at 1.3 μm on GaAs substrates and have several advantages over the current state-of-the-art material system, GaInAsP. However, the growth of these alloys is a challenge as the different size and electron affinity of nitrogen and arsenic responsible for these beneficial bandgap properties might also cause phase segregation.

Chapter 2: Molecular Beam Epitaxy Growth of Nitride-Arsenides

This chapter presents the growth of nitride-arsenides. First, we describe molecular beam epitaxy (MBE) the growth technique utilized in this research and lattice mismatch issues encountered during growth of III-V hetero-junctions. Next, we discuss more specifics related to the nitride-arsenide growth i.e. generating atomic nitrogen, controlling the nitrogen composition, and avoiding phase segregation. This provides the knowledge needed to discuss the advantages of the molecular beam epitaxy growth of nitride-arsenides over metal organic chemical vapor deposition of nitride-arsenides.

2.1 Growth of III-V materials for hetero-junction devices

2.1.1 Molecular Beam Epitaxy

2.1.1.1 Theoretical Background

In order to make hetero-junction devices based on III-V materials, it is necessary to grow single-crystal, closely lattice matched layers with precisely controlled thickness and doping concentration. The three most commonly used epitaxial growth techniques are liquid-phase epitaxy (LPE), molecular beam epitaxy (MBE), and metal-organic vapor-phase deposition (MOCVD). In LPE and MOCVD, the growth occurs under near equilibrium conditions from a liquid and a flowing gas respectively. MBE is a technique to grow thin epitaxial structures by adsorption and subsequent surface reaction of vapor species in an ultra high vacuum environment (UHV).

The development of MBE resulted from Arthur's [23] study of the reaction kinetics of gallium and As₂ beams on GaAs surfaces. Cho's [24] adaptation of electron

diffraction to monitor the GaAs surface structure during the growth advanced the deposition technique well beyond simple vacuum evaporation to a much more precisely controlled technique. Since 1978, MBE systems have been commercially available. The different aspects of this growth technique are shown in Figure 11.

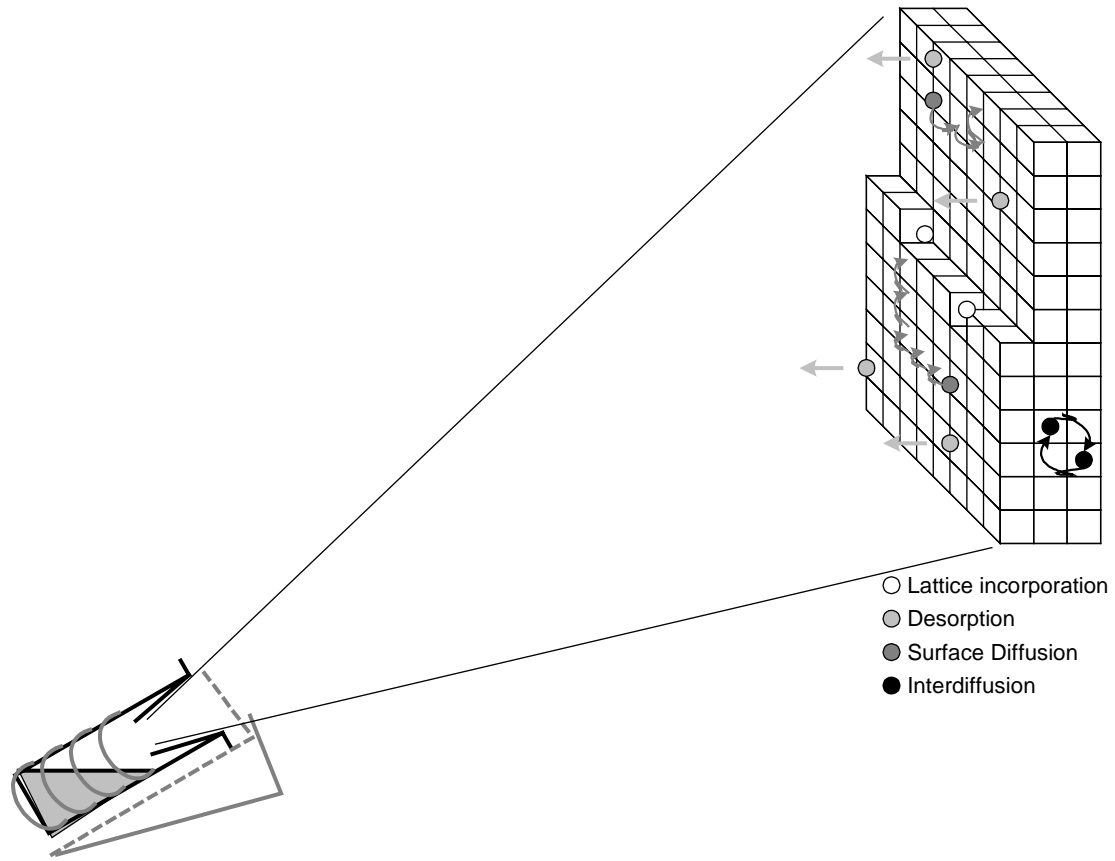


Figure 11: Schematic illustration of the processes occurring during MBE.

The pressure in an idle MBE growth chamber is typically 10^{-11} - 10^{-9} Torr. Ion-pumps, cryo-pumps, and a liquid nitrogen cryo-shroud around the interior of the chamber guarantee UHV conditions and virtually eliminate any memory effects during growth. To maintain the UHV, contamination during the wafer loading process must be avoided. For that purpose, an MBE system has a separate loading chamber in which the wafers are baked and a transition tube that connects the loading chamber and the growth chamber. This UHV is necessary for three reasons. The UHV allows the growth of films with extremely low impurity concentrations: at these low pressures, a surface will stay clean for ~ 7 h; while in the atmospheric environment it will acquire a mono-layer of adsorbed gas in 4 ns (assuming unity sticking coefficient). Another unique advantage of the UHV

environment is the capability to use surface sensitive diagnostic monitoring techniques that require vacuum: reflection high-energy electron diffraction (RHEED), and Auger electron spectroscopy (AES). A third feature of the UHV is that species in the growth chamber are in the molecular flow regime. In other words, they do not collide or react with one another on their way to the substrate, and species that miss or leave the substrate are pumped away nearly immediately.

The sources are Knudsen-effusion-cells forming the “molecular beam” by thermal evaporation (for the group III elements) or sublimation (for As_4). The solid or liquid source material is held in an inert pyrolytic boron-nitride crucible heated by radiation. The amount of material evaporated is quantified by the beam flux. The temperature of the cell monitored with a thermocouple controls the beam flux. As_4 can also be cracked to As_2 in a cracker cell. The cracker consists of a low temperature sublimator section and a high temperature cracking section. The temperature of the sublimator section determines the arsenic flux. In more modern crackers, a valve is put between the sublimator and the cracker section to control the arsenic flux. Shutters in front of these cells enable starting and stopping the growth, and controlling composition and doping with monolayer accuracy. To grow GaAs, the gallium and arsenic shutter are opened; to grow GaNAs the gallium, arsenic, and nitrogen shutters are opened; and to grow GaInNAs the gallium, indium, nitrogen and arsenic shutter are opened. By choosing the appropriate cell temperature for the group III elements, epitaxial films of the desired chemical composition are obtained. With a growth rate of ~ 1 monolayer per second and the ability to open and close these shutters in a fraction of a second, growth can be controlled on a submonolayer scale.

Because of the high vacuum, MBE growth is carried out under conditions far from thermodynamic equilibrium and is governed mainly by the kinetics of the surface occurring when the impinging beams react with the outermost atomic layers of the substrate crystal. A series of surface processes are involved in MBE growth. First, the impinging molecules adsorb on the surface through chemisorption for the group III atoms and physisorption for As_2 and As_4 . Under typical growth conditions the group III atoms tend to have sticking coefficients close to unity; this allows precise control of the composition by the evaporation rate. The group III atoms migrate on the surface; a

typical hopping rate is 10^4 hops/s. When the atoms find a low energy site, they may incorporate into the crystal lattice of the substrate. To obtain smooth surfaces, the growth occurs in a layer-by-layer mode, and the ad-atoms attach at ledges or kinks. Some of the supplied As_2 will dissociate. The fact that the group V molecules are much more volatile than the group III atoms allows stoichiometric growth without precise control of the group V flux. If the substrate is sufficiently hot (typically 625 °C), the group V molecules will re-evaporate unless there is a group III atom with which to form the compound. Growth normally proceeds under arsenic rich conditions with V/III flux ratio of 10-25; a lot of As_2 is desorbed from the substrate. Finally, if growth occurs at elevated temperatures, some inter-diffusion of deposited species can occur.

The different adsorption, dissociation, and desorption steps involved in growth of GaAs on GaAs (100) have been described in detail by Herman and Sitter [25]. For typical growth conditions, the As-rich GaAs (100) (2×4) reconstruction (see Figure 12) is an important step in the growth process. This has been experimentally observed using RHEED.

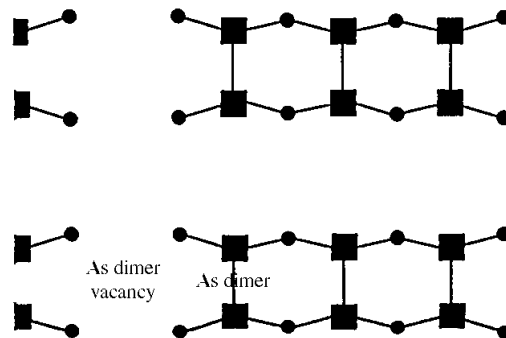


Figure 12: Planar view of the As-rich GaAs (100) (2×4) surface unit cell. The As atoms (■) form three dimers per unit cell. The dimer vacancy exposes four gallium atoms (●) in the second layer.

2.1.1.2 Description of growth conditions

All growths were done on two-inch GaAs substrates. Wafers are loaded onto substrate holders. The Varian Gen-II MBE system consists of a load chamber, a transition tube and a growth chamber (see Figure 13). Holders with wafers are first placed in a load chamber and baked at 400 °C at a pressure of 10^{-6} Torr for 1 hour to drive off water vapor. They are then transferred through the transition tube into the growth chamber.

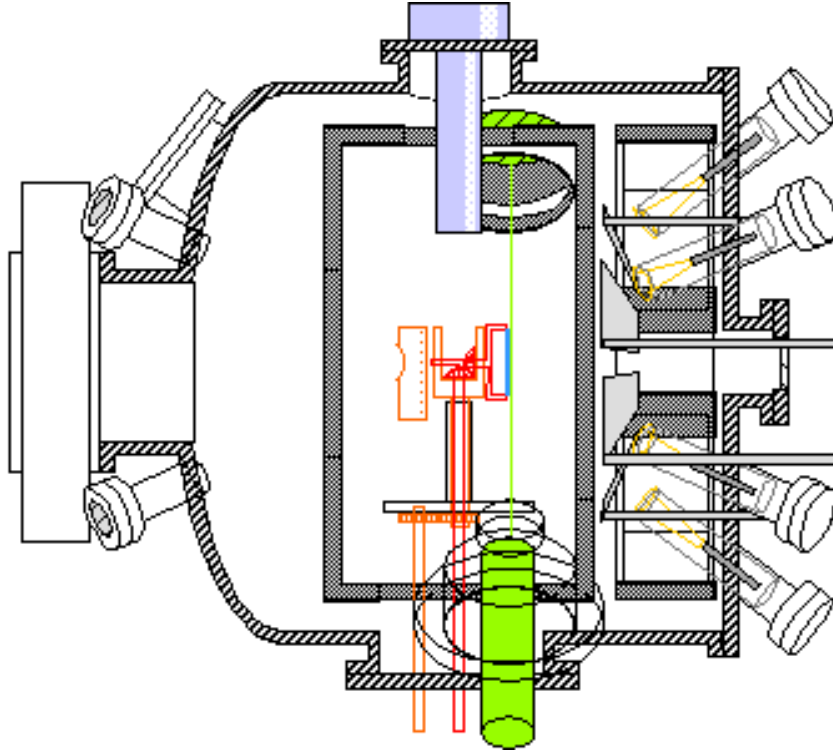


Figure 13: MBE growth chamber.

The growth chamber (see Figure 13) contains 8 effusion cells or source furnaces. The growth rates used for gallium, aluminum, and indium, are 0.1-0.8 mono-layers/s, 0.1-0.8 mono-layers/s, and 0.2-0.3 mono-layers/s, respectively. The growth chamber also contains two valved arsenic crackers that supply As_2 with a beam flux equal to 20 times the total beam flux of the group III elements. A radio frequency (rf) plasma was used to supply atomic nitrogen (see section 2.2). The other sources are beryllium and silicon cells for p- and n-type doping, respectively. Growth rate calibrations are performed each time of new source material is loaded. The beam flux is measured using a Bayard-Alpert ion gauge in the growth chamber. The ratio between the measured beam flux and the growth rate are determined from RHEED oscillations, reflectivity measurements and X-ray diffraction data.

The substrate holders are radiatively heated for growth. The substrate temperature control is very important for the growth of nitride-arsenides for two reasons: to avoid phase-segregation (see section 2.4.3) and to optimize the laser performance [26].

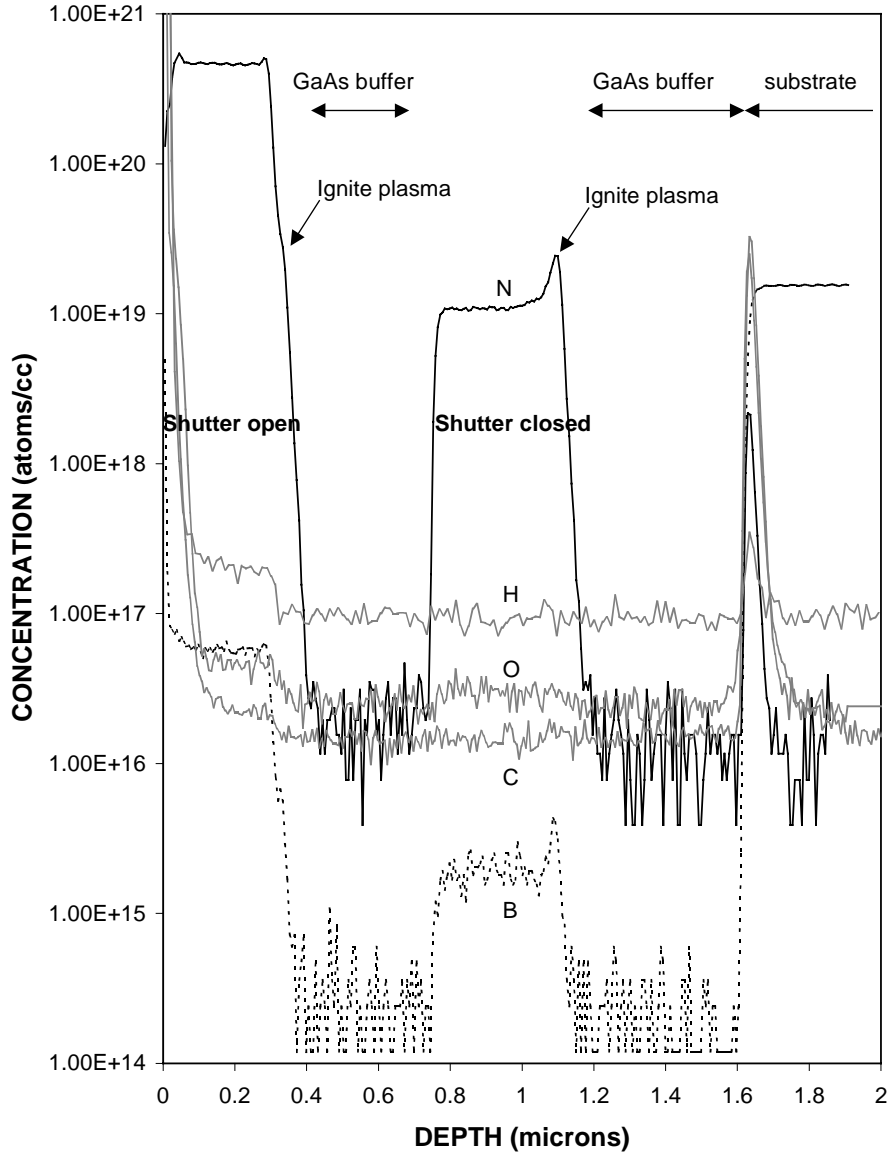


Figure 14: Nitrogen, hydrogen, oxygen, carbon, and boron concentration profile measured by SIMS in a CAMECA IMS 4.5f instrument using cesium ion bombardment. The sample structure consists of a GaAs substrate, GaAs buffer layer, GaNAs layer grown with rf plasma running but shutter in front of it closed, GaAs buffer layer, and GaNAs layer grown with rf plasma running and shutter in front of it open.

Secondary ion mass spectroscopy (SIMS) has been used to investigate the impurity concentration of the MBE grown material. As seen in Figure 14, the measured impurity concentration in the GaAs buffer layer is the same as in the GaAs substrate and likely caused by the background in the SIMS instrument. During the periods where nitrogen gas flows into the growth chamber i.e. when the plasma is running, there is a slight increase in background impurity concentration due to both impurities in the nitrogen gas and contamination from the plasma cell containing pyrolytic boron nitride

(PBN). However, the concentration of hydrogen, oxygen, carbon, and boron in the film remains below $1 \times 10^{17}/\text{cm}^3$ throughout the whole film. Figure 14 also shows that additional nitrogen is incorporated just when the plasma is ignited as well as when running the plasma with a closed shutter. This is not expected from conventional MBE growth; it indicates that N_2 is not effectively pumped by the cryo-shroud because its vapor pressure at 77K is not negligible [27] so that it gets incorporated even when there is no line of sight between the nitrogen cell and the substrate. When igniting the plasma (when no atomic nitrogen is formed yet), this additional nitrogen incorporation results in defects because the supplied nitrogen are not the right species (see Figure 15). A defect is generated when igniting the N_2 plasma during the initiation of the GaNAs growth; this same defect accumulates at the normal interface.

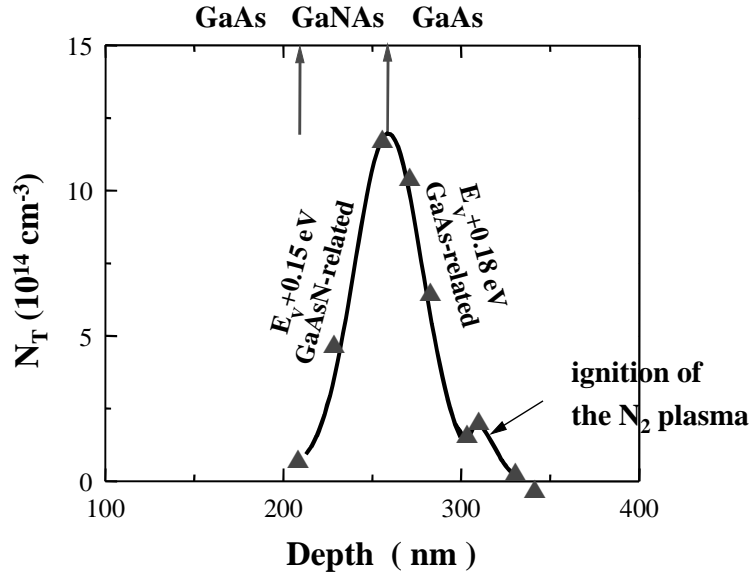


Figure 15: Defect concentration versus depth in a GaAs/GaN_{0.03}As_{0.97}/GaAs structure measured by deep level transient spectroscopy (DLTS).

The ability to achieve abrupt interfaces is demonstrated in the high resolution TEM image in Figure 16. The Ga_{0.8}In_{0.2}N_{0.015}As_{0.985} quantum well (QW) is darker due to mass contrast. The observed oscillations in the sum intensity trace correspond to monolayers. There are 22 monolayers in the QW. The quantum well boundary is 2 to 3 monolayers thick.

2.1.2 Lattice Mismatch

As MBE is an epitaxial growth technique, the arrangement of the atomic species of the growing film mimics the arrangement of atoms in the underlying layer. In some

cases, a crystallographically coherent interface forms with the atoms of the growing film and the underlying layer in perfect “registry” even if the lattice parameter from the bulk and the film differ. In that case, the film will be strained, and its electronic and opto-electronic properties are altered by strain-induced changes in the electronic band structure [28]. On the other hand, if the layer is semi-coherent with the substrate, dislocations that compensate for the lattice parameter misfit are present and degrade the performance of light emitting devices significantly. Dislocations act as a non-radiative recombination centers (see section 1.2.1). Efficient opto-electronic devices require dislocation-free material.

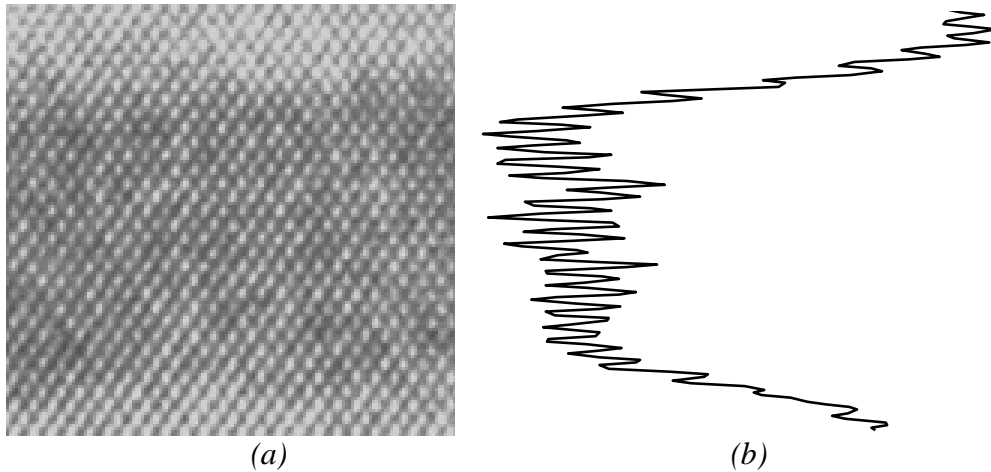


Figure 16: (a) High resolution TEM image of a $Ga_{0.8}In_{0.2}N_{0.015}As_{0.985}$ quantum wells with GaAs barriers. (b) Intensity in the image summed over the width of the picture. The oscillations indicate the position of the atom planes.

If the layers are sufficiently thin, the mismatch is entirely accommodated by uniform strain and the lattice parameter of the epi-layer is equal to that of the substrate parallel to the interfacial plane (see Figure 17). The film can relax somewhat due to Poisson contraction resulting in a change of lattice parameter in the out of plane direction. The elastic strain energy stored in this geometry increases with film thickness. At film thicknesses greater than the critical thickness, h_c , it becomes energetically favorable to reduce the stored elastic strain energy by the introduction of misfit dislocations allowing the film to relax to its strain free lattice parameter (see Figure 17). To avoid this dislocation formation in the growth of opto-electronic devices, the thickness of the layers must stay below the critical thickness.

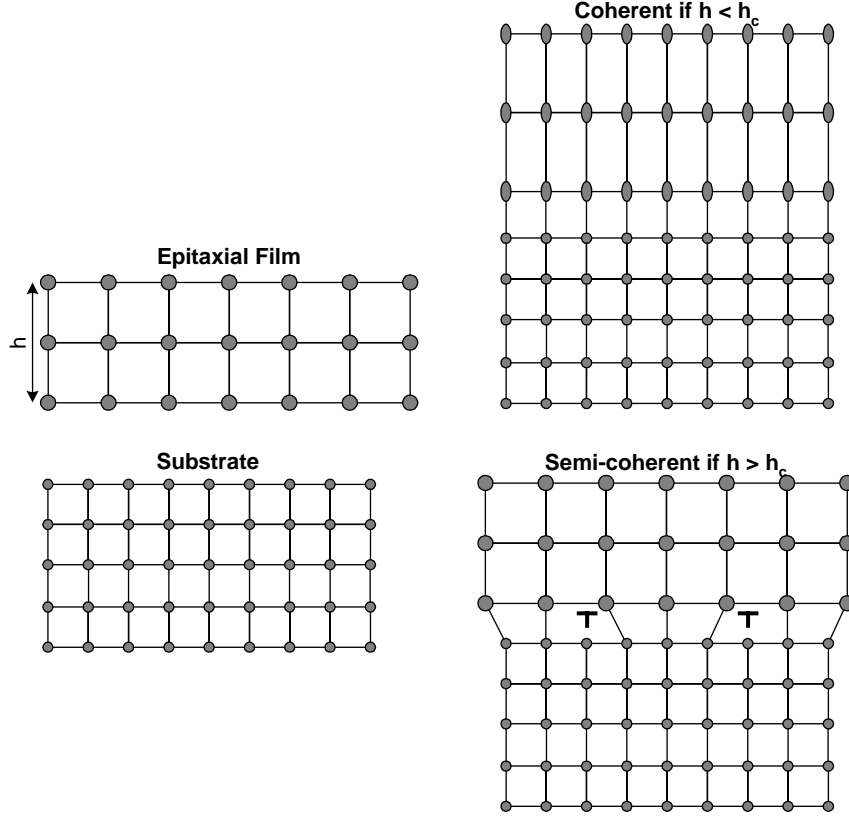


Figure 17: Schematic illustration of the critical thickness concept for the case of a film with a bigger lattice parameter than the substrate.

Matthews and Blakeslee [29] have developed a formula to predict the equilibrium critical thickness in strained semiconductor hetero-structures. For a film on a substrate this critical thickness is given by:

$$h_c = \frac{b(1-\nu\cos^2\theta)}{8\pi(1+\nu)\epsilon\cos\lambda} \ln\left(\frac{\alpha h_c}{b}\right)$$

where b is the length of Burgers vector, ν is the Poisson ratio, θ is the angle between the Burgers vector and dislocation line, ϵ is the linear strain between the film and the substrate, λ is the angle between the Burgers vector and the normal to the dislocation line direction in the interface, and α is a factor accounting for the dislocation core energy. For III-V zinc-blende semiconductors, the $\{111\}$ plane is the slip plane and the most commonly observed dislocations have a Burgers vector of $\frac{1}{2}[110]$. Therefore, the length

of the Burgers vector is $b = \frac{a}{\sqrt{2}}$ (with lattice parameter a), and θ is 60° . For a

dislocation at a (100) interface, $\cos\lambda = 0.5$. For GaAs, α is around 4. The linear strain ϵ between the epi-layer and the substrate is defined as:

$$\epsilon = \frac{a_f - a_s}{a_f}$$

with a_f and a_s the in-plane lattice parameters of the film and the substrate, respectively. When the strained film is buried beneath another thick layer of material that has the same lattice parameter as the substrate, the equation reduces to [30]:

$$h_c \sim \frac{b(1 - \nu \cos^2\theta)}{4\pi(1 + \nu)\epsilon \cos\lambda} \ln\left(\frac{\alpha h_c}{b}\right)$$

The capping of strained layers results in an increase of the critical thickness by a factor of approximately two. This is of great benefit in post-growth processing of practical strained layer devices. The above formula results in critical thicknesses of 500 Å, 100 Å, and 150 Å for GaAs_{0.97}N_{0.03}, In_{0.3}Ga_{0.7}As, and Ga_{0.7}In_{0.3}As_{0.98}N_{0.02} respectively.

The experimentally determined critical thickness is often greater than the Matthews and Blakeslee prediction and several models have been developed in an attempt to more closely match the observed data [30]. They take into account the kinetics of misfit dislocation formation.

2.2 Optimization of the radio frequency plasma

An important element in the growth of nitride-arsenides is the nitrogen source. The choice of a rf plasma cell was based on the following considerations. As mentioned before, the equilibrium bulk solubility of N in GaAs is very low (see section 2.4) and nitrogen-containing reagents are very stable. To allow the nitrogen to react and incorporate into the growing surface, it is necessary to supply a very reactive nitrogen species: atomic nitrogen. Atomic nitrogen is generated with a radio frequency (rf) plasma to minimize ion damage to the surface of the growing film [31].

Initial rf plasma sources were designed to grow GaN, and produced quite high nitrogen fluxes. We worked with an SVT cell and modified the exit aperture of it to allow plasma operation at low nitrogen flow rates (0.1-0.8 sccm) required to obtain nitride-arsenides with only a few percent of nitrogen. This aperture is a PBN plate with

nine holes of diameter 0.2 mm. These dimensions are based on the desired conductance to achieve enough pressure in the cell to ignite the plasma. The nine holes are necessary to maximize the uniformity of the generated atomic nitrogen flux.

A nitrogen gas supply system has been built to control the flow of nitrogen into the MBE chamber (see Figure 18). The nitrogen mass flow controller, the valve to the turbo pump, and the leak valve to the MBE chamber control the nitrogen flow into the chamber. With the shutter in front of the nitrogen cell closed, the plasma is ignited in the following way:

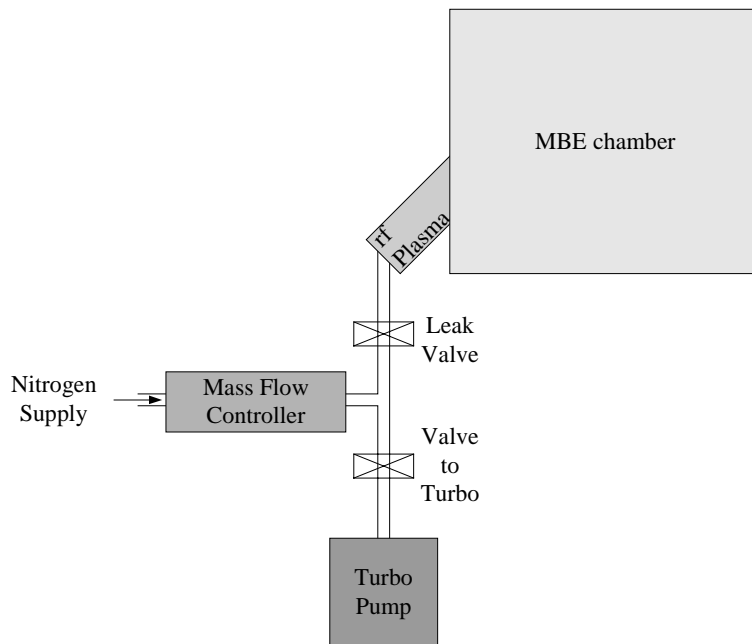


Figure 18: Schematic picture of the nitrogen gas supply.

- With the leak valve closed and the valve to the turbo pump open, the nitrogen flow through the mass flow controller is set to 0.625 sccm. All this nitrogen is pumped away with the turbo pump and nothing flows into the MBE chamber.
- When the flow is stable, the power to the plasma is slowly ramped to 300 W.
- The leak valve is opened. Because its aperture is small, most of the supplied nitrogen gas is still pumped away by the turbo pump. The pressure in the MBE chamber is typically 1×10^{-6} Torr.
- The valve to the turbo pump is closed. At this time, all the supplied nitrogen flows into the MBE chamber. When the pressure in the chamber is around 1×10^{-5} Torr, the plasma ignites. However, because the pressure in the plasma cell is high (~ 10

mTorr), the mean free path of the species is short and they do not gain enough energy to form atomic nitrogen.

- Next, the nitrogen flow is decreased to the flow rate used during the growth (0.25 sccm). At a flow rate of approximately 0.3 sccm, the plasma intensity increases suddenly. At this point, the pressure in the plasma is low enough and the mean free path of the nitrogen species is long enough to create atomic nitrogen. The pressure in the chamber drops.

This start-up procedure results in a variation of the nitrogen pressure in the MBE chamber with the highest pressure reached when the plasma is ignited. This high nitrogen pressure causes in a higher nitrogen concentration in the film when the plasma is ignited (see Figure 14 and Figure 56 (c)). The nitrogen incorporation decreases when the nitrogen flow is decreased to the value used during the growth. Of course, the nitrogen incorporation increases again when the shutter in front of the plasma is opened.

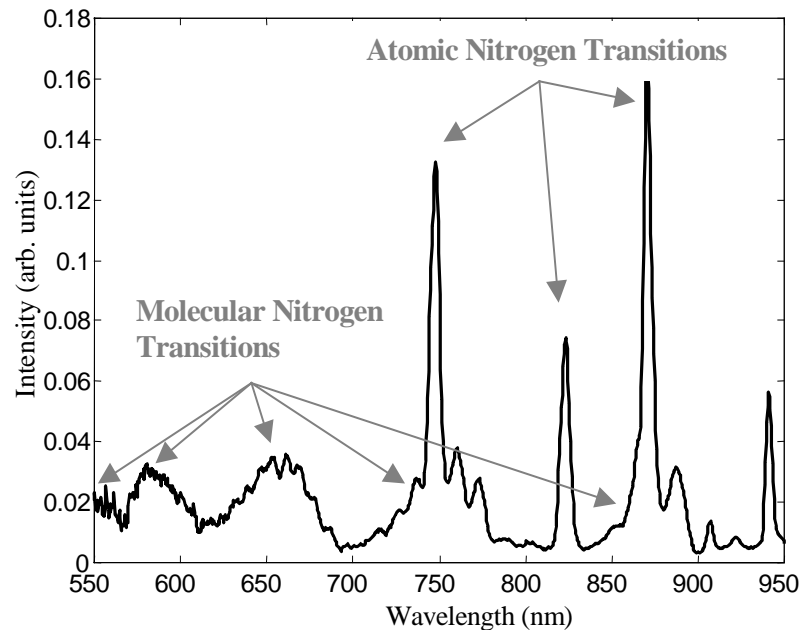


Figure 19: Emission spectrum of the rf nitrogen plasma for a nitrogen supply of 0.25 sccm and power of 300 W.

The operation of the rf plasma has been optimized to maximize the generation of atomic nitrogen within the limits of stable plasma operation. The plasma conditions that maximize the amount of atomic nitrogen versus molecular nitrogen are determined using the emission spectrum of the plasma (see Figure 19). The amount of molecular nitrogen is determined from the intensity of the first set of bands at approximately 550, 580, and

650 nm; the intensity in the bands at 740, 820 and 870 nm is proportional to the amount of atomic nitrogen present in the plasma [32]. Hence, the ratio of the peak intensity due to an atomic nitrogen transition and the peak intensity due to a molecular nitrogen transition is proportional to the relative amount of atomic versus molecular nitrogen in the plasma. The total intensity integrated from 550 to 950 nm is proportional to the total amount of excited nitrogen in the plasma.

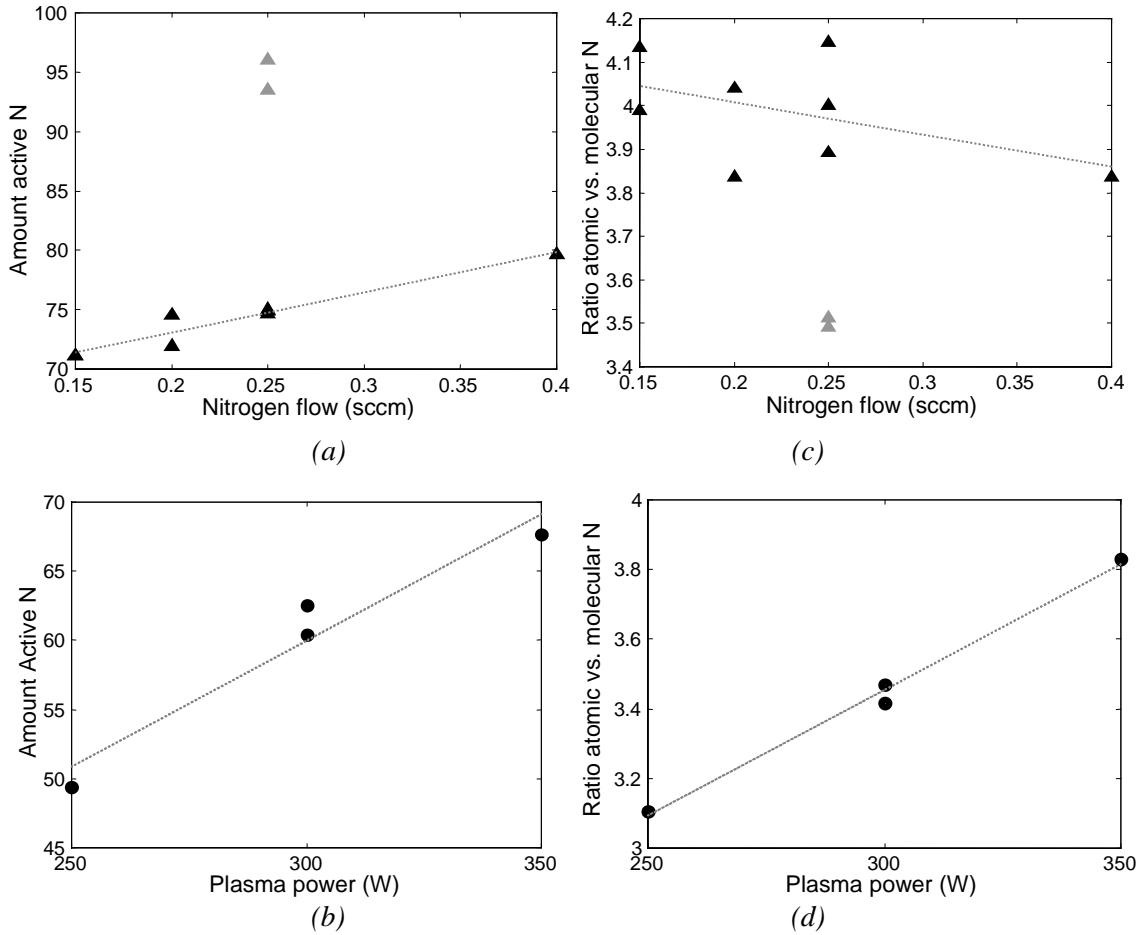


Figure 20: Plasma operation as function of nitrogen flow and plasma power. The amount of excited nitrogen in the plasma as function of (a) nitrogen flow and (b) plasma power. The ratio of atomic versus molecular nitrogen concentration in the plasma as function of (c) nitrogen flow and (d) plasma power. The gray points in (a) and (c) are data obtained when the nitrogen flow was turned down to 0.15 sccm and then back to 0.25 sccm.

To optimize the plasma, we have investigated how the amount of excited nitrogen and ratio of atomic versus molecular nitrogen in the plasma vary with nitrogen flow rate and plasma power. Figure 20(c) shows that the start-up procedure of the plasma influences the amount of atomic nitrogen in the plasma. To maximize the generation of

atomic nitrogen, the nitrogen flow should be decreased to the desired value after ignition. When the flow is increased after that, the plasma changes to a different operating mode and results in a lower ratio of atomic versus molecular nitrogen as shown by the gray points in Figure 20(c). As shown in Figure 20(a) and Figure 20(c), the total amount of excited nitrogen in the plasma increases with increasing nitrogen flow because more nitrogen species are supplied. The ratio of atomic versus molecular nitrogen tends to decrease with increasing nitrogen flow. At the higher nitrogen flow rates, the pressure in the plasma cell is higher resulting in a shorter mean free path. Therefore, the nitrogen molecules do not gain enough energy to break the N-N bond and the ratio of atomic versus molecular nitrogen decreases. With increasing plasma power, both the ratio of atomic nitrogen versus molecular nitrogen and the total amount of excited nitrogen increase (see Figure 20(b) and Figure 20(d)). For our plasma source design, the plasma power is more effective than the nitrogen flow rate in controlling the generation of atomic nitrogen.

For all growths described in later chapters, the nitrogen flow rate is fixed at 0.25 sccm. Lower flow rates give rise to a larger ratio of atomic versus molecular nitrogen but the plasma source does not remain stable at these lower flow rates. The plasma power is set to 300 W for all the reported growths. A higher power results in higher ratios of atomic versus molecular nitrogen, but the plasma tends to heat up too much at these higher powers and there was concern about source or vacuum failure.

2.3 Control of nitrogen concentration

As explained before (see section 2.2), the rf plasma operation has been optimized within the range of stable conditions by setting the nitrogen flow at 0.25 sccm and the plasma power at 300 W. These conditions were used for all the described growths. The next important step in the growth of nitride-arsenides is the control of the nitrogen composition with these fixed plasma conditions.

Changing the group III growth rate and keeping the plasma power fixed at 300 W and the nitrogen flow fixed at 0.25 sccm controls the nitrogen concentration in the film. Figure 21 shows that the nitrogen concentration is inversely proportional to the GaAs

growth rate. At substrate temperatures of 500 °C or below and an As₂ overpressure of twenty times the gallium pressure, N₂ formation is limited because the amount of atomic nitrogen is small compared to the As₂ and gallium overpressures in the MBE system. Moreover, atomic nitrogen is very reactive. Hence, all the supplied atomic nitrogen is incorporated to form GaNAs. This result suggests that the GaInNAs system might have some advantages in terms of yield and reproducibility compared to the arsenide-phosphide system where the phosphorus concentration is strongly dependent on vapor composition and growth temperature (see Figure 9) [33,34].

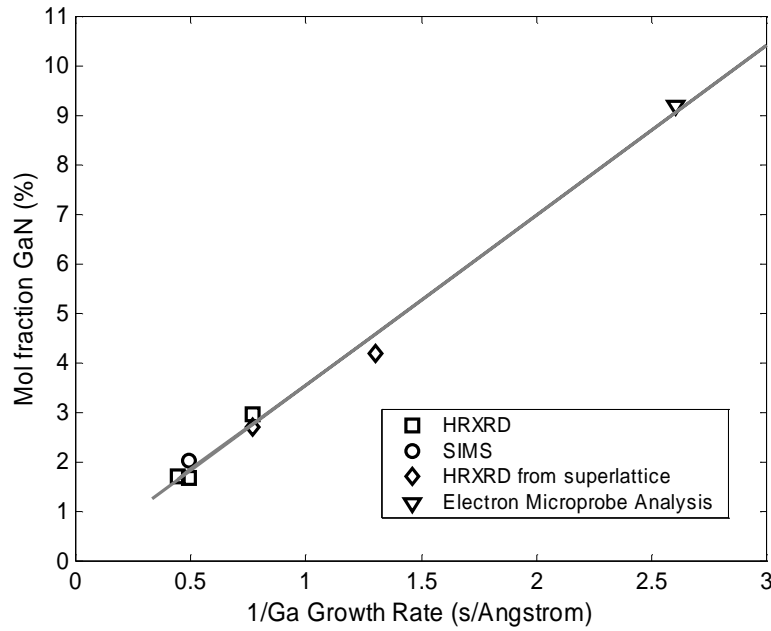


Figure 21: Concentration of nitrogen in GaNAs films as function of the GaAs growth rate. The nitrogen concentration was measured by HRXRD, SIMS, and electron microprobe analysis. The nitrogen plasma was operated with a power of 300 W and a nitrogen flow of 0.25 sccm.

A challenge faced when taking these data has been the choice of the analysis tool to measure the nitrogen concentration. The analysis tools utilized are high resolution X-ray diffraction (HRXRD), secondary ion mass spectroscopy (SIMS), and electron probe X-ray microanalysis (EPMA).

HRXRD measures the lattice parameter of the film. The lattice parameter is related to the position of the constructive interference X-ray peak by Bragg's law:

$$n\lambda = 2d_{hkl}\sin\theta \quad [35]$$

where λ is the wavelength of the used X-ray source, and d_{hkl} is the spacing between the hkl planes, which for cubic crystals is related to the lattice parameter, a , as

$$\frac{1}{d_{hkl}^2} = \frac{h^2 + k^2 + l^2}{a^2} \quad [35].$$

All the measured films are not relaxed as indicated by the position of the film 224 peak with respect to the GaAs 224 peak (see Figure 22). Hence, the equilibrium unstrained lattice parameter (a_{eq}) of the cubic crystal can be calculated from the measured out-of-plane lattice parameter (a_{004}) as:

$$\sigma_z = 0 = 2.C_{12}.\epsilon_{in-plane} + C_{11}.\epsilon_{out-plane} \text{ or } a_{eq} = \frac{2 \frac{C_{12}}{C_{11}} a_{GaAs} + a_{004}}{(1 + 2 \frac{C_{12}}{C_{11}})}$$

where $\epsilon_{in-plane}$ is the in-plane strain which is equal to $\frac{a_{GaAs} - a_{eq}}{a_{eq}}$ if the film is not relaxed,

$\epsilon_{out-plane}$ is the out-of-plane strain which is equal to $\frac{a_{004} - a_{eq}}{a_{eq}}$ (a_{GaAs} is the lattice

parameter of GaAs), and σ_z is the strain in the out-of-plane direction. C_{11} and C_{12} are the stiffness coefficients; $2 \frac{C_{12}}{C_{11}}$ is around 0.9 for all III-V materials [36]. Since Vegard's

law is valid for low concentrations in the nitride-arsenide material system [3], it can be used to calculate the nitrogen concentration from the unstrained lattice parameter.

For nitrogen concentrations below 5 %, the nitrogen concentration can be calculated from the lattice parameter of the unrelaxed film. For higher nitrogen concentrations a unrelaxed single film is too thin for accurate analysis (as it results in too low X-ray counts). The concentration is determined by comparing the measured HRXRD spectrum from a GaAs/GaNAs superlattice with a spectrum simulated from the High Resolution Simulation software supplied by Phillips [37].

SIMS determines the nitrogen concentration from the measured yield of secondary ions (GaN ions) after bombarding the sample with cesium ions. Due to matrix effects, the accuracy of quantification with SIMS is seldom better than 5 % especially at concentrations above 4 % [38]. The data are only meaningful if the measurements are calibrated with reliable standards in the same concentration range.

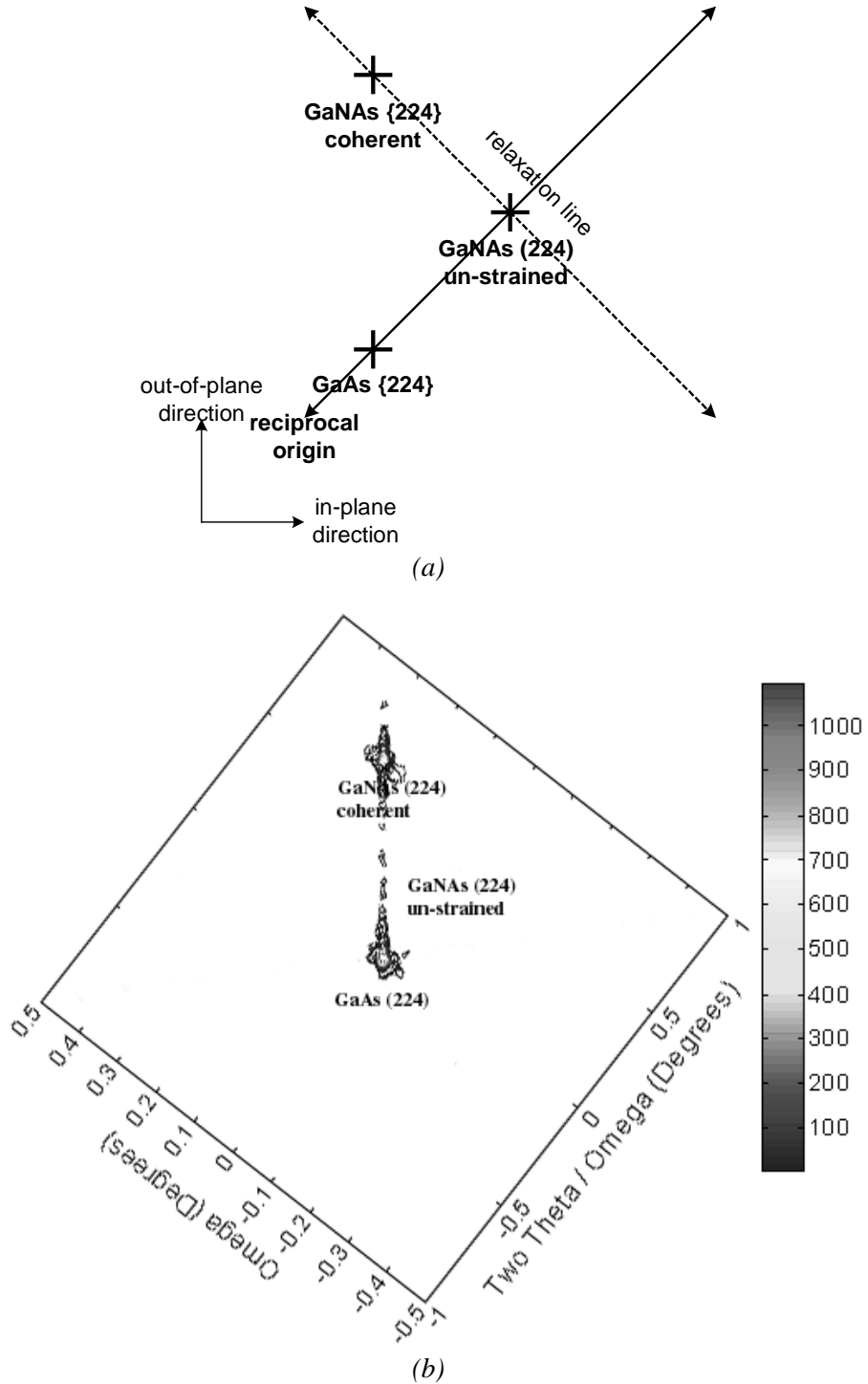


Figure 22: (a) Region of the reciprocal space map near the (224) reciprocal lattice point (b) Reciprocal space contour map of 2500 Å thick, $\text{GaN}_{0.025}\text{As}_{0.975}$ on GaAs.

EPMA is an elemental analysis technique based upon bombarding the specimen with a focused beam of energetic electrons to induce emission of characteristic X-rays. As the thickness of our films is limited (because the nitrogen plasma can only run for a

limited time due to heating), only films with a GaN molecular fraction above 10 % give rise to enough counts to determine the concentration accurately.

In addition to the above techniques, X-ray photoelectron spectroscopy (XPS), Auger electron spectroscopy and nuclear reaction analysis (NRA) can be used to determine the nitrogen concentration.

XPS uses mono-energetic X-rays to bombard the sample, causing ejection of electrons. This technique has proven to be challenging for several reasons. For the most commonly used X-ray source (aluminum) a gallium Auger peak overlaps with the N(1s) peak, making quantitative analysis difficult (see Figure 23). This technique is very surface sensitive (see Figure 24) and the argon sputtering used to remove the surface contamination layer depleted the nitrogen (see Figure 23). Hence, XPS measurements are not useful for the above analysis.

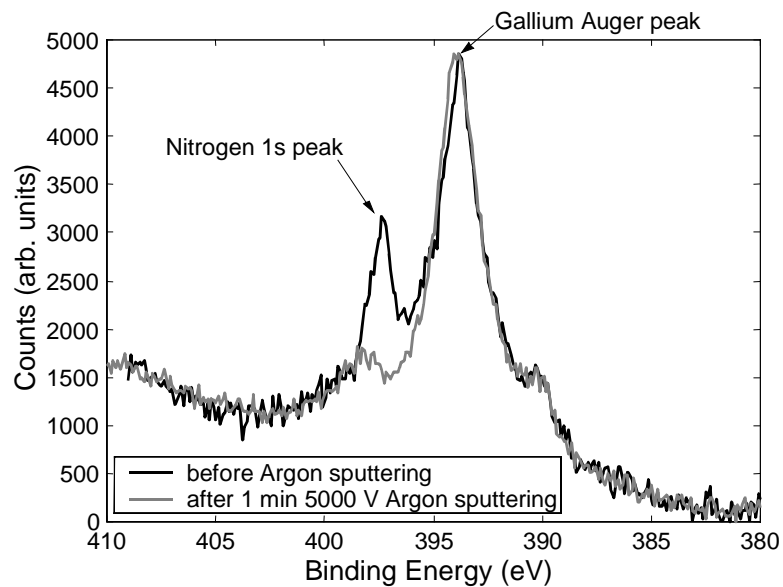


Figure 23: XPS signal from a 650 Å $\text{GaN}_{0.1}\text{As}_{0.9}$ film on GaAs substrate before and after Argon sputtering.

AES uses a focused electron beam to create secondary electrons near the surface. Quantitative analysis requires standards. Figure 25 shows that for elements with a low atomic number the Auger yield is large. Unfortunately, this technique is also really surface sensitive (see Figure 24) and removing the surface contamination layer by argon sputtering is again not an option as this also depletes the nitrogen.

NRA uses a beam of charged particles with energy around 1 MeV to bombard the sample producing protons, deuterons, tritons, He, α particles or γ rays. The yield of these

particles is converted to concentrations. The reactions that can be used to detect nitrogen are: $^{14}\text{N} + \text{deuteron} \rightarrow \alpha + ^{12}\text{C}$, $^{14}\text{N} + ^3\text{He} \rightarrow \text{proton} + ^{16}\text{O}$ or $^{14}\text{N} + ^3\text{He} \rightarrow ^4\text{He} + ^{13}\text{N}$. In the first reaction, the acceleration of deuterons creates neutrons resulting in a poor signal to noise ratio. The cross-section for the second and third reactions is small, causing low particle counts. These considerations together with the fact that this technique is not easily available, have made us choose HRXRD, SIMS, and EPMA for this analysis. We use the NRA technique for other purposes (see section 3.2.4.3).

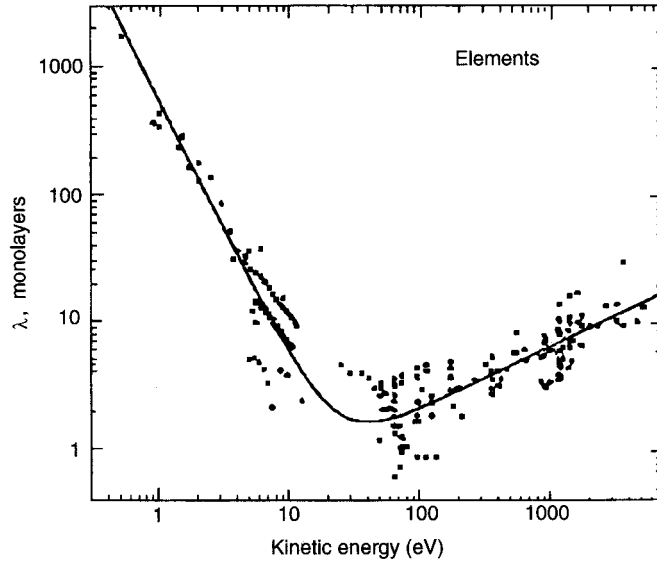


Figure 24: Escape depth of electrons during AES or XPS [38].

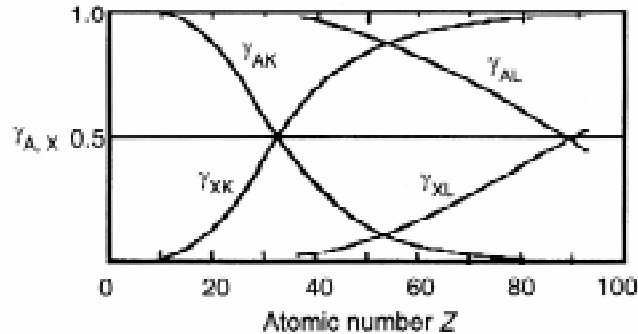


Figure 25: Emission probability of an Auger electron (A) or photon (X) [38].

2.4 Growth temperature and phase segregation

As mentioned in section 1.1, the different size and electron affinity of nitrogen and arsenic result in the existence of an extensive miscibility gap. The equilibrium mole

fraction of nitrogen in GaAs and InAs is only a fraction of a percent [3,7]. Since precipitates of a second phase can act as a center for non-radiative recombination, thermodynamic considerations are important to determine the growth conditions under which single-phase material can be formed. Once the alloy has been formed, phase segregation can sometimes be avoided by freezing in meta-stable or unstable solutions. Macroscopic calculations of the onset of phase segregation are based on the regular solution model. Alloy phase diagrams can also be obtained from first-principle calculations [39], however these are really computer intensive.

2.4.1 Regular solution model

The regular solution model provides valuable insight in the thermodynamic properties of solutions. It is convenient to classify the different models for solutions according to the strength of the interaction between the two components (see Table 3).

| Type of solution | Description of model | h_m | s_m |
|------------------|---|-----------------|---|
| Ideal | Two components interact with each other in the same way as they do among themselves | 0 | $-R[(1-x)\ln(1-x)+x\ln x]$ (exact) |
| Regular | Two components interact with each other substantially and differently from the way they interact among themselves | $\Omega x(1-x)$ | $-R[(1-x)\ln(1-x)+x\ln x]$ (approximate) |

Table 3: Description of various semi-empirical models of solutions and their corresponding molar enthalpies and entropies of mixing [40]. The molar Gibbs free energy of mixing is thus $g_m = h_m - TS_m$.

For an ideal solution, the entropy of mixing, s_m , is the entropy associated with the random mixing of the two components in a condensed phase. This entropy can be calculated from the number of ways the N_a “a” atoms can position themselves on $N_a + N_b$ lattice sites:

$$s_{m,\text{ideal}} = \frac{R}{N_a + N_b} \ln \left[\frac{(N_a + N_b)!}{N_a! N_b!} \right],$$

which can be simplified using Stirling’s approximation to:

$$s_{m,\text{ideal}} = -R[(1-x)\ln(1-x)+x\ln x]$$

where N_a is the number of “a” atoms, N_b is the number of “b” atoms, x is the concentration of “b” atoms in atomic percent, and R is the universal gas constant. For the regular solution, the entropy of mixing is still equal to the ideal entropy of mixing. This

assumption of random distribution is the most critical feature of the regular solution model. For regular solutions the two components should be chemically only slightly dissimilar so that they will mix very nearly randomly.

The regular solution model assumes that the atoms are distributed randomly on the sites of a three-dimensional lattice. With the number of “a-a” pairs N_{aa} , the number of “a-b” pairs N_{ab} , and the number of “b-b” pairs N_{bb} , one can calculate N_a , and N_b as:

$$ZN_a = 2N_{aa} + N_{ab} \text{ and } ZN_b = 2N_{bb} + N_{ab}$$

where Z is the coordination number i.e. the number of nearest neighbors of “a” and “b”. N_{ab} is equal to the chance of finding an “a” atom next to a “b” atom times the total number of pairs:

$$N_{ab} = (2x(1-x))\left(\frac{1}{2}ZN\right) = ZNx(1-x)$$

where $N = N_a + N_b$ is the total number of atoms. The enthalpy of the lattice is:

$$H = N_{aa}\epsilon_{aa} + N_{ab}\epsilon_{ab} + N_{bb}\epsilon_{bb} = \frac{1}{2}ZN_a\epsilon_{aa} + \frac{1}{2}ZN_b\epsilon_{bb} + N_{ab}\left[\epsilon_{ab} - \frac{1}{2}(\epsilon_{aa} + \epsilon_{bb})\right]$$

where ϵ_{aa} , ϵ_{bb} , and ϵ_{ab} designate the energies of the “a-a”, “b-b” and “a-b” pairs respectively. As $\frac{1}{2}ZN_a$ is the total number of “a-a” pairs in pure “a” before mixing, the

enthalpy of pure “a” before mixing is $H_a = \frac{1}{2}ZN_a\epsilon_{aa}$. And similarly, the enthalpy of pure

“b” before mixing is $H_b = \frac{1}{2}ZN_b\epsilon_{bb}$. Hence, the enthalpy of mixing and the molar enthalpy of mixing are:

$$H_m = H - H_a - H_b = N_{ab}\left[\epsilon_{ab} - \frac{1}{2}(\epsilon_{aa} + \epsilon_{bb})\right] = Nx(1-x)\Omega \text{ and } h_m = \frac{H_m}{N} = x(1-x)\Omega$$

where the interaction parameter Ω is equal to $Z\left[\epsilon_{ab} - \frac{1}{2}(\epsilon_{aa} + \epsilon_{bb})\right]$. The interaction parameter is proportional to the difference in nearest-neighbor binding energy between like and unlike components. But, atoms rarely interact only with their nearest neighbors, so this simple interpretation of Ω can be at best qualitative. Ω is a useful semi-empirical measure of the chemical “dissimilarity” between two components of an alloy.

An important parameter in the regular solution model is the interaction parameter, Ω . The delta lattice parameter (DLP) model calculates Ω for III-V materials. It is based on the assumptions that the bonding energy in semiconductors is linearly related to the bandgap and that the average bandgap varies approximately as $a_0^{-2.5}$ (with a_0 the lattice parameter). It estimates the interaction parameter as:

$$\Omega \approx 4.375 \text{ K} \frac{\Delta^2}{(\bar{a})^{4.5}} \quad [41]$$

where K is a constant, $\Delta = a_a - a_b$ is the difference between the lattice parameters of the two components, and $\bar{a} = \frac{a_a + a_b}{2}$ is the average lattice parameter of the two components. Since the errors in the calculation of the enthalpy of the components cancel the error in the calculation of the enthalpy of the alloy, the DLP model is very accurate [16]. K can be obtained from a fit to experimental data, or from a calculation using the valence-force-field (VFF) model. This VFF model assumes that the microscopic strain energy associated with the bond distortion in the alloy is equal to the enthalpy of mixing [7]. Using this model, Ω_{GaNAS} has been calculated as 1.5×10^5 J/mol [7] or 2.2×10^5 J/mol [42]; Ω_{InNAS} is 0.9×10^5 J/mol [7]. Ω_{InNAS} is smaller due to the lower bond strengths of the InAs bonds.

Despite its shortcomings, the regular solution model provides good qualitative description of many phenomena and a valuable insight in the thermodynamic properties of solutions. Its popularity rests in its convenient simplicity. During MBE growth the random distribution of components is possible due to the random arrival of species and the use of reagents with a big driving force to react. Hence, the regular solution model can be applied to give qualitative guidance about growth conditions for single-phase growth (see section 2.4.3).

2.4.2 Stability of a regular solution

For solutions with a positive enthalpy of mixing (H_m and $h_m > 0$), the regular solution model also allows determination of the stability with respect to phase segregation after growth.

The molar Gibbs free energy of a regular solution is:

$$g = h - sT = (1-x)g_a^0 + xg_b^0 + \Omega x(1-x) + RT[(1-x)\ln(1-x) + x\ln x]$$

where g_a^0 and g_b^0 are the free energies of the pure components “a” and “b”. Figure 26 shows how this Gibbs free energy varies with temperature. The free energy of the solution is made of two terms with different temperature variation: the enthalpy (h) and the product of entropy and temperature (sT). Enthalpy is the driving force for segregation while entropy acts as a randomizing force. At low temperature T the enthalpy is more important than the product of entropy and temperature. Segregation can occur because the solution can lower its energy by forming two phases. If there are two phases: α , an “a”-rich phase, and β , a “b”-rich phase, in equilibrium with each other, then the total Gibbs free energy, $G^{\text{tot}} = G^\alpha + G^\beta$ is minimized with respect to transfer of atoms from one phase to the other. In other words, the change in the total Gibbs free energy should vanish if we increase the number of “a” atoms in the α phase, N_a^α while decreasing the number of “a” atoms in the β phase, N_a^β so that the overall number of “a” atoms is constant:

$$\frac{\delta G^{\text{tot}}}{\delta N_a^\alpha} = \frac{\delta G^\alpha}{\delta N_a^\alpha} + \frac{\delta G^\beta}{\delta N_a^\alpha} = \frac{\delta G^\alpha}{\delta N_a^\alpha} - \frac{\delta G^\beta}{\delta N_a^\beta} = \mu_a^\alpha - \mu_a^\beta = 0.$$

Similarly, the change in the total Gibbs free energy should vanish if we increase the number of “b” atoms in the α phase, N_b^α while decreasing the number of “b” atoms in the β phase, N_b^β so that the overall number of “b” atoms is constant:

$$\frac{\delta G^{\text{tot}}}{\delta N_b^\alpha} = \frac{\delta G^\alpha}{\delta N_b^\alpha} + \frac{\delta G^\beta}{\delta N_b^\alpha} = \frac{\delta G^\alpha}{\delta N_b^\alpha} - \frac{\delta G^\beta}{\delta N_b^\beta} = \mu_b^\alpha - \mu_b^\beta = 0.$$

Hence, the chemical potentials of “a” must be equal in the two phases, and the chemical potentials of “b” must be equal in the two phases. As the chemical potentials (μ_a^α , μ_a^β , μ_b^α , and μ_b^β) are the intercepts of the tangent to the molar Gibbs free energy curve, the two phases must share a common tangent:

$$\left[\frac{\delta g^\alpha}{\delta x^\alpha} \right]_{x_0^\alpha} = \frac{g_{x_0^\beta}^\beta - g_{x_0^\alpha}^\alpha}{x_0^\beta - x_0^\alpha} \quad \text{and} \quad \left[\frac{\delta g^\beta}{\delta x^\beta} \right]_{x_0^\beta} = \frac{g_{x_0^\beta}^\beta - g_{x_0^\alpha}^\alpha}{x_0^\beta - x_0^\alpha}$$

at their equilibrium compositions x_0^α and x_0^β . Solving these last equations yields the compositions x_0^α and x_0^β of the two phases in equilibrium with each other at temperature T . At a sufficiently high temperature, T' , the product of entropy and temperature is

sufficiently large to offset the effect of enthalpy and the phase is stable. As the temperature is raised from T to T' , the region of segregation shrinks until it vanishes at a temperature which is called the critical temperature, T_c .

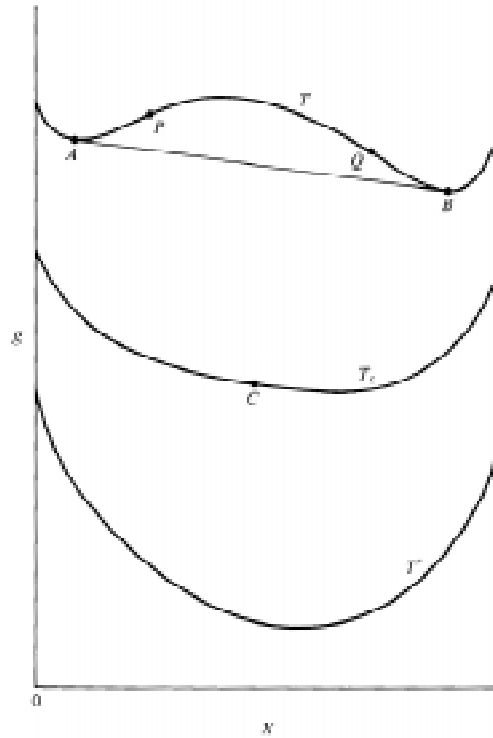


Figure 26: Typical temperature dependence of the molar free energy of a regular solution [20].

However, even if the system can lower its energy by phase segregating, this does not always happen because small composition changes do not lower the energy. Figure 27 shows how to determine whether a solution is stable with respect to small fluctuations. In every homogeneous solution, the movement of atoms will result in local composition fluctuations. Through these fluctuations, the system decomposes into a mixture of “phases”. If the Gibbs free energy of the mixture is lower than that of the homogeneous solution, the latter is unstable and further decomposition may occur to lower the Gibbs free energy (see Figure 27(b)). This is the case for $\frac{\delta^2 g}{\delta x^2} < 0$. Unstable solutions sometimes exist at room temperature. They are known as “frozen” because the rates of their decomposition are limited by the low diffusion mobility of atoms at room temperature. If the free energy of the homogeneous solution is lower than that of any mixture of phases, decomposition will not occur and the solution is stable (see Figure

27(a)). This is the case for $\frac{\delta^2 g}{\delta x^2} > 0$. The inflection point at which $\frac{\delta^2 g}{\delta x^2} = 0$ separates the regions of instability and stability (with respect to small fluctuations). It is called the spinodal point.

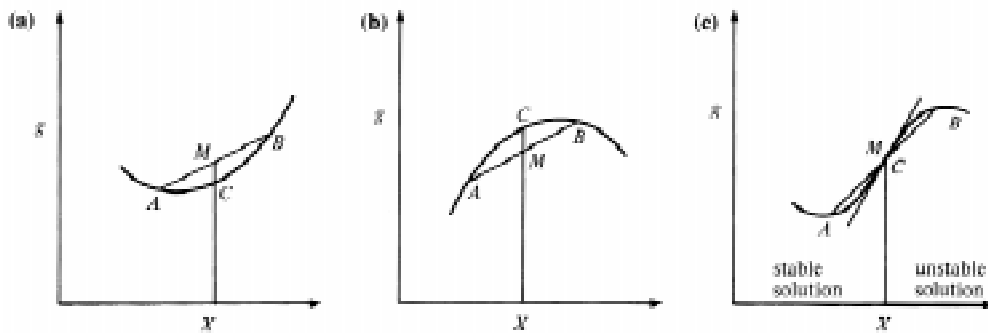


Figure 27: Criterion of stability for a homogeneous solution. (a) $\frac{\delta^2 g}{\delta x^2} > 0$: stable solution. (b)

$\frac{\delta^2 g}{\delta x^2} < 0$: unstable solution; (c) $\frac{\delta^2 g}{\delta x^2} > 0$: spinodal point [20].

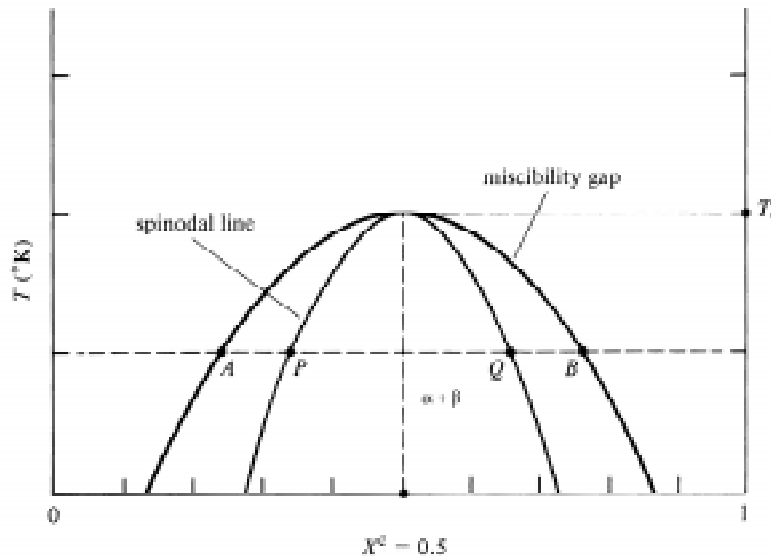


Figure 28: Example of a miscibility gap and a spinodal line in the case of a regular solution [20].

Using the equation for the molar Gibbs free energy stated above, the equation of the miscibility gap is:

$$\ln \frac{x}{1-x} = \frac{\Omega}{RT} (2x-1),$$

and the equation for the spinodal line is:

$$x(1-x) = \frac{RT}{2\Omega}$$

(see Figure 28). The critical point is determined by

$$x_c = 0.5 \text{ and } T_c = \frac{\Omega}{2R}.$$

2.4.3 Growth conditions resulting in non-phase segregated material

Despite the very low solubility of nitrogen in GaAs (0.0000001 % at 727 °C [7]), growth experiments have indicated that up to 10 mol percent GaN can be incorporated into GaAs without phase segregation [43]. Qiu et al. [43] observed that the growth conditions such as growth temperature and nitrogen-to-arsenic flux ratio determine whether phase segregation occurs during the growth of nitride-arsenides. They have built a model to explain their observations for the case of the metal organic MBE growth of GaNAs [44]. In this section, a similar model is developed for the growth of GaNAs and GaInNAs by solid source MBE using a rf plasma.

To be able to form $\text{GaN}_x\text{As}_{1-x}$, two chemical reactions must be occurring:



where the superscripts G and S refer to the gaseous and solid phases, respectively. Hence, the two following conditions for the chemical potentials must be satisfied:

$$\mu_{\text{Ga}}^G + \frac{1}{2} \mu_{\text{As}_2}^G \geq \mu_{\text{GaAs}}^S$$

$$\mu_{\text{Ga}}^G + \frac{1}{2} \mu_{\text{N}}^G \geq \mu_{\text{GaN}}^S.$$

The regular solution model is used to calculate the chemical potentials of GaAs and GaN (μ_{GaAs}^S and μ_{GaN}^S) in GaNAs. The activity coefficients in a regular solution are given by:

$$\ln \gamma_1 = \frac{\Omega}{RT} x_2^2 \text{ and } \ln \gamma_2 = \frac{\Omega}{RT} x_1^2.$$

At low pressures, the ideal gas approximation is valid. Therefore, the previous equations for the chemical potential can also be expressed as [45,21]:

$$p_{\text{Ga}}^G (p_{\text{As}_2}^G)^{1/2} \geq K_1 (1-x) \exp(\Omega x^2/RT)$$

or

$$p_{\text{Ga}}^{\text{G}} (p_{\text{As}_2}^{\text{G}})^{1/2} \geq (1-x) \exp(27.01 - 5.476 \times 10^4/T) \exp(2.2 \times 10^4 * x^2/T)$$

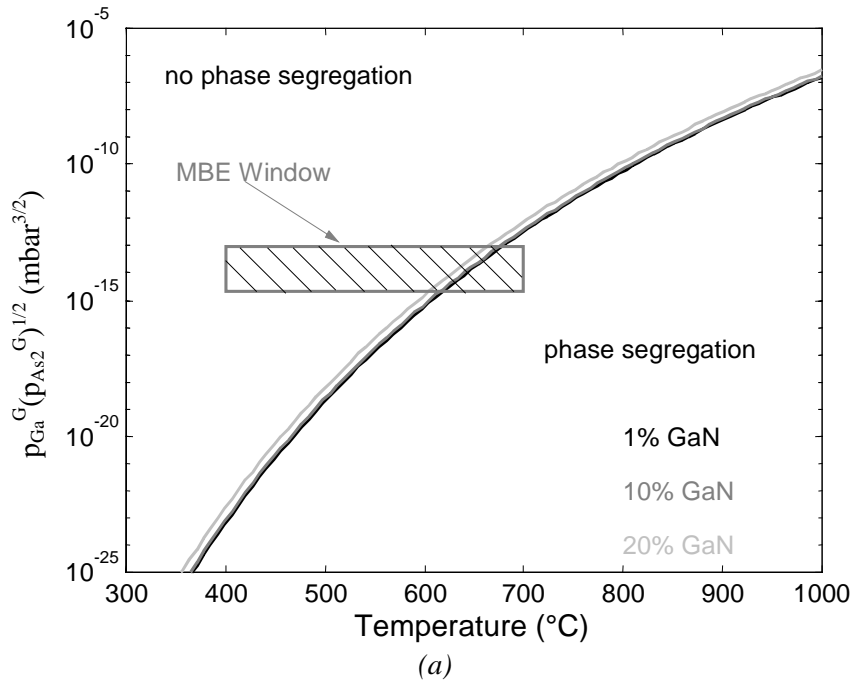
and

$$p_{\text{Ga}}^{\text{G}} p_{\text{N}}^{\text{G}} \geq K_2 x \exp(\Omega (1-x)^2 / RT)$$

or

$$p_{\text{Ga}}^{\text{G}} p_{\text{N}}^{\text{G}} \geq x \exp(35.22 - 1.031 \times 10^5/T) \exp(2.2 \times 10^4 * (1-x)^2/T);$$

where p_{Ga}^{G} , $p_{\text{As}_2}^{\text{G}}$, and p_{N}^{G} are the partial pressures in the gas phase of gallium, As₂, and atomic nitrogen, respectively. K_1 and K_2 are the equilibrium constants of the two reactions, and T is the growth temperature. Figure 29 plots these inequalities as function of temperature for different compositions. The shaded boxes indicate the MBE accessible growth conditions. Figure 29(a) refers to the reaction of gallium and arsenic to form GaAs in a solid solution GaN_xAs_{1-x}. Figure 29(b) refers to the reaction of gallium and atomic nitrogen to form GaN in a solid solution GaN_xAs_{1-x}. The two conditions are independent of each other and both must be satisfied in order to form single phase GaN_xAs_{1-x}. As atomic nitrogen is very reactive, the supplied gallium and nitrogen form a GaN bond in a solid solution GaN_xAs_{1-x} for all the possible growth conditions. The GaAs reaction dictates that single phase GaN_xAs_{1-x} can only be formed at sufficiently high As₂ pressures and sufficiently low temperatures.



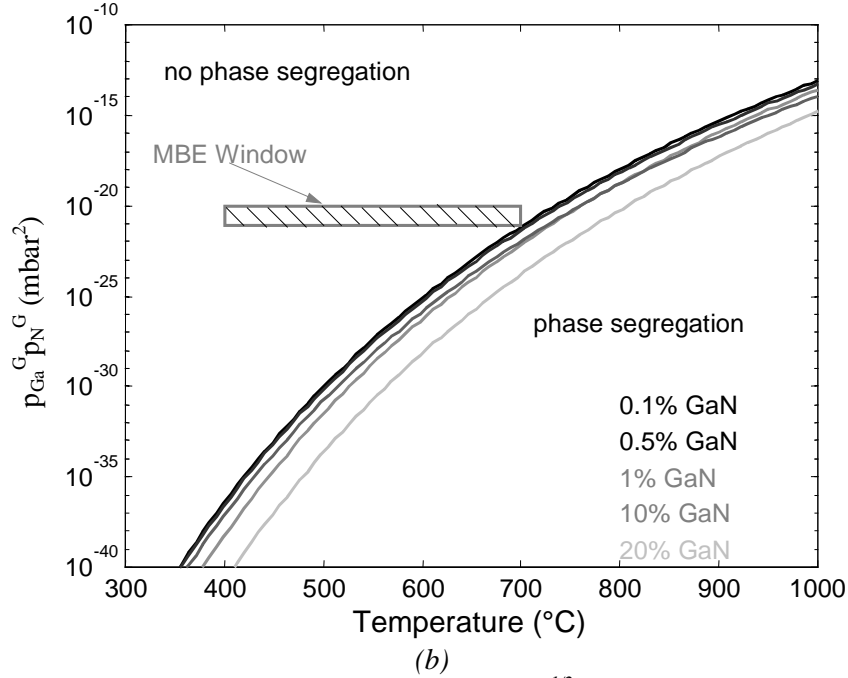


Figure 29: (a) The product of equivalent pressures of $(As_2)^{1/2}$ and Ga for which the GaAs reaction occurs in GaNAs, and (b) the product of the equivalent pressures of Ga and atomic N for which the GaN reaction occurs in GaNAs. The shaded box indicates the possible growth conditions.

Figure 30(a) shows the above calculations for $GaN_{0.05}As_{0.95}$. One can avoid precipitation and formation of N_2 by growing the nitride-arsenides at low temperatures. Figure 30(b) shows experimental data for a 400 Å $GaN_{0.05}As_{0.95}$ film grown at two different temperatures with the same plasma power, nitrogen flow, gallium flux, and As_2 flux. The X-ray $2\theta/\omega$ scans indicate that the film grown at high temperature contains a second phase and less nitrogen in the film (because of N_2 formation).

The above model can be extended to the formation of single phase GaInNAs. To be able to form $Ga_yIn_{1-y}N_xAs_{1-x}$, four chemical reactions must be occurring:



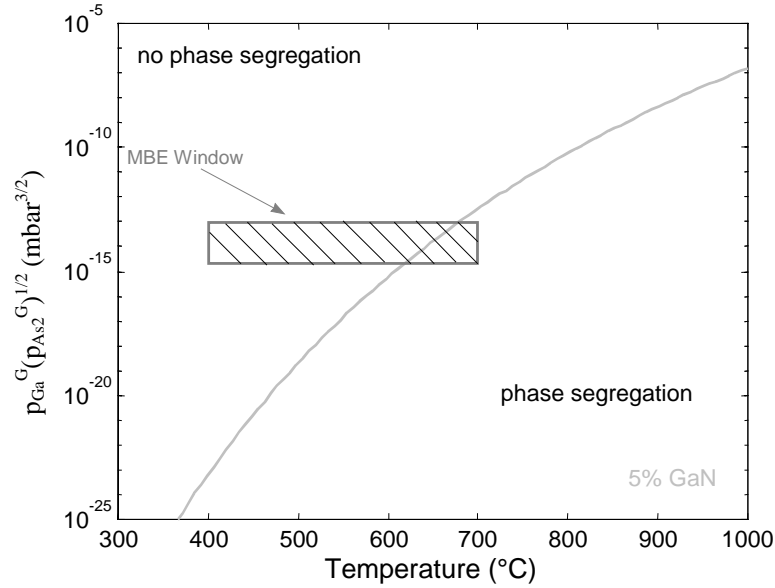
Hence, the four following conditions for the chemical potentials must be satisfied:

$$\mu_{Ga}^G + \frac{1}{2}\mu_{As_2}^G \geq \mu_{GaAs}^S$$

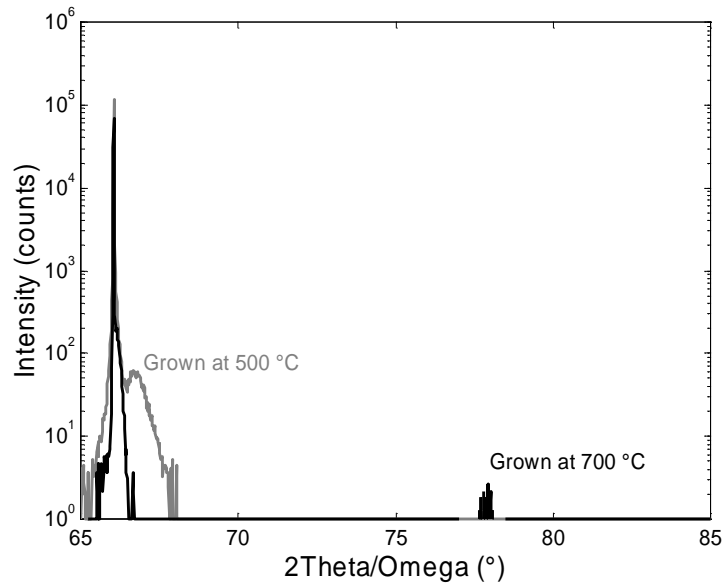
$$\mu_{Ga}^G + \frac{1}{2}\mu_N^G \geq \mu_{GaN}^S$$

$$\mu_{\text{In}}^{\text{G}} + \frac{1}{2}\mu_{\text{As}_2}^{\text{G}} \geq \mu_{\text{InAs}}^{\text{S}}$$

$$\mu_{\text{In}}^{\text{G}} + \frac{1}{2}\mu_{\text{N}}^{\text{G}} \geq \mu_{\text{InN}}^{\text{S}}$$



(a)



(b)

Figure 30: (a) The product of equivalent pressures of $(\text{As}_2)^{1/2}$ and Ga for which the GaAs reaction occurs in $\text{GaN}_{0.05}\text{As}_{0.95}$ (b) HRXRD 2Theta/Omega curve from a 400 Å $\text{GaN}_{0.05}\text{As}_{0.95}$ film grown at 500°C and a film grown under same group III and group V fluxes at 700°C.

To calculate these inequalities for the chemical potentials, an expression for the activity coefficients is needed. For the case of quaternary alloys, the activities predicted by the regular solution model are [46]:

$$\ln a_{\text{GaN}} = \ln(yx) + \Omega_{\text{InGa}}(1-y)^2/RT + \Omega_{\text{NAs}}(1-x)^2/RT - \Omega_c(1-y)(1-x)/RT$$

$$\ln a_{\text{GaAs}} = \ln(y(1-x)) + \Omega_{\text{InGa}}(1-y)^2/RT + \Omega_{\text{NAs}}x^2/RT + \Omega_c(1-y)x/RT$$

$$\ln a_{\text{InN}} = \ln((1-y)x) + \Omega_{\text{InGa}}y^2/RT + \Omega_{\text{NAs}}(1-x)^2/RT + \Omega_c y(1-x)/RT$$

$$\ln a_{\text{InAs}} = \ln((1-y)(1-x)) + \Omega_{\text{InGa}}y^2/RT + \Omega_{\text{NAs}}x^2/RT - \Omega_c yx/RT$$

with Ω_c a combination of the tetrahedral interchange energies: $\Omega_c = \Omega_{\text{GaN}} + \Omega_{\text{InAs}} - \Omega_{\text{InN}} - \Omega_{\text{GaAs}}$, and Ω_{GaIn} and Ω_{NAs} the dodecahedral interchange energies (for Ga-In and N-As interactions). Ω_c can be calculated from [46]:

$$\Omega_c = \Delta H_F^{\text{GaAs}} + \Delta H_F^{\text{InN}} - \Delta H_F^{\text{GaN}} - \Delta H_F^{\text{InAs}} - T(\Delta S_F^{\text{GaAs}} + \Delta S_F^{\text{InN}} - \Delta S_F^{\text{GaN}} - \Delta S_F^{\text{InAs}}) + \frac{1}{2}(\Omega_{\text{GaN}}^1 + \Omega_{\text{InAs}}^1 - \Omega_{\text{InN}}^1 - \Omega_{\text{GaAs}}^1)$$

with ΔH_F and ΔS_F the enthalpy and entropy of fusion of the components, and Ω^1 is the liquid interaction parameter of the components. Ω_{GaIn} and Ω_{NAs} can be approximated by [47]:

$$\Omega_{\text{GaIn}} = x\Omega_{\text{GaN-InN}} + (1-x)\Omega_{\text{GaAs-InAs}}$$

$$\Omega_{\text{NAs}} = y\Omega_{\text{GaN-GaAs}} + (1-y)\Omega_{\text{InN-InAs}}$$

Substituting the expressions for the activity coefficients into the previous equations for the chemical potential gives [45,21,48,49,50]:

$$p_{\text{Ga}}^G (p_{\text{As}_2}^G)^{1/2} \geq K_1(1-x)y$$

$$\exp((x\Omega_{\text{GaN-InN}} + (1-x)\Omega_{\text{GaAs-InAs}})(1-y)^2/RT + (y\Omega_{\text{GaN-GaAs}} + (1-y)\Omega_{\text{InN-InAs}})x^2/RT + (\Delta H_F^{\text{GaAs}} + \Delta H_F^{\text{InN}} - \Delta H_F^{\text{GaN}} - \Delta H_F^{\text{InAs}} - T(\Delta S_F^{\text{GaAs}} + \Delta S_F^{\text{InN}} - \Delta S_F^{\text{GaN}} - \Delta S_F^{\text{InAs}}) + \frac{1}{2}(\Omega_{\text{GaN}}^1 + \Omega_{\text{InAs}}^1 - \Omega_{\text{InN}}^1 - \Omega_{\text{GaAs}}^1))(1-y)x/RT)$$

or

$$p_{\text{Ga}}^G (p_{\text{As}_2}^G)^{1/2} \geq (1-x)y \exp(27.01-5.476 \times 10^4/T) \exp((3 \times 10^3 Kx + 1.5 \times 10^3 K(1-x))(1-y)^2/T + (2.2 \times 10^4 Ky + 1.1 \times 10^4 K(1-y))x^2/T + (8 \times 10^3 K - 1.9T)x(1-y)/T),$$

$$p_{\text{Ga}}^{\text{G}} p_{\text{N}}^{\text{G}} \geq K_2 xy$$

$$\begin{aligned} & \exp((x\Omega_{\text{GaN-InN}} + (1-x)\Omega_{\text{GaAs-InAs}})(1-y)^2/RT + (y\Omega_{\text{GaAs-GaN}} + (1-y)\Omega_{\text{InAs-InN}})(1-x)^2/RT - \\ & (\Delta H_{\text{F}}^{\text{GaAs}} + \Delta H_{\text{F}}^{\text{InN}} - \Delta H_{\text{F}}^{\text{GaN}} - \Delta H_{\text{F}}^{\text{InAs}} - T(\Delta S_{\text{F}}^{\text{GaAs}} + \Delta S_{\text{F}}^{\text{InN}} - \Delta S_{\text{F}}^{\text{GaN}} - \Delta S_{\text{F}}^{\text{InAs}}) + \\ & \frac{1}{2}(\Omega_{\text{GaN}}^1 + \Omega_{\text{InAs}}^1 - \Omega_{\text{InN}}^1 - \Omega_{\text{GaAs}}^1))(1-y)(1-x)/RT) \end{aligned}$$

or

$$\begin{aligned} p_{\text{Ga}}^{\text{G}} p_{\text{N}}^{\text{G}} \geq & xy \exp(35.22-1.031 \times 10^5/T) \exp((3 \times 10^3 \text{K}x + 1.5 \times 10^3 \text{K}(1-x))(1-y)^2/T + \\ & (2.2 \times 10^4 \text{K}y + 1.1 \times 10^4 \text{K}(1-y))(1-x)^2/T + (8 \times 10^3 \text{K} - 1.9T))(1-x)(1-y)/T), \end{aligned}$$

$$p_{\text{In}}^{\text{G}} (p_{\text{As}_2}^{\text{G}})^{1/2} \geq K_3 (1-x)(1-y)$$

$$\begin{aligned} & \exp((x\Omega_{\text{GaN-InN}} + (1-x)\Omega_{\text{GaAs-InAs}})y^2/RT + (y\Omega_{\text{GaN-GaAs}} + (1-y)\Omega_{\text{InN-InAs}})x^2/RT - \\ & (\Delta H_{\text{F}}^{\text{GaAs}} + \Delta H_{\text{F}}^{\text{InN}} - \Delta H_{\text{F}}^{\text{GaN}} - \Delta H_{\text{F}}^{\text{InAs}} - T(\Delta S_{\text{F}}^{\text{GaAs}} + \Delta S_{\text{F}}^{\text{InN}} - \Delta S_{\text{F}}^{\text{GaN}} - \Delta S_{\text{F}}^{\text{InAs}}) + \\ & \frac{1}{2}(\Omega_{\text{GaN}}^1 + \Omega_{\text{InAs}}^1 - \Omega_{\text{InN}}^1 - \Omega_{\text{GaAs}}^1))xy/RT) \end{aligned}$$

or

$$\begin{aligned} p_{\text{In}}^{\text{G}} (p_{\text{As}_2}^{\text{G}})^{1/2} \geq & (1-x)(1-y) \exp(9.66-5.004 \times 10^4/T) \exp((3 \times 10^3 \text{K}x + 1.5 \times 10^3 \text{K}(1-x))y^2/T + \\ & (2.2 \times 10^4 \text{K}y + 1.1 \times 10^4 \text{K}(1-y))x^2/T + (8 \times 10^3 \text{K} - 1.9T))xy/T), \end{aligned}$$

and

$$p_{\text{In}}^{\text{G}} p_{\text{N}}^{\text{G}} \geq K_4 x(1-y)$$

$$\begin{aligned} & \exp((x\Omega_{\text{GaN-InN}} + (1-x)\Omega_{\text{GaAs-InAs}})y^2/RT + (y\Omega_{\text{GaN-GaAs}} + (1-y)\Omega_{\text{InN-InAs}})(1-x)^2/RT + \\ & (\Delta H_{\text{F}}^{\text{GaAs}} + \Delta H_{\text{F}}^{\text{InN}} - \Delta H_{\text{F}}^{\text{GaN}} - \Delta H_{\text{F}}^{\text{InAs}} - T(\Delta S_{\text{F}}^{\text{GaAs}} + \Delta S_{\text{F}}^{\text{InN}} - \Delta S_{\text{F}}^{\text{GaN}} - \Delta S_{\text{F}}^{\text{InAs}}) + \\ & \frac{1}{2}(\Omega_{\text{GaN}}^1 + \Omega_{\text{InAs}}^1 - \Omega_{\text{InN}}^1 - \Omega_{\text{GaAs}}^1))(1-x)y/RT) \end{aligned}$$

or

$$\begin{aligned} p_{\text{Ga}}^{\text{G}} p_{\text{N}}^{\text{G}} \geq & xy \exp(34.12-1.071 \times 10^5/T) \exp((3 \times 10^3 \text{K}x + 1.5 \times 10^3 \text{K}(1-x))y^2/T + \\ & (2.2 \times 10^4 \text{K}y + 1.1 \times 10^4 \text{K}(1-y))(1-x)^2/T + (8 \times 10^3 \text{K} - 1.9T))(1-x)y/T); \end{aligned}$$

where p_{In}^{G} is the partial pressure in the gas phase of indium, and K_3 and K_4 are the equilibrium constants of the two indium reactions.

The results of these calculations for $\text{Ga}_y\text{In}_{1-y}\text{N}_x\text{As}_{1-x}$ with $x = 0.02$ and $y = 1$ or $y = 0.7$ are shown in Figure 31. The GaAs reaction still determines whether single phase

material can be formed. The nitride reactions are not limiting because very reactive atomic nitrogen is supplied. Moreover, the InAs reaction occurs more easily than the GaAs reaction because the InN-InAs interaction parameter is smaller than the GaN-GaAs interaction parameter. Again, phase segregation can be avoided by growing at sufficiently low temperatures and sufficiently high arsenic overpressures. The addition of indium does not significantly change the necessary growth conditions to drive the GaAs reaction forward; the main parameter determining phase segregation is the large GaN-GaAs interaction parameter.

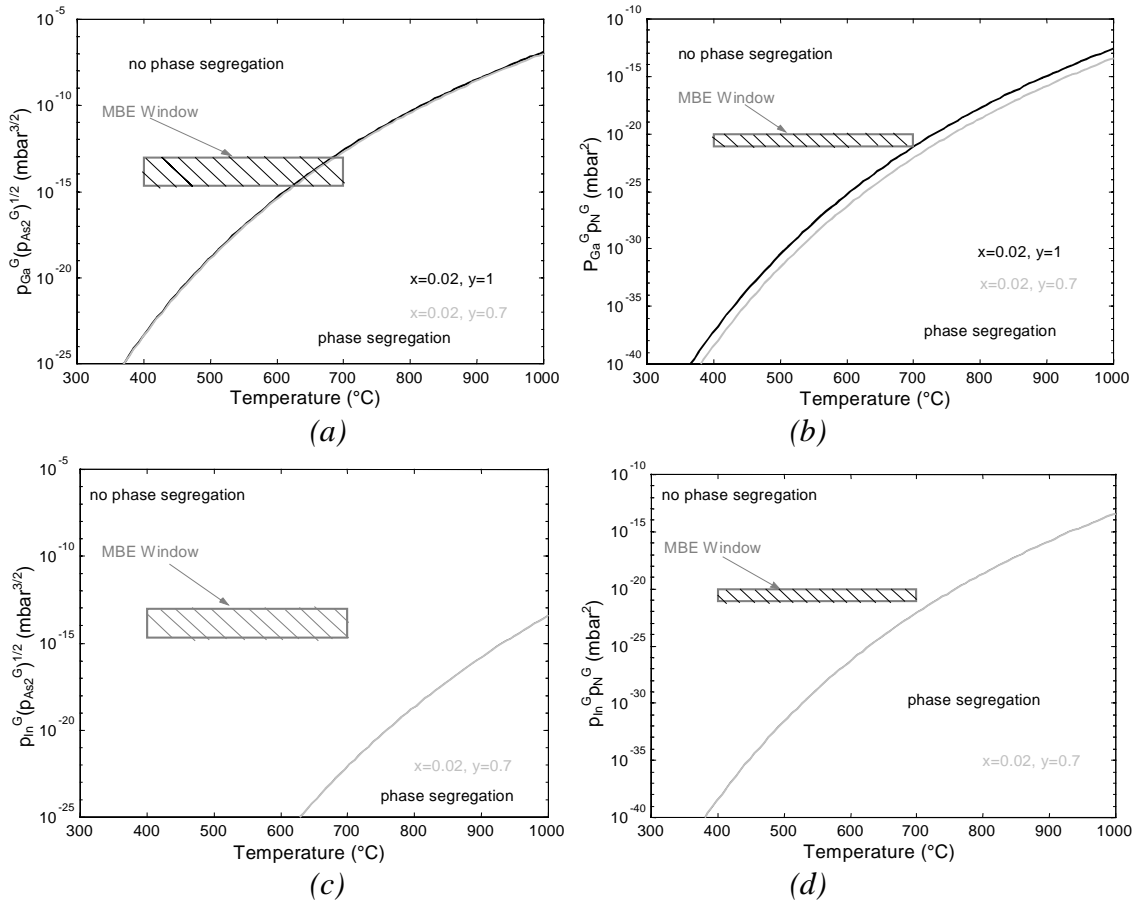


Figure 31: (a) The product of equivalent pressures of $(As_2)^{1/2}$ and Ga for which the GaAs reaction occurs in $Ga_yIn_{1-y}N_xAs_{1-x}$ (b) the product of the equivalent pressures of Ga and atomic N for which the GaN reaction occurs in $Ga_yIn_{1-y}N_xAs_{1-x}$ (c) the product of equivalent pressures of $(As_2)^{1/2}$ and In for which the InAs reaction occurs in $Ga_yIn_{1-y}N_xAs_{1-x}$ (d) the product of the equivalent pressures of In and atomic N for which the InN reaction occurs in $Ga_yIn_{1-y}N_xAs_{1-x}$. The possible growth conditions are indicated by the shaded box.

The previous model describes the necessary growth conditions to form single-phase material with relatively high nitrogen concentration. A model to explain how the relatively high nitrogen concentrations are incorporated in GaAs despite the low

solubility was developed by Zhang et al. [51]. As described before (see Figure 12), the (001) surface of GaAs is covered with adsorbed As_2 dimers during the growth of GaAs. The surface dimer bonds cause local strain variations at the surface (see Figure 32). The anion site directly under the dimer (labeled α) is under compression, while the anion site with no dimers above it (labeled β) is under tension. Of course, these strain variations caused by surface dimers diminish as one moves deeper into the film. Hence, the overall strain energy reduces and the solubility rises if small solute atoms (e. g. N) incorporate at the α site and larger (solvent) atoms at the β site close to the surface. The valence force field theory [7] can be used to calculate the modified substitution energy; it predicts a surface solubility of $2 \times 10^{19} \text{ cm}^{-3}$ (compared to $1 \times 10^{14} \text{ cm}^{-3}$ for the bulk). When the growth conditions permit, the high surface nitrogen concentration may be frozen in as the crystal grows.

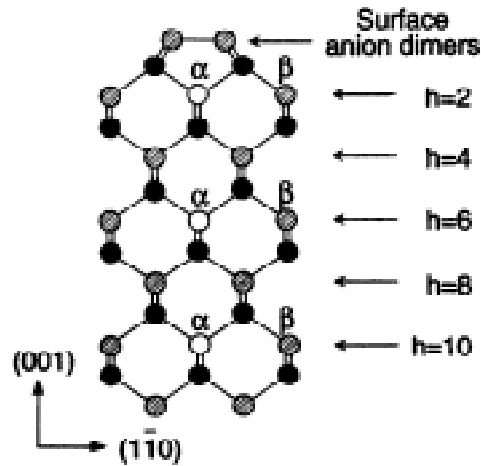


Figure 32: Atomic structure of the dimerized (001) surface. The solid dots represent cations, while the open and hatched dots represent anions on the α and β sites respectively [57].

The model from Zhang et al. also has other implications. First of all, it predicts a lower substitution energy for the nitrogen atoms at the surface. This energy difference will act as a driving force for nitrogen segregation to the top of the growing film resulting in a higher nitrogen concentration near the surface. In fact, this segregation has been observed by Bandic et al [52]. Furthermore, a difference in cation sizes can also reduce some of the strain energy when the small cation incorporates under the α site and the big cation incorporates under the β site. Therefore, the enhanced nitrogen solubility is expected to be less in InGaAs alloys. Finally, as some of the surface strain can be

released by incorporating interstitials above the β sites, this model predicts a higher concentration of interstitials that can also be frozen in (see section 3.2.4.4).

The two models described above have one important aspect in common: they predict that a higher nitrogen concentration is incorporated during the growth and that this higher nitrogen concentration is frozen in due to low diffusion mobility of atoms. Hence, all the nitride-arsenide films with nitrogen concentrations above 0.0000001 % are meta-stable or unstable with respect to phase segregation.

2.4.4 Spinodal decomposition calculations

In the previous section, we showed that it is possible to grow single phase nitride-arsenides with higher a nitrogen concentration than the equilibrium solid solubility. Because nitride-arsenide alloys have to be annealed in order to remove non-radiative recombination centers (see section 3.2.3), it is important to determine whether these alloys are stable under annealing. Hence, we need to determine the spinodal decomposition region. However, in the case of a strained film on a strained substrate and decomposition into phases with different lattice parameters, additional strain energy terms have to be included into the calculation.

The first strain energy term comes about because the two phases into which nitride-arsenides decompose have a different lattice parameter. This coherency stress stabilizes the alloy with respect to composition fluctuations and hence reduces the critical temperature above which the material system is stable. Cahn [53] showed the stability criterion reduces to:

$$\frac{\delta^2 g}{\delta x^2} + 2\eta^2 Y(100) = 0$$

where η is a function of the volume change caused by phase segregation, and $Y(100)$ is function of the elastic constants in the material:

$$V(c) = V_0[1 + 3\eta(c-c_0)] \text{ or } \eta = \frac{\Delta V}{3\Delta c \bar{V}}$$

$$Y(100) = \frac{(C_{11} + 2C_{12})(C_{11} - C_{12})}{C_{11}}$$

with $V(c)$ the stress-free molar volume at concentration c , and V_0 the molar volume at the not phase segregated concentration c_0 .

The strain energy with respect to the substrate results in an increase of the Gibbs free energy g^{str} that can be expressed as:

$$g^{\text{str}} = v_m \frac{(C_{11} + 2C_{12})(C_{11} - C_{12})}{C_{11}} \epsilon^2$$

with v_m the molar volume, and ϵ the strain in the epitaxial layer [54]. This energy due to a lattice parameter mismatch between epi-layer and substrate tends to stabilize the solid composition that produces an exact lattice parameter match.

Schlenker et al. [55] have considered these additional terms when calculating the spinodal decomposition region and showed that due to the strain effect $\text{Ga}_y\text{In}_{1-y}\text{N}_x\text{As}_{1-x}$ alloys with $y \geq 0.6$ and $x \leq 0.4$ are stable with respect to spinodal decomposition (see Figure 33(b)).

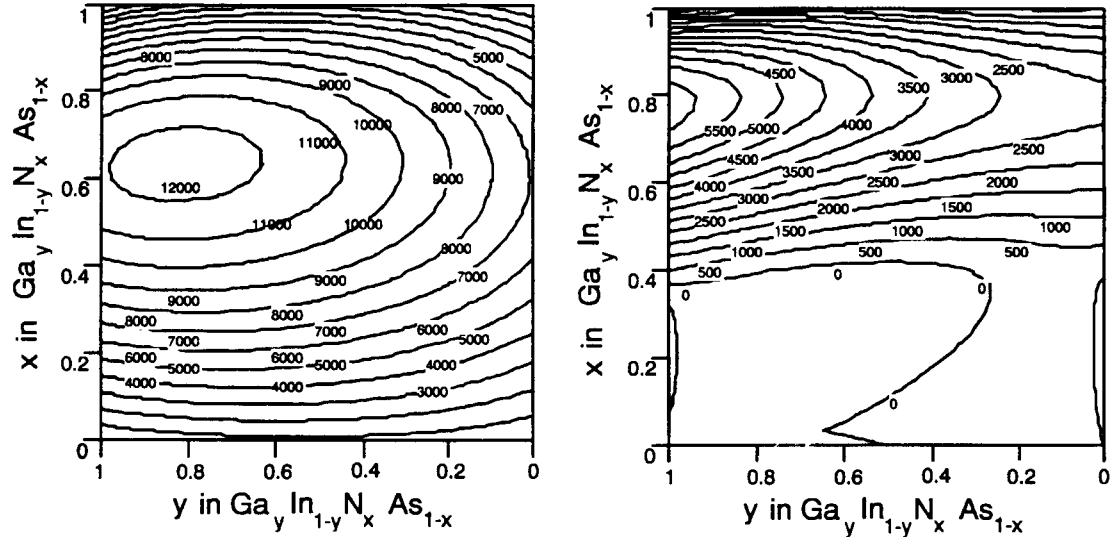


Figure 33: A contour plot of the miscibility gap in $\text{Ga}_y\text{In}_{1-y}\text{N}_x\text{As}_{1-x}$ on a GaAs substrate (a) neglecting strain effects and (b) including strain effects [55]. The numbers in the figure show the critical temperatures above which the material is meta-stable

2.4.5 Ordering

One final issue related to thermodynamic aspects of the growth is ordering. Ordering has been observed in several III-V solid solutions [16]. If the positive interaction parameter is due to strain, the atoms tend to be arranged with a larger than random number of unlike nearest neighbor pairs. This leads to an increase in the number of bonds between dissimilar atoms, i.e. ordering. Hence, the size difference drives both

ordering and phase segregation [56]. The VFF model is usually used to calculate the microscopic strain and the associated bond bending and bond stretching [40].

Ordering might be taking place during the growth of nitride-arsenides.

2.5 MBE versus MOCVD growth of nitride-arsenides

MOCVD proceeds at conditions much closer to thermodynamic equilibrium than MBE. This seems to affect its capabilities to grow nitride-arsenides.

In MOCVD growth, the nitrogen incorporation is low and strongly temperature dependent at the typical growth temperature due to nitrogen desorption from the surface [57]. Because this desorption is reduced at lower growth temperatures, one of the breakthroughs in MOCVD growth of nitride-arsenides has been the development of gas sources having a low decomposition temperature: dimethylhydrazine (DMHy) to supply nitrogen and tertiarybutylarsine (TBAs) to supply arsenic.

Obtaining a low concentration of background impurities in the deposited material is a challenge when growing the nitride-arsenides by MOCVD. The purity of the DMHy and the TBAs is lower than other precursors, not only because they are less common but also because they are harder to purify due to their low decomposition temperature. Moreover, DMHy is thought to decompose into $(\text{CH}_3)_2\text{N}$ and NH_2 . These two species are adsorbed onto the growing surface and result in hydrogen as well as carbon incorporation due to the strong N-H and N-C bonds [58].

Controlling the nitrogen composition was found to be difficult for MOCVD growth of nitride-arsenides. The nitrogen concentration in the film is dependent on the growth temperature, the TBAs partial pressure, the V/III ratio, the growth rate, and the indium concentration of the epitaxial layer [59]. The nitrogen uptake exponentially drops with growth temperature due to nitrogen desorption. Increasing the TBAs partial pressure reduces the nitrogen concentration as arsenic competes with nitrogen for the group V sites [60]. Unfortunately, this implies that nitride-arsenides have to be grown at a lower TBAs pressure than the one needed to minimize crystal defects during the growth. Increasing the V/III ratio decreases the nitrogen incorporation. Reducing the growth rate reduces the nitrogen incorporation due to the higher desorption of nitrogen

from the surface. With increasing indium concentration of the GaInNAs, the nitrogen content reduces significantly.

Compared to these challenges, the optimization of the operation of the rf plasma during plasma assisted MBE growth of nitride-arsenides seems far easier.

2.6 Conclusion

Nitride-arsenide materials have been grown by molecular beam epitaxy (MBE) using a radio frequency (rf) nitrogen plasma source. The nitrogen concentration has been controlled by changing the group III growth rate with the plasma power and nitrogen flow fixed to achieve optimum plasma source operation. The nitrogen sticking coefficient is unity for the low growth temperatures used. Hence, the nitrogen concentration is inversely proportional to the group III growth rate. Despite the large tendency for phase segregation, single-phase nitride-arsenide films are formed when using low growth temperatures. The regular solution model and surface reconstruction enhanced solubility of nitrogen are used to predict these observations. It is expected that these alloys are stable with respect to phase segregation after their formation due to strain effects. MBE seems to be more suitable than MOCVD to grow nitride-arsenides.

The optical properties and crystal quality of the grown nitride-arsenides will be studied in the next chapter.

Chapter 3: Optical Properties of Nitride-Arsenides

The previous chapter described the MBE growth of nitride-arsenides.

Before using these materials in opto-electronic devices, their optical properties must be determined. Absorption measurements are performed to determine the GaNAs bandgap as a function of the nitrogen composition. This relationship is used to derive the indium and nitrogen concentration of GaInNAs alloys yielding emission at 1.3 μm . Quantum wells (QWs) of these alloys have been analyzed by photoluminescence. We have evaluated processes to improve the photoluminescence efficiency.

The next chapter describes how understanding these processes allows us to modify the quantum well design to achieve 1.3 μm emission.

3.1 Dependence of GaNAs bandgap on composition

3.1.1 Theoretical background for absorption measurements

A typical absorption measurement setup is shown in Figure 34. For wavelengths in the visible and near IR, a tungsten lamp is used as the light source. A monochromator is used to select a narrow band of wavelengths from the source. The sample is placed at the exit slit of the monochromator so that the wavelength of the light incident on the sample is set by the monochromator and the absorption is measured at that particular wavelength. The detector must be chosen for the proper spectral range. Lenses are used to focus the light on the entrance slit of the monochromator, on the sample, and on the detector.

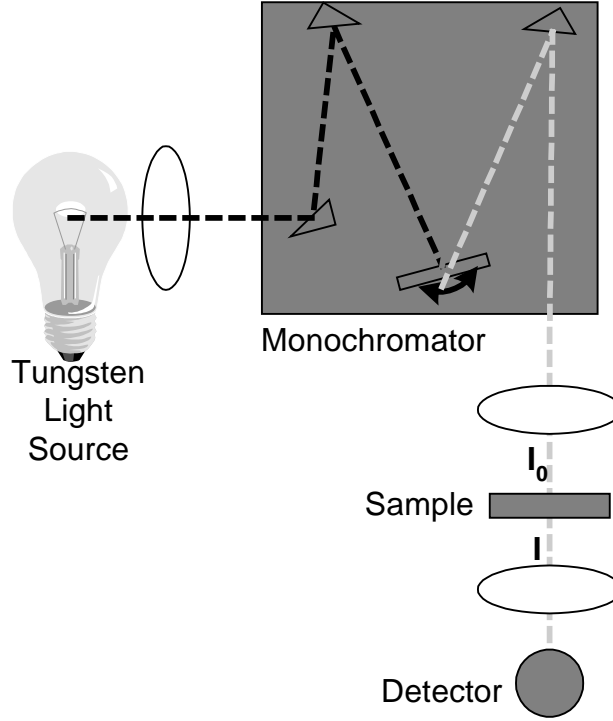


Figure 34: Diagram of experimental setup for absorption measurement [61].

The absorption coefficient, α , is the relative rate of decrease in light intensity, I , along its propagation path:

$$\alpha = -\frac{1}{I} \frac{dI}{dx}.$$

Taking into account multiple internal reflections, the transmitted intensity I_t of a sample with thickness t and reflectivity R is given by:

$$I_t = \frac{I_0(1-R)^2 e^{-\alpha t}}{1-R^2 e^{-2\alpha t}}$$

with I_0 incident intensity at a particular wavelength [61]. For a GaAs sample, the reflectivity is 0.3 [4]. The absorption coefficient, α , can be calculated from:

$$\alpha = \frac{1}{t} \ln \left(\frac{2 \frac{I_t}{I_0} \frac{R^2}{(1-R)^2}}{\sqrt{1 + 4 \left(\frac{I_t}{I_0} \right)^2 \frac{R^2}{(1-R)^4} - 1}} \right).$$

An expression for the absorption due to direct electron transitions from the valence band to the conduction band (see Figure 35) can be found as follows. According to the quantum mechanical perturbation theory, the transition rate for absorption between

an initial state i , with energy E_i , and a final state f , with energy E_f , in the presence of an oscillating electro-magnetic field with frequency ω is equal to [4]:

$$W_{\text{abs}} = \frac{2\pi}{\hbar} \left| \langle f | H'(\mathbf{r}, t) | i \rangle \right|^2 \delta(E_f - E_i - \hbar\omega)$$

where \hbar is the reduced Planck constant ($\hbar = 1.05459 \times 10^{-34}$ Js) and $H'(\mathbf{r}, t)$ is the time-dependent part of the Hamiltonian according to $H = H_0 + H'(\mathbf{r}, t)$ with H the complete Hamiltonian and H_0 the time-independent unperturbed part. The δ -function assures that energy is conserved during photon absorption. The transition rate is proportional to $\left| \langle f | H'(\mathbf{r}, t) | i \rangle \right|^2$ which depends on the quantum mechanical nature of the initial and final states, and the strength of the oscillating ‘‘perturbation’’, $H'(\mathbf{r}, t)$. For an electron in an electro-magnetic field $H'(\mathbf{r}, t)$ is approximated as:

$$H'(\mathbf{r}, t) \approx -\frac{e}{m_0} \mathbf{A} \cdot \mathbf{p} = -\frac{eA_0 \exp(i\mathbf{k}_{\text{op}} \cdot \mathbf{r})}{2m_0} \hat{\mathbf{e}} \cdot \mathbf{p}$$

where \mathbf{p} is the momentum operator, $-i\hbar\nabla$, and \mathbf{A} is the electro-magnetic vector potential:

$$\mathbf{A} = \hat{\mathbf{e}} \left\{ \frac{A_0}{2} \exp[i(\mathbf{k}_{\text{op}} \cdot \mathbf{r} - \omega t)] + \frac{A_0}{2} \exp[-i(\mathbf{k}_{\text{op}} \cdot \mathbf{r} - \omega t)] \right\}$$

with \mathbf{k}_{op} the wavevector of the optical field inside the material and $\hat{\mathbf{e}}$ the direction of the electric field of the linearly polarized wave. The final and initial states can be found using the Bloch theorem:

$$|i\rangle = \frac{\mathbf{u}_v(\mathbf{r}) \exp(i\mathbf{k}_v \cdot \mathbf{r})}{\sqrt{N}} \quad \text{and} \quad |f\rangle = \frac{\mathbf{u}_c(\mathbf{r}) \exp(i\mathbf{k}_c \cdot \mathbf{r})}{\sqrt{N}}$$

with \mathbf{k}_v the electron wavevector in the valence band, \mathbf{k}_c the electron wavevector in the conduction band, N the number of unit cells in the crystal, $\int_{\text{unit}} \mathbf{u}_v^*(\mathbf{r}) \mathbf{u}_v(\mathbf{r}) d^3\mathbf{r} = 1$, and

$\int_{\text{unit}} \mathbf{u}_c^*(\mathbf{r}) \mathbf{u}_c(\mathbf{r}) d^3\mathbf{r} = 1$. The resulting expression for the transition rate can be further

simplified using the two following considerations:

1. We are interested in transitions near the center of the Brillouin zone and \mathbf{k}_{op} is very small. Therefore, $\exp[i(\mathbf{k}_v - \mathbf{k}_c + \mathbf{k}_{\text{op}}) \cdot \mathbf{r}]$ is nearly constant within a unit cell.
2. Momentum is conserved or $\mathbf{k}_v - \mathbf{k}_c + \mathbf{k}_{\text{op}} = 0$.

The transition rate for absorption between an initial state i and a final state f becomes:

$$W_{\text{abs}} = \frac{2\pi}{\hbar} \frac{e^2 A_0^2}{4m_0^2} |p_{\text{cv}}|^2 \delta(E_f - E_i - \hbar\omega)$$

with $p_{\text{cv}} = \int_{\text{unit cell}} u_c^*(\mathbf{r}) \hat{\mathbf{e}} \cdot \mathbf{p} u_v(\mathbf{r}) d^3\mathbf{r}$.

To calculate the optical absorption coefficient, α , we need the total transition rate, W_{tot} , which is the sum of the transition rates between all possible initial states and all possible final states:

$$W_{\text{tot}} = \frac{2\pi}{\hbar} \frac{e^2 A_0^2}{4m_0^2} |p_{\text{cv}}|^2 \sum_{\mathbf{k}} \delta(E_f - E_i - \hbar\omega) = \frac{2\pi}{\hbar} \frac{e^2 A_0^2}{4m_0^2} |p_{\text{cv}}|^2 \int_E g_J(E_J) \delta(E_J - \hbar\omega) dE_J$$

where $g_J(E_J)$ is the joint density of states:

$$g_J(E_J) = \frac{1}{2\pi^2} \left(\frac{2\mu_{\text{eff}}}{\hbar^2} \right)^{3/2} (E_J - E_g)^{1/2}$$

E_J is defined as $E_J(\mathbf{k}) = E_c(\mathbf{k}) - E_v(\mathbf{k}) = \frac{\hbar^2 \mathbf{k}^2}{2} \left(\frac{1}{m_e} + \frac{1}{m_h} \right) + E_g = \frac{\hbar^2 \mathbf{k}^2}{2\mu_{\text{eff}}} + E_g$ with m_e the electron effective mass in the conduction band, and m_h the hole effective mass in the valence band. The total transition rate is equal to:

$$W_{\text{tot}} = \frac{1}{\hbar} \frac{e^2 A_0^2}{4m_0} E_p \frac{1}{2\pi} \left(\frac{2\mu_{\text{eff}}}{\hbar^2} \right)^{3/2} (\hbar\omega - E_g)^{1/2} \quad \text{for } \hbar\omega \geq E_g$$

with $E_p = \frac{2}{m_0} |p_{\text{cv}}|^2$ according to the $\mathbf{k} \cdot \mathbf{p}$ Kane model [4].

The absorption coefficient, α , is related to total transition rate, W_{tot} , and the photon flux, n_p , by:

$$\alpha(\hbar\omega) = \frac{W_{\text{tot}}}{n_p} = \frac{\hbar e^2}{4\pi m_0 n_r c \epsilon_0} \frac{E_p}{\hbar\omega} \left(\frac{2\mu_{\text{eff}}}{\hbar^2} \right)^{3/2} (\hbar\omega - E_g)^{1/2};$$

the photon flux is defined as the number of incident photons per unit area per second and is equal to $n_p = \frac{I}{\hbar\omega}$ with $I = \frac{n_r c \epsilon_0 \omega^2 A_0^2}{2}$ [4], n_r the refractive index, c the velocity of light, and ϵ_0 the permittivity of free space. The absorption spectrum, $\alpha(\hbar\omega)$, follows the joint density of states: it rises as $(\hbar\omega - E_g)^{1/2}$ for $\hbar\omega > E_g$ and is zero for $\hbar\omega < E_g$. The form of the optical absorption edge for these direct transitions is illustrated in Figure 35.

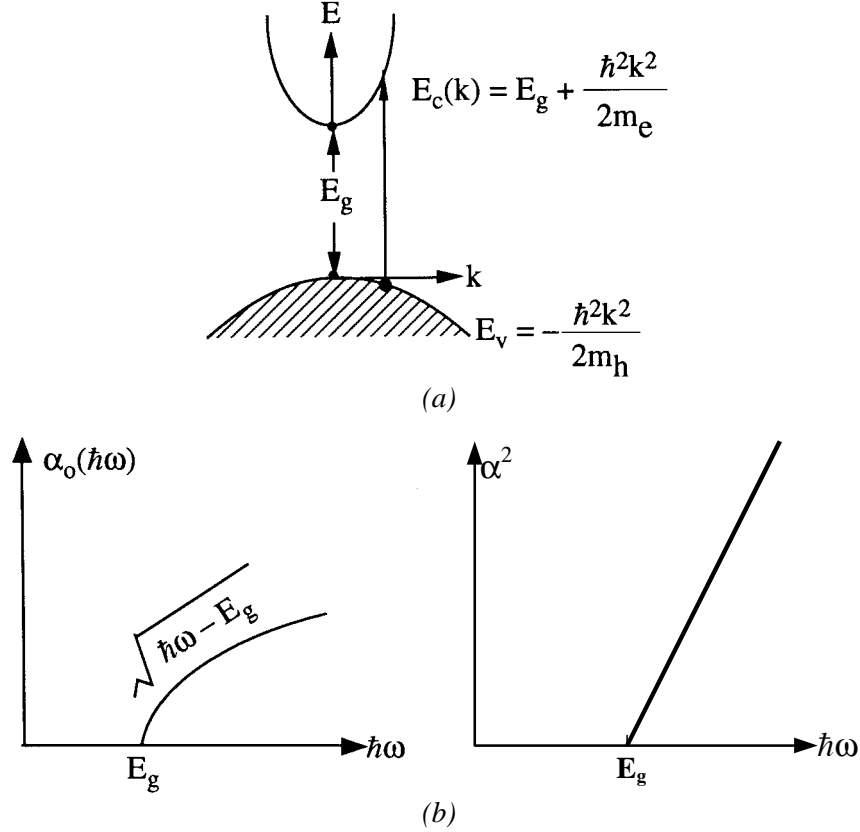


Figure 35: (a) Illustration of direct optical transitions between an electron state in the valence band to a state in the conduction band with the same momentum (b) Resulting absorption for these direct optical transitions.

The above derivation has assumed that the valence band is completely occupied and the conduction band is empty. A derivation for a partially occupied valence band and an almost empty conduction band can be found in [62]. The above model also does not include the effect of excitons. At low temperature excitons or bound electron-hole pairs cause a peak near the bandgap energy in the absorption spectrum [63].

3.1.2 Experimental determination of GaNAs bandgap versus nitrogen concentration

To determine the relationship between the bandgap energy and nitrogen concentration in GaNAs alloys, we have used absorption measurements to determine the bandgap energy and high resolution X-ray diffraction (HRXRD) measurements to determine the nitrogen concentration.

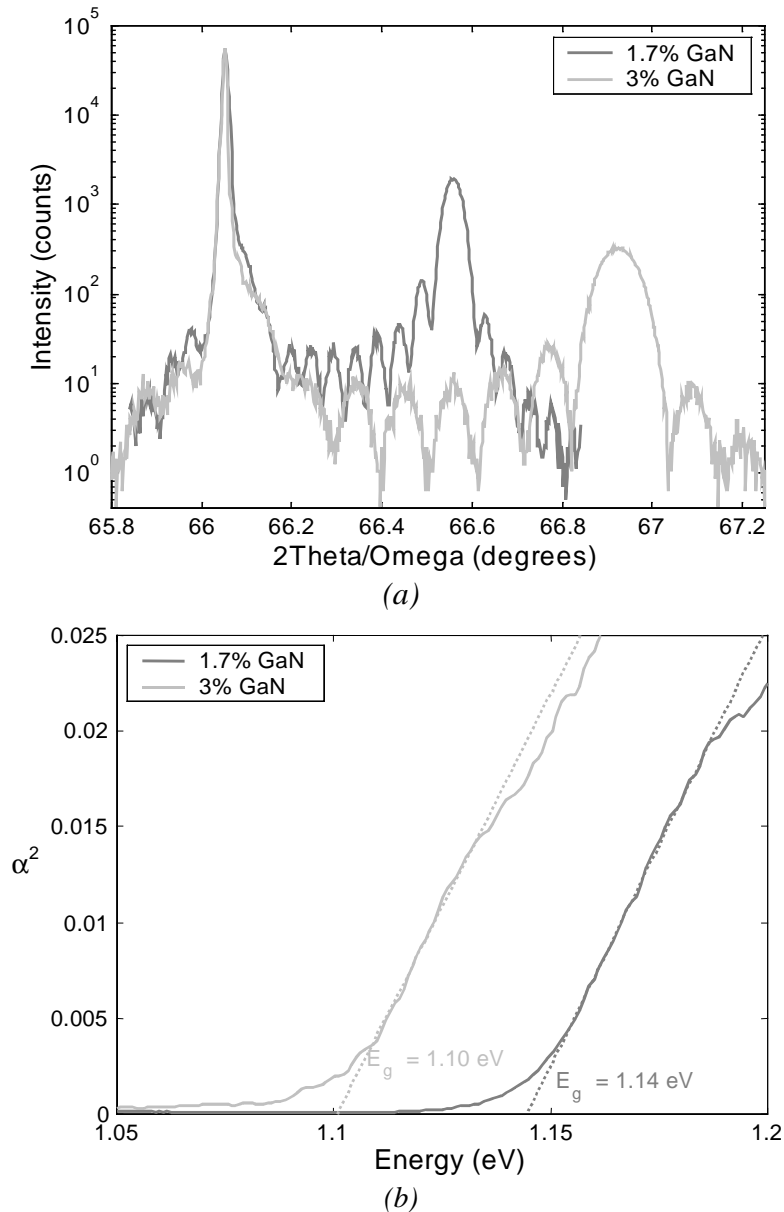


Figure 36: (a) Symmetric HRXRD scans showing GaAs and GaNAs 004 peak (b) Absorption measurement from the same sample.

The two samples used for this analysis are a 2000 Å thick $\text{GaN}_{0.017}\text{As}_{0.983}$ film on a GaAs substrate and a 1000 Å thick $\text{GaN}_{0.03}\text{As}_{0.97}$ film on a GaAs substrate. Thick films have been grown to assure that the bulk properties of the GaNAs are determined. X-ray mapping experiments have revealed that both films are not relaxed from the position of the film (224) peak with respect to the GaAs (224) peak (see section 2.3). The results from the symmetrical high resolution X-ray scan and the absorption measurement are shown in Figure 36.

The nitrogen concentration of the GaNAs films has been determined from the HRXRD measurements. From the position of the film peak one can determine the not strained lattice parameter (see section 2.3). Vegard's law is used to determine the nitrogen concentration from the lattice parameter (see section 2.3). We have obtained a concentration of 1.7 mol % GaN for the film with the low nitrogen concentration and a concentration of 3 mol % GaN for the film with the higher nitrogen concentration.

The thickness of the film has been determined from the Pendellösung oscillations in the HRXRD scan. The diffracted X-Ray intensity of a finite crystal varies as:

$$I(\mathbf{q}) = I_0 \left(\frac{r_e}{R} \right)^2 |F_c(\mathbf{q})|^2 \left[\prod_{j=1}^3 \frac{\sin^2(N_j \mathbf{q} \cdot \mathbf{a}_j / 2)}{\sin^2(\mathbf{q} \cdot \mathbf{a}_j / 2)} \right] \quad [64]$$

with \mathbf{q} the scattering vector defined as $q_B = \frac{4\pi \sin \theta_B}{\lambda}$ at the Bragg condition, r_e the radius of an electron, R the distance from detector to sample, $F_c(\mathbf{q})$ the structure factor, and N_j the number of unit cells in the crystal along the direction of the unit cell vector \mathbf{a}_j . For a film with thickness t (assumed infinite in the other two directions), the distance between the maxima in symmetric HRXRD is

$$\Delta q = \frac{2\pi}{t} = \frac{4\pi}{\lambda} \cos \theta \Delta \theta \quad \text{or} \quad t = \frac{\lambda}{2 \cos \theta \Delta \theta}.$$

We have obtained a film thickness of 2185 Å for the film with the lower nitrogen concentration and a thickness of 990 Å for the film with the higher nitrogen concentration.

These thicknesses have been used to calculate the absorption coefficient as a function of wavelength from the incident and transmitted optical intensities (see section 3.1.1). The absorption coefficient is plotted as a function of energy in Figure 36(b). The intercept of the linearly increasing part with the x-axis results in a bandgap energy of 1.14 eV for the film with the lower nitrogen concentration and 1.10 eV for the film with the higher nitrogen concentration.

The absorption and HRXRD measurements are combined to determine that the decrease in the bandgap energy is approximately 100 meV/mol % GaN. When assuming that indium and nitrogen do not interact, this trend can be used together with the dependence of the InGaAs bandgap on indium composition ($E_g = 0.36 + 0.505x +$

$0.555x^2$ in $\text{In}_{1-x}\text{Ga}_x\text{As}$ [4]) to estimate which GaInNAs alloys give rise to emission at $1.3 \mu\text{m}$. Possible alloys for bulk $1.3 \mu\text{m}$ emission are $\text{GaN}_{0.05}\text{As}_{0.95}$, $\text{In}_{0.35}\text{Ga}_{0.65}\text{As}$, $\text{Ga}_{0.8}\text{In}_{0.2}\text{N}_{0.02}\text{As}_{0.98}\dots$ (see Figure 37). Because most opto-electronic devices use these alloys in QWs, we have investigated the optical properties of QWs from these alloys using photoluminescence (PL) (see section 3.2.3).

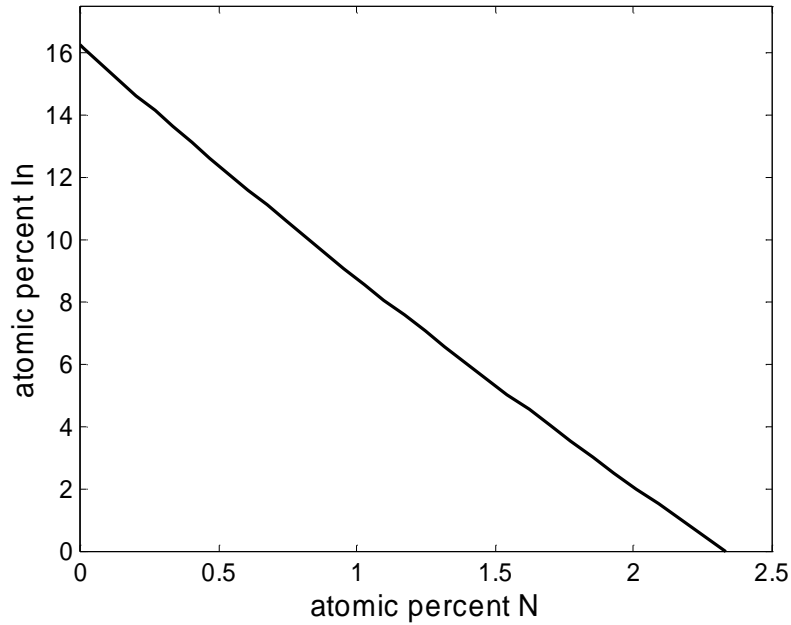


Figure 37: Indium and nitrogen concentration for GaInNAs alloys resulting in bulk $1.3 \mu\text{m}$ emission.

3.2 Photoluminescence from nitride-arsenides

3.2.1 Theoretical background for photoluminescence measurements

A PL measurement entails optical stimulation and detection of the resulting light emission. It is a very diverse qualitative technique with excellent sensitivity.

A PL measurement setup consists of a source for optical excitation, a spectrometer, and a detector suitable for the emitted light. A typical PL measurement setup is shown in Figure 38. Our setup uses an Argon laser with a wavelength of 514.5 nm and an InGaAs photodetector. The output of the Argon laser is chopped to increase the sensitivity of the apparatus by lock-in amplification.

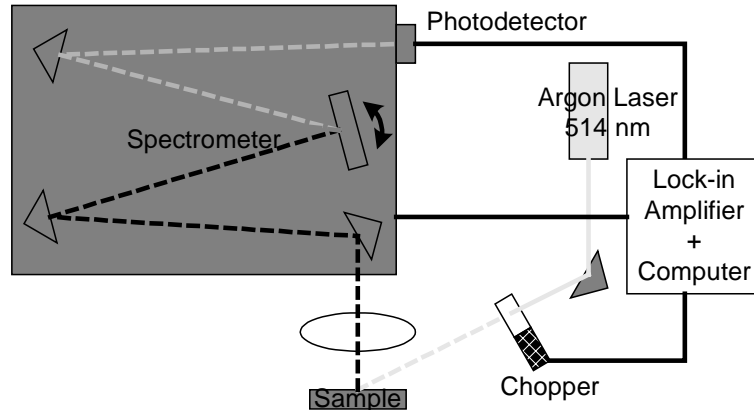


Figure 38: Experimental setup used for PL measurement.

The different processes taking place when performing a PL measurement are shown in Figure 39. First, the material gains energy by absorbing light and promoting an electron to a higher energy level. One possible excitation in a semiconductor is an electron transition from the valence band to the conduction band. The system then relaxes non-radiatively to a more stable excited state by interaction with crystalline vibration modes (or phonons). After a characteristic lifetime, τ_{tot} , in this second excited state the system will return to the ground state. The energy released during this final transition can be in the form of light. In a semiconductor photons are sometimes emitted when an electron and a hole recombine. The wavelength of the emitted light is determined by difference between the electron and the hole energy level. Besides this band-to-band emission and recombination, semiconductors can also undergo intraband transitions and transitions involving traps with levels in the bandgap. In order of decreasing energy the following structures are usually observed in a near-band-edge PL spectrum of a direct bandgap semiconductor (see Figure 40): electron hole recombination from the conduction band to the valence band (CV), free exciton recombination (X), recombination of excitons bound to neutral donors and acceptors (D^0X and A^0X), electron hole recombination from the conduction band to an acceptor level (CA), and recombination from a donor level to an acceptor level (DA). In some cases these other processes reduce the number of excited carriers available for band-to-band recombination, resulting in a decreased intensity at the wavelength corresponding to band-to-band recombination (see section 1.2.1).

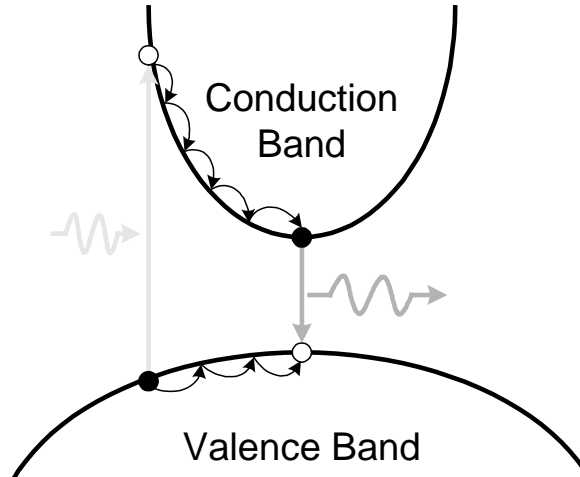


Figure 39: Schematic of PL processes in semiconductors [65].

A critical parameter in determining the PL efficiency is the lifetime, τ_{tot} :

$$\frac{1}{\tau_{\text{tot}}} = \frac{1}{\tau_{\text{nr}}} + \frac{1}{\tau_{\text{r}}}$$

with τ_{nr} the non-radiative lifetime and τ_{r} the radiative lifetime. In addition to spontaneous radiative recombination, other processes rule over the decay of photo-excited carriers. These processes that contribute to τ_{nr} are: (i) Auger recombination, (ii) trapping and recombination at impurities and defects, (iii) surface recombination, and (iv) diffusion of carriers away from the region of observation. If the non-radiative lifetime is really short, most of the generated carriers will recombine non-radiatively and the PL intensity will be very low. Therefore, it is important to minimize defects and impurities resulting in non-radiative recombination.

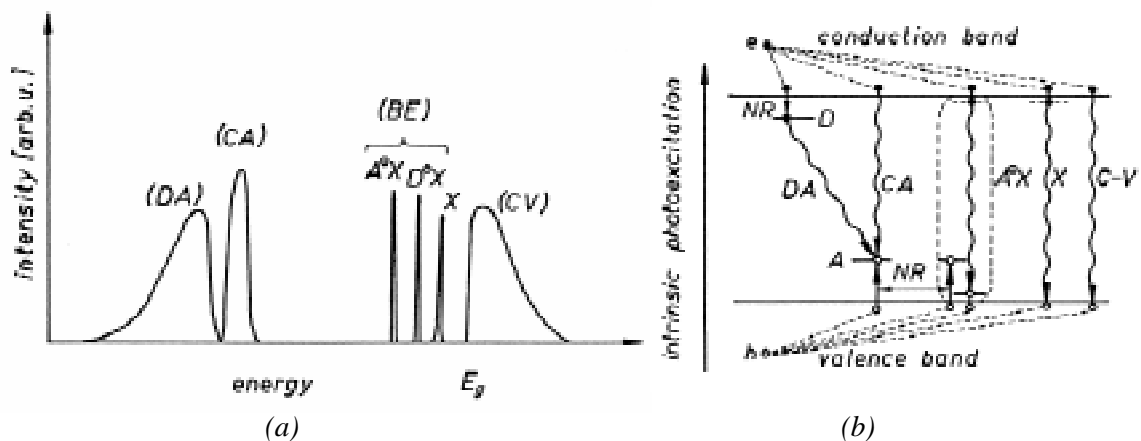


Figure 40: (a) Main parts of a near-band-edge PL spectrum, and (b) schematic representation of the corresponding recombinations [25].

The PL intensity at a particular wavelength is directly proportional to the spontaneous emission, $R_{sp}(\hbar\omega)$. The spontaneous emission is equal to the transition rate from a filled state in the conduction band to an empty state in the valence band times the probability of a filled initial state and an empty final state:

$$R_{sp}(\hbar\omega) d(\hbar\omega) \propto \sum_{i,f} \frac{2\pi}{\hbar} \left| \langle f | H'(\mathbf{r}, t) | i \rangle \right|^2 P_i P'_f \delta(E_f - E_i - \hbar\omega) d(\hbar\omega)$$

with P_i the probability that the initial state is occupied, and P'_f the probability that the final state is empty. These probabilities can be determined using Fermi-Dirac statistics as:

$$P_i = \frac{1}{1 + \exp\left(\frac{E_i - E_F^e}{k_B T}\right)} \quad \text{and} \quad P'_f = 1 - \frac{1}{1 + \exp\left(\frac{E_f - E_F^h}{k_B T}\right)}$$

with E_F^e and E_F^h the electron and hole quasi-Fermi levels. The emission and the absorption are related because at thermal equilibrium the downward and upward transition rates must be equal. Hence, the emission spectrum can be calculated from the absorption spectrum using the so-called van Roosbroeck-Shockley relation [62]:

$$R_{sp}(\hbar\omega) = \frac{8\pi}{h^3 c^2} \frac{[\hbar\omega]^2}{\left(1 + \exp\left(\frac{E_i - E_F^e}{k_B T}\right)\right) \left(1 + \exp\left(\frac{E_F^h - E_f}{k_B T}\right)\right)} \alpha(\hbar\omega)$$

with h the Planck constant which is equal to $2\pi\hbar$, and $\Delta E_F = E_F^e - E_F^h$. For direct band-to-band transitions with parabolic bands the expression for $\alpha(\hbar\omega)$ has been derived in section 3.1.1, and can be used in the above expression to find:

$$R_{sp}(\hbar\omega) \propto (\hbar\omega - E_g)^{1/2} \exp\left[-\frac{(\hbar\omega - E_g)}{k_B T}\right].$$

We have assumed a non-degenerate semiconductor, so that the Boltzmann factors can be substituted for the Fermi function. This results in a PL peak shape as shown in Figure 41 with an exponential tail toward higher energy (or lower wavelength). The peak energy ($\hbar\omega_p$) and the half-width (ΔE) of the PL band are, respectively:

$$\hbar\omega_p = E_g + \frac{1}{2} k_B T \quad \text{and} \quad \Delta E = 1.8 k_B T.$$

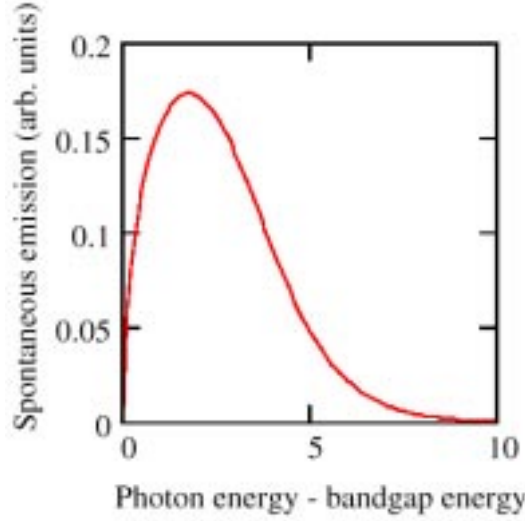


Figure 41: Spontaneous emission spectrum for a GaAs-like semiconductor [66]. Energy units are $k_B T$.

3.2.2 Model for energy levels and absorption in a quantum well

As described in section 1.2.1, laser devices have the active material in a quantum well (QW). Therefore, we need to understand the properties of a QW to study the properties of GaInNAs in a QW.

In a QW, the potential varies across the structure as shown in Figure 42(a) and Figure 43(a). The time-independent Schrödinger equation allows determining energy and wave functions resulting from this potential profile for electrons and holes:

$$\left[-\frac{\hbar^2}{2m}\nabla^2 + V(z)\right]\psi(x,y,z) = E\psi(x,y,z)$$

where m is the effective mass, $V(z)$ the potential, $\psi(x,y,z)$ the wave function, and E the energy.

The simplest QW has infinite barriers as shown in Figure 42(a). In that case, the wave function vanishes at the boundaries and the solution for the wave function and energy are:

$$\psi(x,y,z) = \frac{e^{ik_x x + ik_y y}}{\sqrt{A}} \phi_n(z) \text{ with } \phi_n(z) = \begin{cases} \sqrt{\frac{2}{L}} \sin\left(\frac{n\pi}{L}z\right) & \text{if } n \text{ even} \\ \sqrt{\frac{2}{L}} \cos\left(\frac{n\pi}{L}z\right) & \text{if } n \text{ odd} \end{cases} \text{ such that } \phi\left(-\frac{L}{2}\right) = \phi\left(\frac{L}{2}\right)$$

and

$$E = \frac{\hbar^2}{2m} \left[k_x^2 + k_y^2 + \left(\frac{n\pi}{L} \right)^2 \right]$$

with L the length of the QW, and A the cross-sectional area in the x - y plane. The solution for the envelope function $\phi_n(z)$ is plotted in Figure 42(a) and the energy dispersion diagram $E(k_x, k_y)$ is plotted in Figure 42(b).

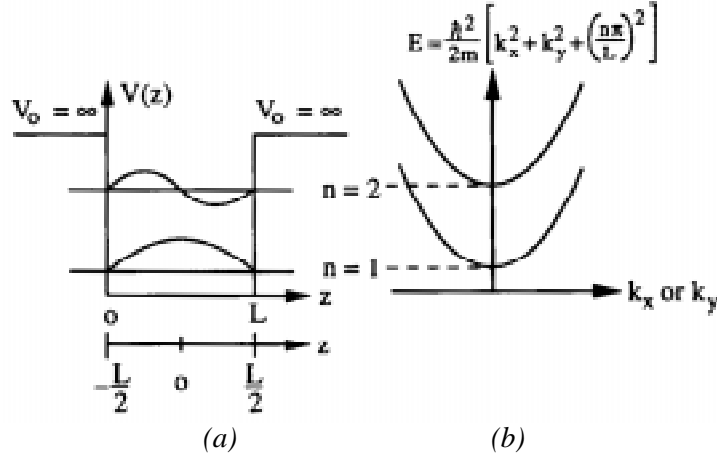


Figure 42: (a) A QW with a width L and an infinite barrier $V_0 = \infty$. (b) The energy dispersion in the k_x or k_y space [4].

A practical QW is more accurately modeled with finite barriers (see Figure 43(a)).

In this case, we have

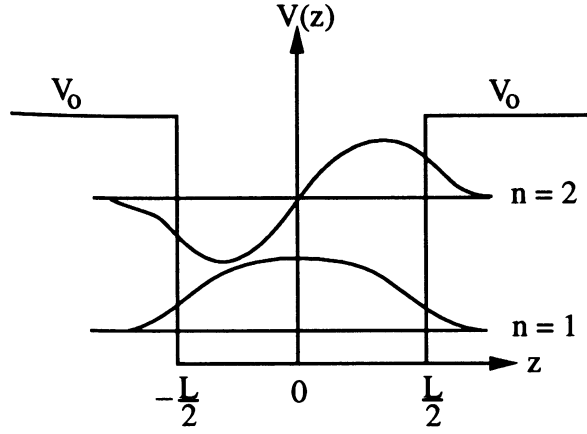
$$V(z) = \begin{cases} V_0 & \text{if } |z| \geq \frac{L}{2} \\ 0 & \text{if } |z| < \frac{L}{2} \end{cases}$$

Solving the Schrödinger equation with $m = m_w$ in the well and $m = m_b$ in the barrier gives:

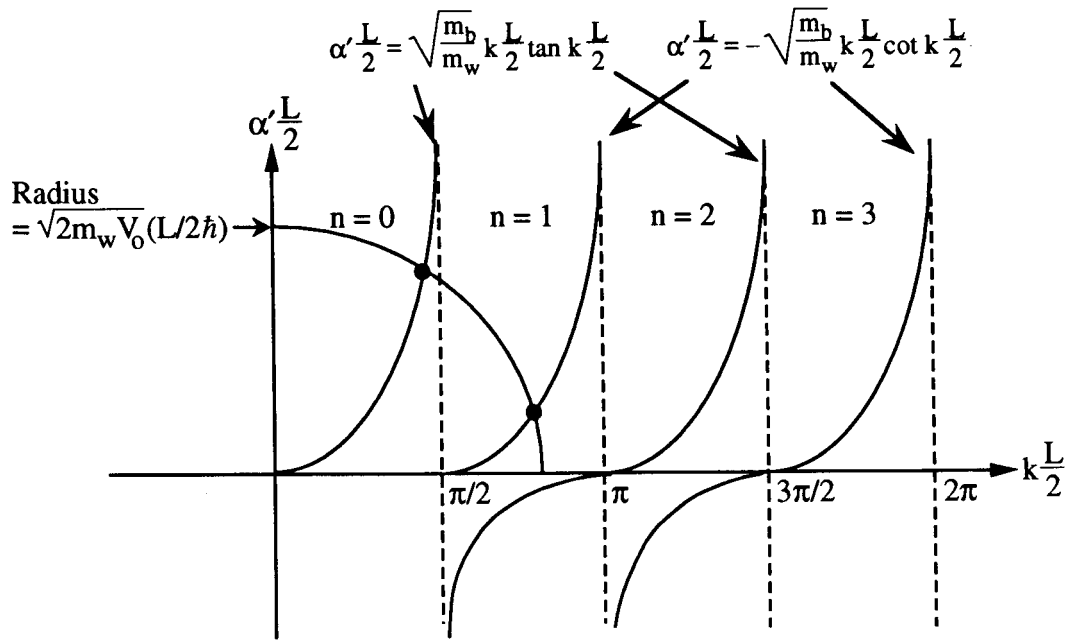
$$\phi(z) = \begin{cases} C_1 e^{-\alpha(|z|-L/2)} & \text{if } |z| \geq \frac{L}{2} \\ C_2 \cos kz & \text{if } |z| < \frac{L}{2} \end{cases} \quad \text{for the even wave functions}$$

and

$$\phi(z) = \begin{cases} C_1 e^{-\alpha(z-L/2)} & \text{if } z > \frac{L}{2} \\ C_2 \sin kz & \text{if } |z| \leq \frac{L}{2} \\ -C_1 e^{+\alpha(z+L/2)} & \text{if } z < -\frac{L}{2} \end{cases} \quad \text{for the odd wave functions}$$



(a)



(b)

Figure 43: (a) A QW with a width L and a finite barrier height V_0 . The energy levels for $n=1$ and $n=2$ and their corresponding wave functions are shown. (b) A graphical solution for the decaying constant α and wave number k of a QW with finite barriers [4].

with $k = \frac{\sqrt{2m_w E}}{\hbar}$ and $\alpha = \frac{\sqrt{2m_b (V_0 - E)}}{\hbar}$.

The boundary conditions require that the wave function and its first derivative divided by the effective mass be continuous at the interface between the barrier and the well:

$$\phi\left(\frac{L^+}{2}\right) = \phi\left(\frac{L^-}{2}\right) \quad \text{and} \quad \frac{1}{m_b} \frac{d}{dz} \phi\left(\frac{L^+}{2}\right) = \frac{1}{m_w} \frac{d}{dz} \phi\left(\frac{L^-}{2}\right).$$

These conditions are satisfied when

$$\alpha = \frac{m_b k}{m_w} \tan k \frac{L}{2} \quad \text{for the even wave functions}$$

and when

$$\alpha = -\frac{m_b k}{m_w} \cot k \frac{L}{2} \quad \text{for the odd wave functions.}$$

The solutions for the eigen energies in a QW with finite barriers can be obtained graphically as shown in Figure 43(b) from

$$\left(k \frac{L}{2}\right)^2 + \left(\alpha' \frac{L}{2}\right)^2 = \frac{2m_w V_0}{\hbar^2} \left(\frac{L}{2}\right)^2 \text{ and}$$

$$\begin{cases} \alpha' \frac{L}{2} = \sqrt{\frac{m_b}{m_w}} k \frac{L}{2} \tan k \frac{L}{2} & \text{for the even wavefunctions} \\ \alpha' \frac{L}{2} = -\sqrt{\frac{m_b}{m_w}} k \frac{L}{2} \cot k \frac{L}{2} & \text{for the odd wavefunctions} \end{cases}$$

with $\alpha' \equiv \alpha \sqrt{\frac{m_w}{m_b}}$. These solutions for k and E are smaller than for a QW with infinite

barriers. The reduced carrier confinement results in a decrease of the energy levels as if the QW was widened. Indeed, for the case of $m_w = m_b = m$ the solutions for the energy and the wave function are [4]:

$$E_n = \frac{\hbar^2}{2m} \left(\frac{n\pi}{L_{\text{eff}}}\right)^2 \text{ and } \phi_n(z) = \sqrt{\frac{2}{L_{\text{eff}}}} \sin\left(\frac{n\pi}{L_{\text{eff}}} z\right) \text{ with } L_{\text{eff}} = L + 2/\alpha.$$

The electron density, n , in a quantum well with infinite barriers can be calculated using

$$n = \frac{2}{V} \sum_n \sum_{k_x} \sum_{k_y} P(E)$$

with the summation over all the occupied subbands. By converting the sum into an integration so that

$$n = \int dE \rho_{2D}(E) P(E),$$

we find the two dimensional density of states (see Figure 44):

$$\rho_{2D}(E) = \frac{m}{\pi \hbar^2 L_z} \sum_n H(E - E_n)$$

with E_n is defined as $\frac{\hbar^2}{2m} \left(\frac{n\pi}{L}\right)^2$, and $H(x)$ a Heaviside step function $H(x) = 1$ for $x > 0$ and $H(x) = 0$ for $x < 0$. When the energy is equal to E_n , the three-dimensional density of states ($\rho_{3D}(E) = \frac{1}{2\pi^2} \left(\frac{2m}{\hbar^2}\right)^{3/2} \sqrt{E}$) and the two dimensional density of states ($\rho_{2D}(E)$) coincide.

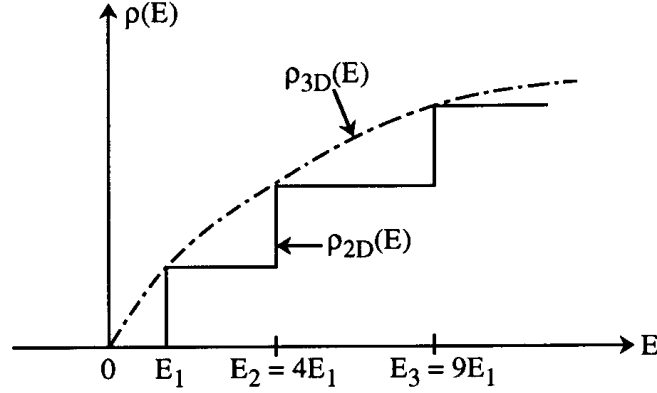


Figure 44: The electron density of states $\rho_{2D}(E)$ (solid line) for a two-dimensional QW structure compared with the three-dimensional density of states $\rho_{3D}(E)$ (dashed curve) [4].

We can use the above knowledge to derive PL spectra from a QW. In section 3.1.1, we have shown that the absorption follows the behavior of the joint density of states. In this section, we have observed that the density of states in a QW is different from the density of states in a bulk semiconductor. We can derive the absorption from a QW using the same equations as before to get:

$$\alpha(\hbar\omega) = \frac{\pi e^2}{2n_r c \epsilon_0 m_0 \omega} E_p \sum_{n,m} |I_{nm}^{en}|^2 \frac{m_r}{\pi \hbar^2 L_z} H(\hbar\omega - E_{nm}^{en})$$

with $E_{nm}^{en} = E_g + E_{en} - E_{hm}$ in which E_{en} and E_{hm} are the energies for the electron and hole respectively, and $I_{nm}^{en} = \int dz \phi_n^* \phi_m(z)$ the overlap integral of the conduction- and valence-band envelope functions. For an infinite QW $I_{nm}^{en} = \delta_{nm}$ and $\alpha(\hbar\omega)$ is given by

$$\alpha(\hbar\omega) = \frac{\pi e^2 \hbar}{2n_r c \epsilon_0 m_0} \frac{E_p}{\hbar\omega} \begin{cases} \frac{m_r}{\pi \hbar^2 L_z} & \text{for } E_{h1}^{e1} < \hbar\omega < E_{h2}^{e2} \\ 2 \frac{m_r}{\pi \hbar^2 L_z} & \text{for } E_{h2}^{e2} < \hbar\omega < E_{h3}^{e3} \\ 3 \frac{m_r}{\pi \hbar^2 L_z} & \text{for } E_{h3}^{e3} < \hbar\omega < E_{h4}^{e4} \\ \text{etc.} & \end{cases}.$$

We have again assumed that the valence band is completely filled and the conduction band is completely empty. If this is not the case, the absorption with injected carriers, α_j , can be found as [4]:

$$\alpha_j(\hbar\omega) = \alpha(\hbar\omega) [P_m(\hbar\omega - E_{hm}^{en}) - P_n(\hbar\omega - E_{hm}^{en})]$$

with $P_m(\hbar\omega - E_{hm}^{en}) - P_n(\hbar\omega - E_{hm}^{en})$ the Fermi-Dirac population inversion factor. The relationship between absorption and spontaneous emission gives a spontaneous emission spectrum of the form:

$$R_{sp}(\hbar\omega) = \frac{8\pi}{h^3 c^2} [\hbar\omega]^2 P_n (1 - P_m) \alpha(\hbar\omega)$$

which still has the typical shape shown in Figure 41.

3.2.3 Photoluminescence from GaNAs and GaInNAs quantum wells and effect of anneal

As the luminescence properties of GaInNAs QWs are strongly correlated to device performance, PL measurements on these QWs are an important tool to optimize this new material system for light emitting devices.

A typical PL spectrum from GaInNAs QWs is shown in Figure 45. The PL peak results from the transition of electrons from the first energy level in the conduction band of the QW to the first energy level in the valence band of the QW (direct band-to-band transitions). As expected for QWs with this nitrogen and indium concentration (see section 3.1.1), the emission peaks beyond 1.3 μm in the as-grown material. However, the luminescence efficiency is very low and this material is not good enough to make useful devices. It has been shown that annealing can significantly improve the luminescence efficiency of these alloys [67,68]. This was also the case for our structures (see Figure 45(b)). However, it is also obvious that the spectrum shifts to shorter

wavelengths during anneal. The resulting peak emission is below 1.3 μm even though the starting material was emitting beyond 1.3 μm . Annealing GaInNAs alloys significantly improves the luminescence efficiency but also results in a blue shift of the emission. The origin of improvement in the luminescence efficiency and blue shift of the peak emission will be discussed in detail in further sections (3.2.4 and 3.2.5). All samples were rapid thermal annealed in an AG heatpulse 310.

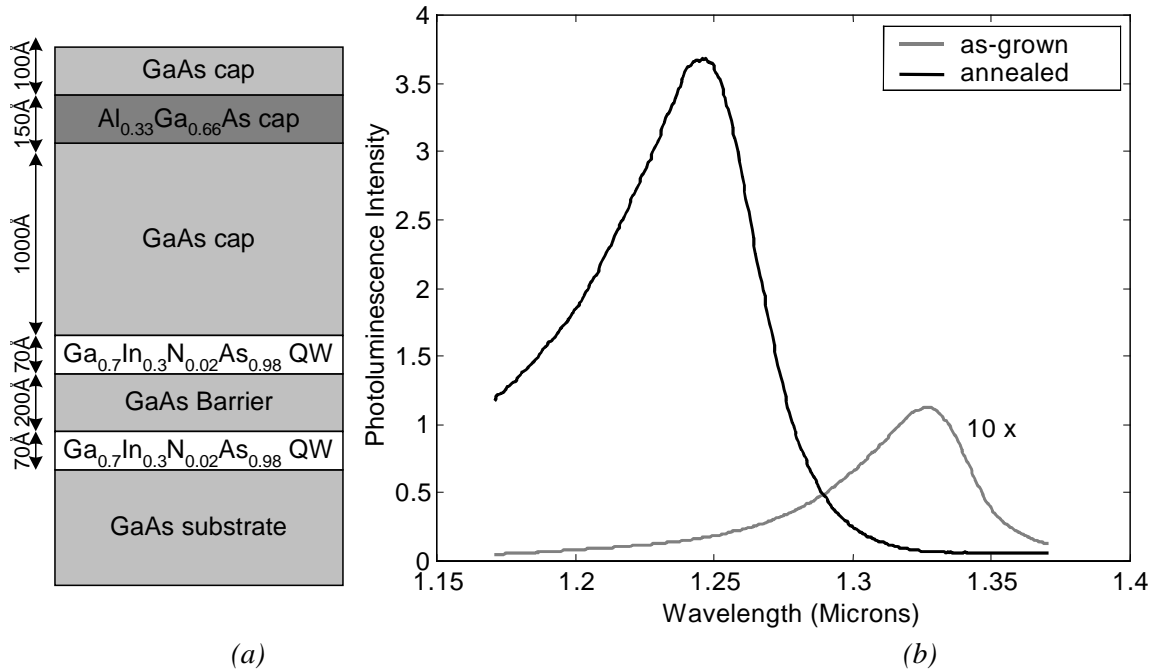
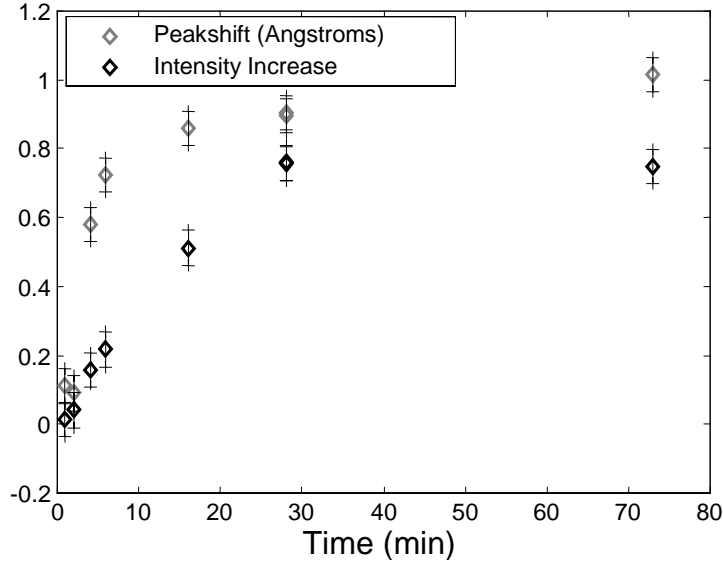


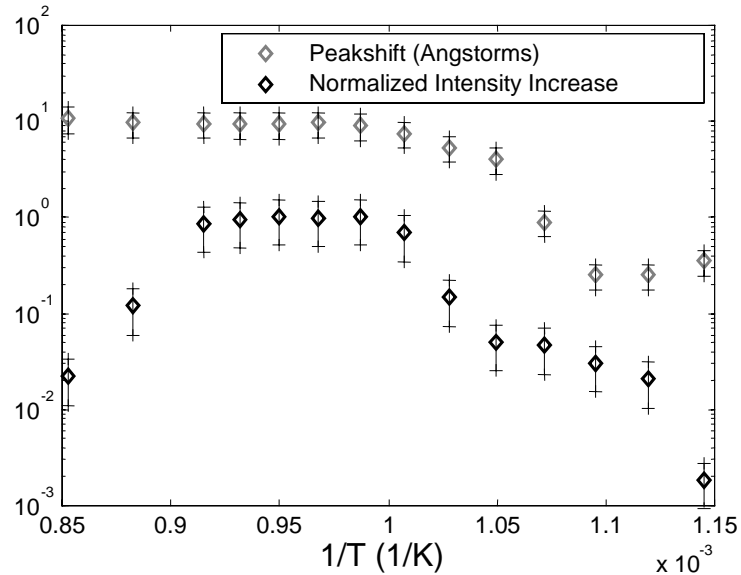
Figure 45: (a) Sample structure and (b) photoluminescence spectrum of as-grown and annealed 70 Å $\text{Ga}_{0.7}\text{In}_{0.3}\text{N}_{0.02}\text{As}_{0.98}$ QWs with GaAs barriers. The samples were proximity capped with GaAs and annealed for 60 seconds at 760 °C under a N_2 ambient.

The increase in luminescence efficiency is due to the decrease of non-radiative recombination centers in the QWs. The wavelength shift can be ascribed to either or both group V or group III inter-diffusion. A study of the dependence of luminescence efficiency and peak shift on anneal temperature and time was done to determine whether one could maximize the luminescence efficiency without causing a significant peak shift. Figure 46(a) shows the photoluminescence intensity and wavelength shift as a function of the annealing time when annealing proximity capped 70 Å GaInNAs/GaAs quantum well samples at 660 °C in N_2 ambient. Initially, the intensity increases linearly with time; it saturates after 30 minutes indicating that most of the non-radiative recombination centers have disappeared. The peak shift shows a similar behavior; at first the shift increases

rapidly with time, but after 30 minutes, the peak shift increases only slightly. Figure 46(b) shows the behavior of luminescence intensity and wavelength shift for samples annealed for 1 minute at various temperatures in a N_2 ambient. The majority of the traps are annealed after a 1 minute anneal at 760 °C. The peak shift remains constant once most of the traps are annealed. The decrease of the photolumuminescence intensity when



(a)



(b)

Figure 46: Room-temperature photoluminescence intensity and wavelength shift of 70Å $Ga_{0.7}In_{0.3}N_{0.02}As_{0.98}/GaAs$ quantum wells as function of (a) anneal time for anneal temperature of 660 °C and (b) anneal temperature for an anneal time of 60 seconds. Excitation was from the 514nm line of an Ar^+ ion laser. Samples were proximity capped and annealed under N_2 ambient.

annealing at temperatures above 790 °C is most likely due to arsenic desorption from the surface. For all these annealing conditions the intensity increase and the peak shift occur together. It seems impossible to maximize the luminescence efficiency while avoiding the wavelength shift.

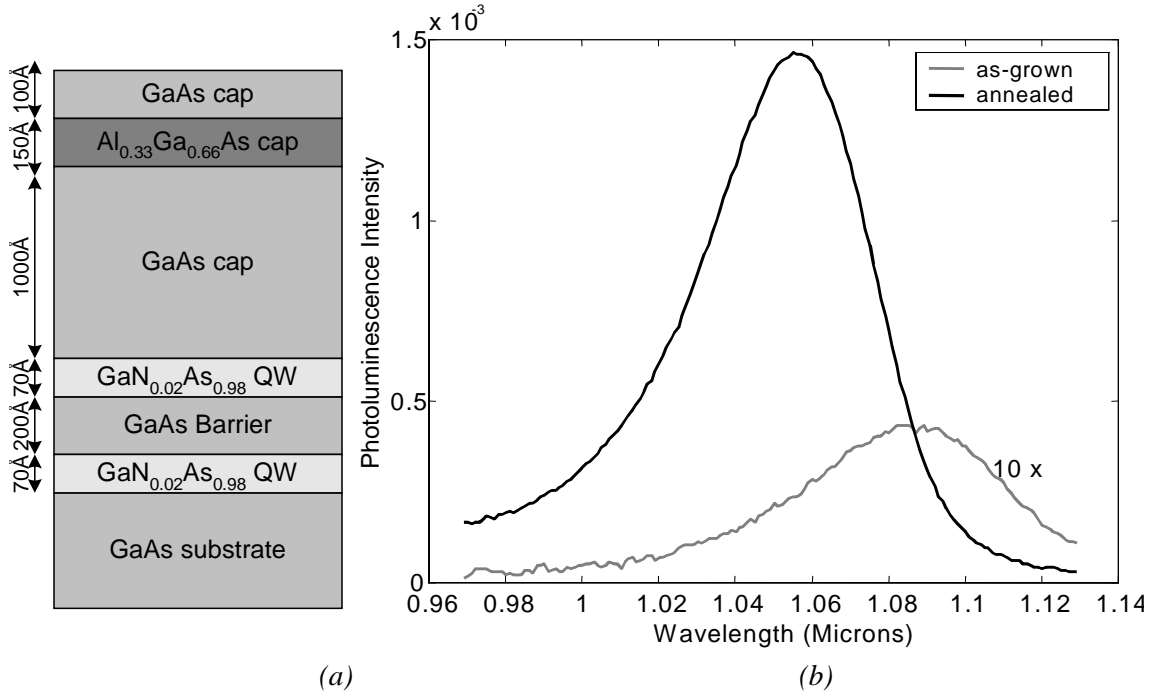


Figure 47: (a) Sample structure and (b) photoluminescence spectrum of as-grown and annealed 70 Å $\text{GaN}_{0.02}\text{As}_{0.98}$ quantum wells with GaAs barriers. The sample was proximity capped and annealed for 60 seconds at 760 °C under a N_2 ambient.

As a first step towards understanding the mechanisms responsible for the photoluminescence efficiency increase and blue shift of the peak emission during the anneal of nitride-arsenides, we have analyzed the PL of of GaNAs QWs before and after anneal (see Figure 47). One observes exactly the same PL behavior when annealing GaNAs QWs as when annealing GaInNAs QWs: a dramatic increase in luminescence efficiency occurring with a simultaneous shift of the peak emission to shorter wavelengths. The wavelength shift of the spectrum is less for GaNAs QWs than for GaInNAs QWs. The previous section has shown that energy is a more direct measure for the properties of the QW. This difference in blue shift during the anneal is less significant when expressed in terms of change in energy: 0.061 eV for the GaInNAs QWs versus 0.034 eV for the GaNAs QWs. For GaNAs QWs the only diffusing species are arsenic and nitrogen. Hence, the group V interdiffusion is the cause of the blue shift of

the spectrum from GaNAs QWs during anneal. As GaNAs QWs also show a significant luminescence increase after anneal, one can deduce that the traps responsible for the decreased luminescence efficiency of as-grown nitride-arsenides are related to a crystal defect or an impurity associated with the nitrogen and not related to indium. The origin of this trap will be described in detail in section 3.2.4. As shown in Figure 48, we observe that the photoluminescence efficiency of the InGaNAs QWs decreases substantially with increasing nitrogen composition. The slight increase in the InGaAs QW luminescence is also due to the fact that the non-radiative trap concentration is lower in the GaInNAs: since a smaller fraction of the generated carriers recombine non-radiatively, more carriers are available for radiative recombination in the InGaAs QWs. The slight difference in the luminescence from the InGaAs QWs is due to small differences of the QW composition between the samples.

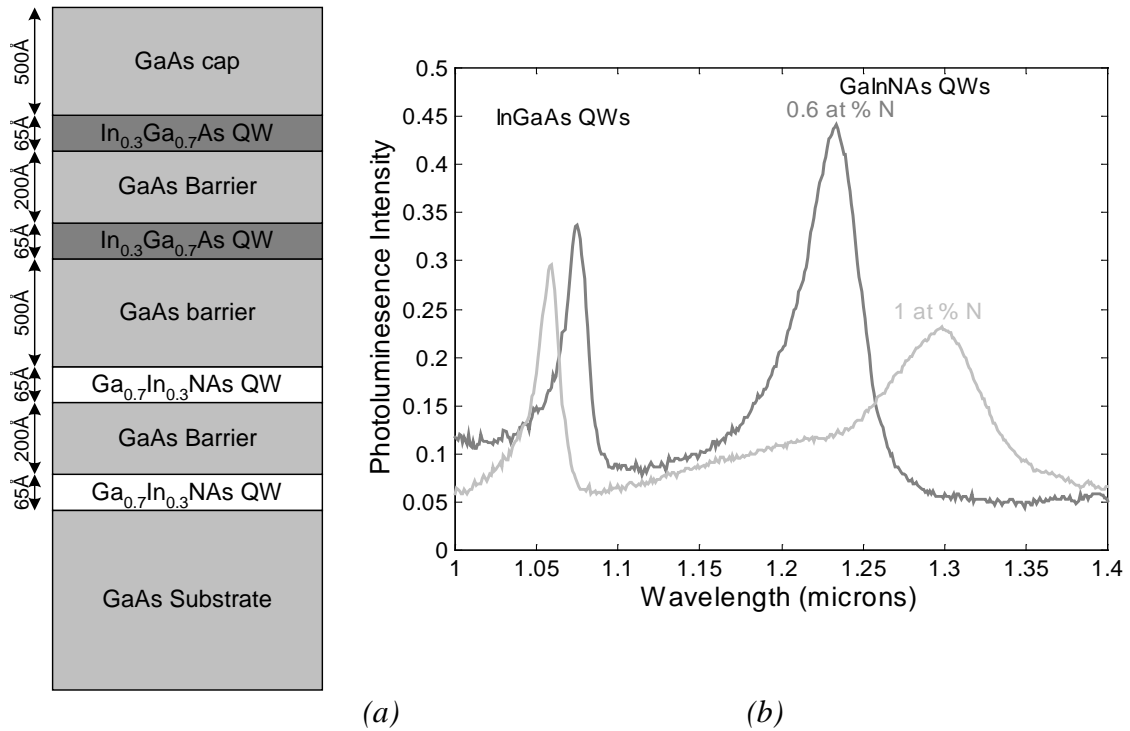


Figure 48: (a) Sample structure and (b) photoluminescence spectrum of as-grown 65 Å $Ga_{0.7}In_{0.3}N_{0.012}As_{0.988}$ and $Ga_{0.7}In_{0.3}N_{0.02}As_{0.98}$ quantum wells with GaAs barriers.

3.2.4 Origin of intensity increase when annealing GaNAs

3.2.4.1 Introduction

The PL data in Figure 47 and Figure 48 indicate that as-grown GaInNAs and GaNAs QWs contain a non-radiative recombination center caused by a crystal defect or

an impurity associated with the nitrogen. Because the annealed nitride-arsenide QWs have a significantly higher luminescence efficiency, the concentration of this center must decrease during an anneal. In this section the exact origin of this center will be investigated.

The presence of a trap that disappears upon anneal was also observed in capacitance voltage (CV) measurements. Figure 49 shows the results from CV measurements on GaNAs. The capacitance of a metal semiconductor junction is given by:

$$C = \left| \frac{dQ_s}{dV} \right| = \sqrt{\frac{q\epsilon_s N_d}{2(\phi_i - V_a)}} = \frac{\epsilon_s}{x_d}.$$

Hence, the carrier concentration is given by:

$$N(x_d) = \frac{-2}{q\epsilon_s [d(1/C^2)/dV_a]}.$$

By biasing the metal semiconductor junction at gradually increasing voltages and applying an small ac voltage variation around the bias voltage, the carrier concentration is determined at different depths with the assumption that the charge state of the traps remains constant during this process [69]. The measurements were been done at a temperature of 300 K and a frequency of 1 MHz. The sample structures are shown in Figure 49(a) and Figure 49(c). As shown in Figure 49(b), the as-grown sample has a lower hole concentration in the QW than the annealed sample, although the doping concentration is the same. This suggests that the as-grown GaNAs QW contains defects that trap the free carriers. A rapid thermal anneal increases the free hole concentration in the well significantly, indicating that annealing reduces the extent of free carrier trapping in the GaNAs material. The higher hole concentration in the well implies that the valence band energy in GaNAs is higher than in GaAs (type I band allignment) [6]. For n-type GaNAs QWs, similar behavior is observed (see Figure 49(d)). Whereas the electrons in as-grown GaNAs are trapped, there is a drastic increase of the electron concentration after annealing. The depleted regions adjacent to the GaNAs layer demonstrate that the conduction band edge of GaAs is higher than that of GaNAs. The peaks at 700 nm which are associated with interfacial states are removed by annealing.

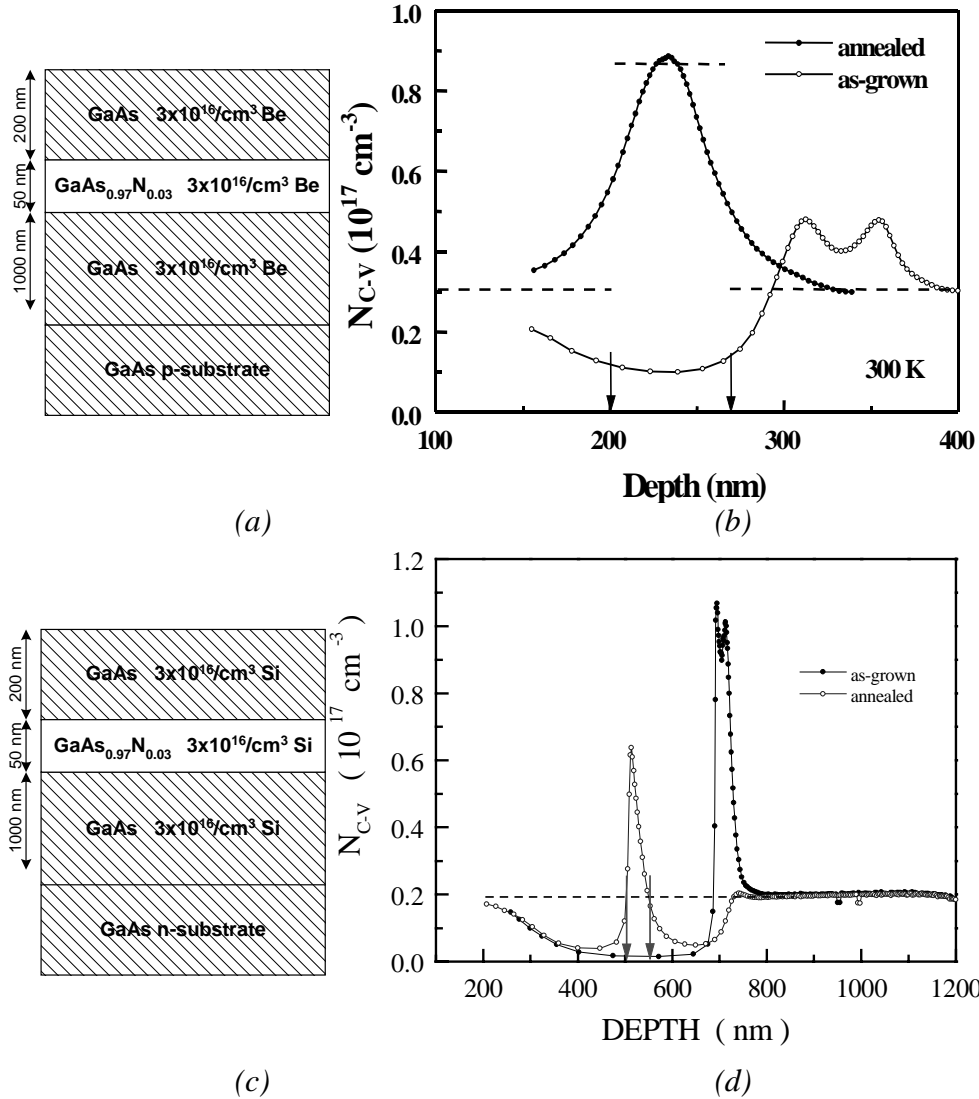


Figure 49: (a) Sample structure and (b) free hole profile of a p-doped as-grown and annealed 500 Å GaN_{0.03}As_{0.97} quantum well with GaAs barriers. The sample was proximity capped and annealed for 60 seconds at 760 °C under a N₂ ambient, (c) Sample structure and (b) free electron profile of a n-doped as-grown and annealed 500 Å GaN_{0.03}As_{0.97} quantum well with GaAs barriers. The sample was proximity capped and annealed for 60 seconds at 760 °C under a N₂ ambient.

Saito et al. [58], Xin et al. [70], and Geisz et al. [71] postulated that this trap was due to hydrogen impurities. They have observed that during the growth of nitride-arsenides by MOCVD and gas source MBE, hydrogen present in the group V gas sources is incorporated. They have also observed changes in the hydrogen profile when annealing. When growing nitride-arsenides by MBE using an rf plasma [72,73] the hydrogen incorporation is significantly lower (see section 2.1.1.2) but we still observe the same increase of luminescence efficiency during anneal. As the impurity concentration

in our films is low, we have investigated crystal defects associated with nitrogen incorporation.

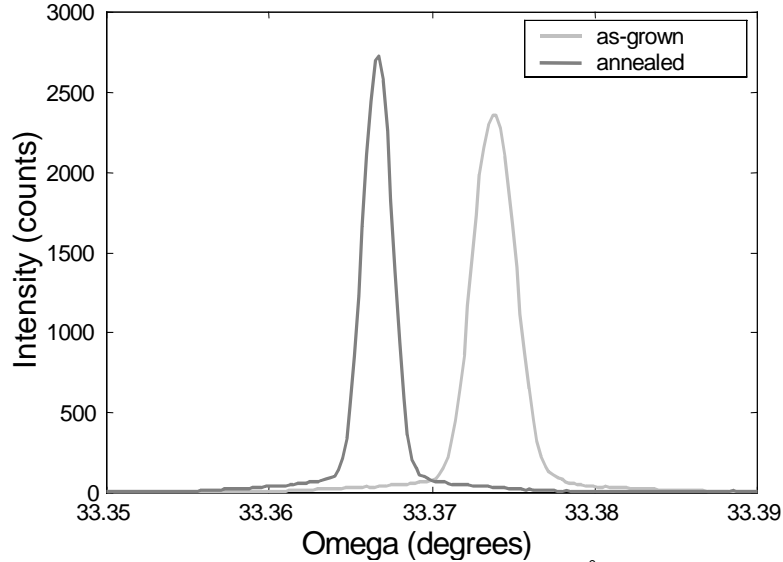


Figure 50: HRXRD rocking curve of the 004 peak from a 2500 Å $\text{GaN}_{0.025}\text{As}_{0.975}$ film on GaAs. The sample was proximity capped and annealed for 5 min at 760 °C under a N_2 ambient.

Annealing indeed improves the crystal quality of a $\text{GaN}_{0.025}\text{As}_{0.975}$ film as indicated by increased X-ray diffraction intensity and decreased full width half maximum (FWHM) of the peaks in a HRXRD rocking curve measurement. Figure 50 shows the diffracted intensity increase and the FWHM decrease of the (004) peak after anneal. The slight shift of the peak is caused by nitrogen out-diffusion (see section 3.2.5). An increase in diffracted intensity and decrease of FWHM was also observed for a rocking curve measurement around the (002), (224), (115) and (044) peaks. We have also demonstrated increased diffracted intensity and hence increased crystal quality after annealing a 6 period 70 Å $\text{GaN}_{0.05}\text{As}_{0.95}/130$ Å GaAs superlattice (see Figure 51). Nitrogen diffusion is again responsible for the slight shift of the peaks.

3.2.4.2 Evidence for non-substitutional nitrogen incorporation

The origin of this crystal defect related to nitrogen incorporation is investigated by studying the lattice parameter of as-grown GaNAs as a function of the nitrogen concentration and by analyzing the nitrogen binding configuration with X-ray photoelectron spectroscopy (XPS).

To analyze the lattice parameter versus nitrogen concentration, we have grown GaNAs films with a thickness around 1800 Å with nitrogen concentrations varying between 2 mol % GaN and 4 mol % GaN. The lattice parameter was measured using

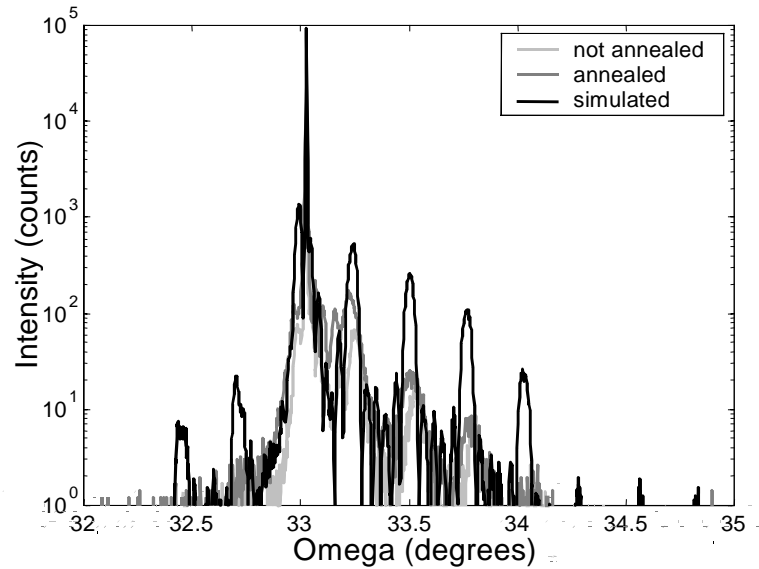


Figure 51: HRXRD rocking curve from an annealed and as-grown 6 period 70 \AA $\text{GaN}_{0.05}\text{As}_{0.95}/130 \text{ \AA}$ GaAs superlattice. Annealing was done for 10 seconds at $775 \text{ }^\circ\text{C}$.

HRXRD as described in section 2.3. The nitrogen concentration was measured with SIMS after calibration with a known GaNAs standard. We have observed that the relationship between lattice parameter and nitrogen concentration in GaNAs films is not linear for nitrogen concentration above 2.9 mole % GaN (see Figure 52). Neugebauer et al. [3] have shown that Vegard's law is valid for this alloy when nitrogen is substituted for arsenic. Our observed deviation from Vegard's law suggests that some nitrogen is incorporated on other locations than the group V lattice sites. The fact that nitrogen is such a small atom compared to gallium and arsenic makes this incorporation on other sites than the group V lattice sites more likely.

If the nitrogen is incorporated on other than group V lattice sites, the nitrogen should be present in more than one type of bond. XPS analysis was done to analyze the nitrogen binding configuration. A Magnesium source was used for the XPS measurements to avoid overlap between a gallium Auger peak and the N(1s) peak. The escape angle was 65° (maximum value possible in the instrument used) to sample as deep as possible into the sample. The N(1s) spectrum for a $\text{GaN}_{0.06}\text{As}_{0.94}$ film covered with GaAs cap (see Figure 53) indicates that nitrogen exists in two configurations: a covalent Ga-N bond plus another nitrogen-complex in which nitrogen is less strongly bonded to gallium atoms. As the GaNAs layer is buried with a GaAs cap, surface contamination

should have no influence on the shape of the nitrogen peak. Annealing removes this nitrogen complex but also results in out-diffusion of nitrogen.

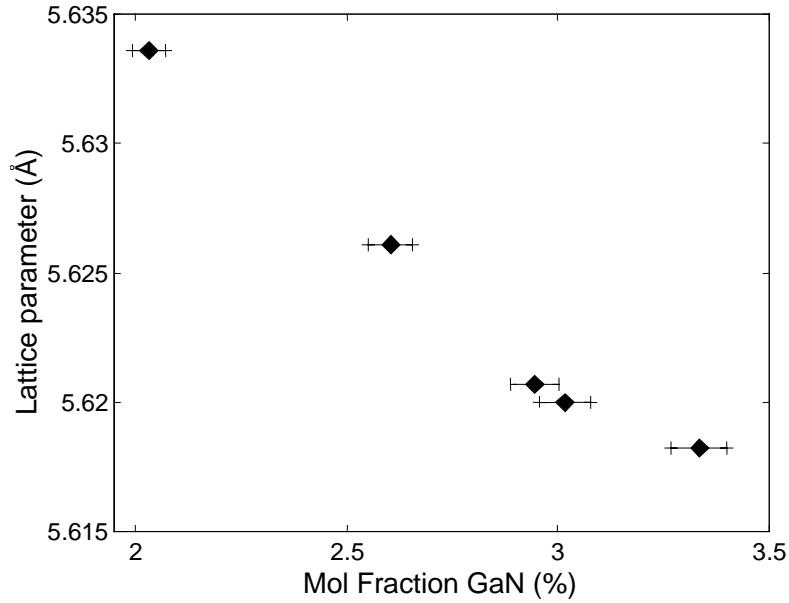


Figure 52: Lattice parameter of different GaNAs films as function of nitrogen concentration. The lattice parameter of the films was determined using HRXRD in a Philips Materials Research Diffractometer. The nitrogen concentration was measured by SIMS in a CAMECA IMS 4.5f instrument.

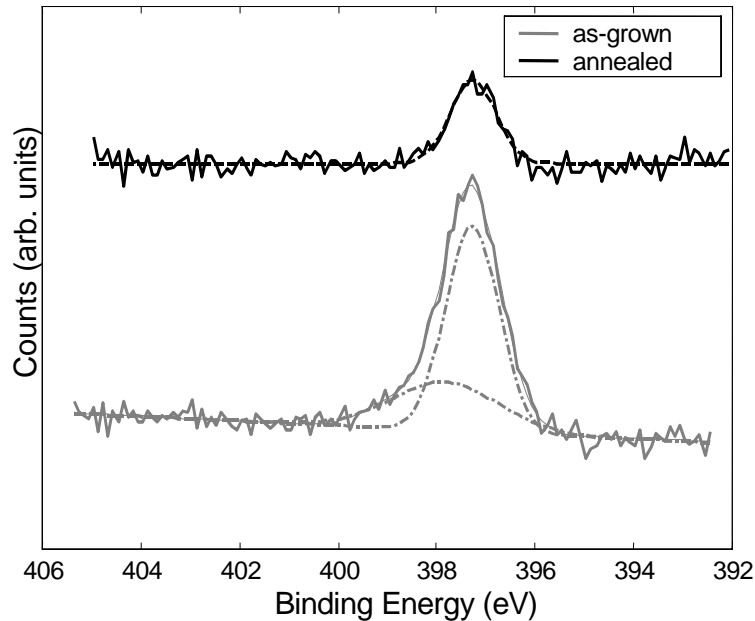


Figure 53: XPS signal from N(1s) peak from annealed and as-grown $\text{GaN}_{0.06}\text{As}_{0.94}$ film measured in a PHI 5800 instrument. The gallium Auger peak around 398 eV was removed by dividing the obtained spectrum by the spectrum of a GaAs reference sample. Annealing was done for 30 seconds at 775 °C under a N_2 ambient with proximity capping.

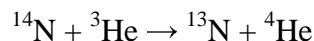
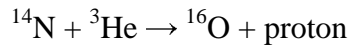
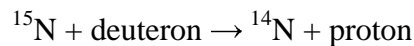
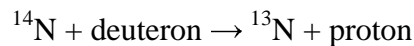
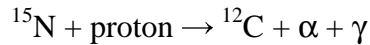
The two previous experiments show that there is a crystal defect associated with nitrogen incorporation that is annealed out. The next section will explain the origin of this defect.

3.2.4.3 Demonstration of interstitial nitrogen incorporation

Rutherford backscattering (RBS) channeling studies are a useful tool to determine how an atom is incorporated into a lattice [38]. However, because nitrogen is so light the amount of backscattering is too low to analyze the concentration and location of nitrogen. However, if one combines channeling techniques with nuclear reaction analysis (NRA), the heavy mass background is removed and the nitrogen signal is strong enough to do channeling analysis.

In RBS, a sample is bombarded with a beam of high-energy particles (usually He ions) that collide with the atomic nuclei. When the rows of atoms in the lattice are aligned parallel to the incident beam, the backscattering from buried atoms in the lattice is drastically decreased since these atoms are shielded from the incident particles by the atoms in the surface layers. The backscattering yield is reduced compared to the random orientation of the sample. Deviations from the idealized lattice structure change the backscattered flux intensity and can be used for investigating effects such as thermal vibrations, lattice relaxation, lattice reconstruction, interstitial atom positions, adsorbate locations and surface disorder [38].

NRA [65] is used to determine the concentration and depth distribution of light elements near the surface (first few μm). A beam of charged particles with energy from a few hundred keV to several MeV is accelerated to bombard the sample. This beam induces nuclear reactions with low mass nuclei in the sample. Possible reactions for nitrogen are:



Products of these reactions (such as protons, deuterons, ^4He , α particles, and γ rays) are detected. Because this method relies on nuclear reactions, it is insensitive to solid state matrix effects and it is easily made quantitative without reference samples.

For this analysis, we have used the reaction $^{14}\text{N} + ^3\text{He} \rightarrow ^{16}\text{O} + \text{proton}$. A 2.5 MeV ^3He analysis beam is used. The protons are detected. The difficulty with the above reaction is the small cross section ($\sim 10^{-32} \text{ m}^2/\text{steradian}$) of this reaction [74]. The detector is placed behind the sample and very close to the sample to produce a large collection angle. The protons are energetic enough to pass through the GaAs sample to the detector. The ^3He does not produce any nuclear reactions with gallium or arsenic at this energy. We have checked the count rates for carbon and oxygen contamination by hitting carbon and SiO_2 targets. The measured proton count rates for these test targets are low, thus assuring that the count rate from the much lower oxygen and carbon coverage on the samples should be negligible. The combined NRA channeling technique was first tested on a GaN sample (2 μm GaN on 300 μm sapphire substrate) with an analysis beam dose of 2 μC . We obtained 4177 counts for a random alignment and 303 counts with the analysis beam aligned with the c-axis. Hence, the backscattered intensity is reduced to 7.3 % of the random intensity when aligning the c-axis of the sample with the incident beam: $\chi = 7.3 \%$. Therefore, the combination of this nuclear reaction with channeling is possible.

The sample we studied consisted of a 2000 \AA $\text{GaN}_{0.03}\text{As}_{0.97}$ film on a (100) GaAs substrate (see Figure 54). The measured the NRA proton yields of annealed and as-grown samples with an incident beam of 20 μC for random and $\langle 100 \rangle$ aligned conditions are shown in Table 4. For comparison, the χ_{min} (ratio of aligned yield/unaligned yield) is 6 % for backscattering of 2.5 MeV ^3He from gallium in the samples. This χ_{min} reflects the change in analysis beam flux at the lattice sites due to channeling. Hence, the value of χ_{min} for the nitrogen NRA yield should also be about 6 % if the nitrogen is all on substitutional lattice sites. The observation that the ratio of aligned yield/unaligned NRA yield for the not-annealed sample is substantially larger than 6 % shows that a considerable portion of the nitrogen is incorporating non-substitutionally. The yield of the aligned sample is considerably lower after anneal. This indicates that a substantial fraction of the non-substitutional nitrogen disappeared during anneal. This non-

substitutional behavior is possible because the nitrogen atom is small (covalent radius 0.7 Å) compared to interstitial sites in a zinc-blende lattice.

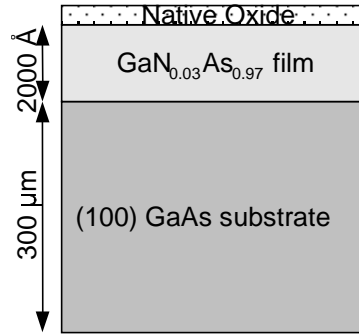


Figure 54: Sample structure for the NRA measurements.

Unfortunately, channeling measurements do not distinguish between the possible non-substitutional sites and possible chemical states for nitrogen: molecular N₂, randomly distributed atomic nitrogen, etc. However, they show the presence of interstitial nitrogen in as-grown GaNAs and a significant decrease in the concentration of interstitial nitrogen after anneal. The combination of HRXRD, XPS and NRA channeling suggests that the interstitial nitrogen might be the defect responsible for the trapping of carriers and low photoluminescence efficiency in as-grown nitride-arsenide alloys.

| Counts | Aligned <100> | Unaligned | Ratio |
|----------|---------------|-----------|--------------|
| As-grown | 102 | 390 | 0.262 ± 0.03 |
| Annealed | 59 | 390 | 0.160 ± 0.02 |

Table 4: NRA signal from annealed and as-grown GaN_{0.03}As_{0.97} film. Annealing was done for 1 min at 760 °C under Argon ambient with proximity capping.

3.2.4.4 Possible mechanism for interstitial nitrogen formation

Section 2.4.3 presented Zhang's [51] model for surfaced enhanced nitrogen incorporation. This model can also explain higher incorporation of interstitials at the surface. The substantial surface strain caused by the (2×4) reconstruction during MBE growth can be released by incorporating interstitials above the β sites. We expect a higher concentration of interstitials at the surface that can then be frozen in as the growth proceeds. Again, because nitrogen atoms and even N₂ molecules are small compared to the radius of the interstitial sites, the incorporation of nitrogen on these sites seems to be the most likely configuration of the non-substitutional nitrogen.

3.2.4.5 Conclusion

We have shown that nitrogen is incorporated into interstitial sites in the lattice. The amount of interstitial nitrogen reduces significantly when annealing. The combination of HRXRD, XPS, SIMS and combined NRA channeling suggests that the interstitial nitrogen might be the defect responsible for the trapping of carriers and the low photoluminescence efficiency in as-grown nitride-arsenide alloys.

3.2.5 Origin of wavelength shift when annealing GaNAs and GaInNAs

In the previous section, we have demonstrated that the amount of interstitial nitrogen in nitride-arsenides reduces during anneal resulting in increased PL intensity of annealed nitride-arsenides. In this section, we will investigate the origin of the shift of the photoluminescence spectrum during anneal.

As shown in Figure 48, the photoluminescence of GaNAs shifts to shorter wavelengths when annealing. The blue shift of the photoluminescence spectrum is due to a change in the energy band potential profile in the QW because of changes in composition and/or narrower width of the QW. Diffusion during anneal will not narrow the QW but changes in composition need to be considered. In the case of GaNAs QWs with GaAs barriers, the only diffusing species are nitrogen and arsenic. Nitrogen diffusion out of GaNAs QWs has been characterized [75] and yields the observed shift to shorter wavelengths. These observed and simulated nitrogen concentration profiles are shown in Figure 55. To obtain an anomalous concentration profile like this, nitrogen and arsenic must interdiffuse through a kick-out mechanism in which an interstitial nitrogen kicks out an arsenic from the lattice, resulting in an interstitial arsenic and a substitutional nitrogen atom or vice versa. This results in both nitrogen and arsenic diffusing through an interstitial mechanism. The observed effective diffusion coefficient for nitrogen is many orders of magnitude larger than the effective diffusion coefficient for arsenic. This indicates that the interstitial-to-substitutional ratio is bigger for nitrogen than for arsenic. Because a nitrogen atom is smaller than an arsenic atom, one can expect that the reverse kick-out mechanism (which produces interstitial nitrogen) is favored by local strain effects. The experimental data from [75] do not reveal whether the fast diffusing nitrogen species are interstitial nitrogen atoms or interstitial N₂ molecules.

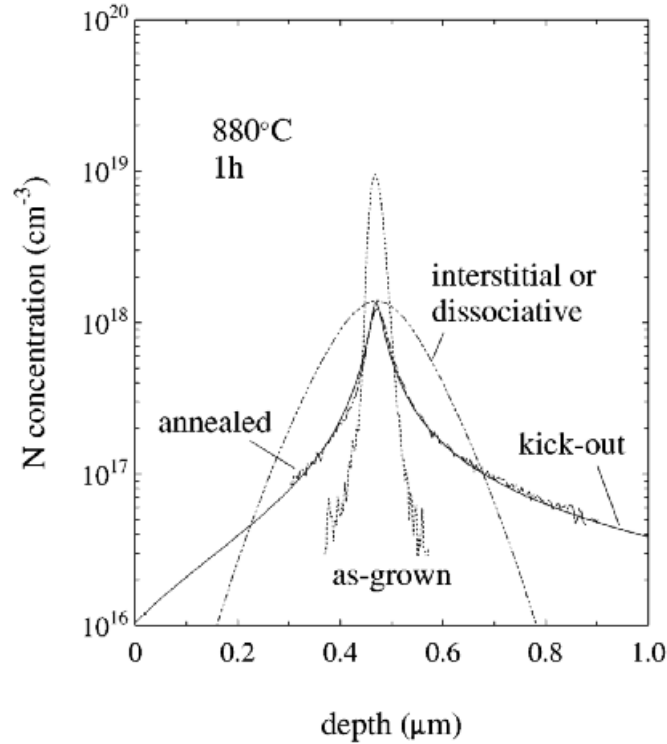


Figure 55: Nitrogen distribution after annealing compared with the as-grown starting profile. Computer-simulated curves demonstrate the validity of the kick-out mechanism as well as the failure of the dissociative mechanism, the interstitial mechanism, and other Gaussian-like broadening [75].

In the case of GaInNAs, the wavelength shift after anneal can be ascribed both to nitrogen out-diffusion and group III inter-diffusion. The latter could be more significant for GaInNAs layers than for InGaAs layers under similar conditions due to possibly elevated point defect densities associated with the growth of nitride-arsenide materials [76]. SIMS depth profiling (see Figure 56(a) and Figure 56(b)) shows that the nitrogen diffusion out of the QWs is more important than the diffusion of indium. Hence, the blue shift of the PL spectrum from GaInNAs QWs is predominantly due to out-diffusion of nitrogen. The extended spectrum (see Figure 56(c)) reveals the nitrogen background in the annealed sample is much higher than in the as-grown sample.

During this SIMS experiment, we have also noticed that diffusion of N_2 in GaAs is significant at the temperature used for anneal (760 °C). The extended spectrum features a big nitrogen spike at the surface tailing into the sample. This indicates that N_2 from the annealing environment is diffusing into the film. This diffusion from N_2 in GaAs is significant and has the same anomalous shape described above. The significance of this N_2 diffusion is demonstrated in Figure 57. The shift of the photoluminescence

spectrum during anneal can be limited by annealing in a N_2 ambient instead of an argon ambient. The N_2 ambient provides a competing source of nitrogen that reduces the nitrogen out-diffusion from the QW. While this decreased drop of nitrogen concentration in the QW reduces the emission wavelength shift, it would be desirable to prevent nitrogen out-diffusion from the QW during anneal.

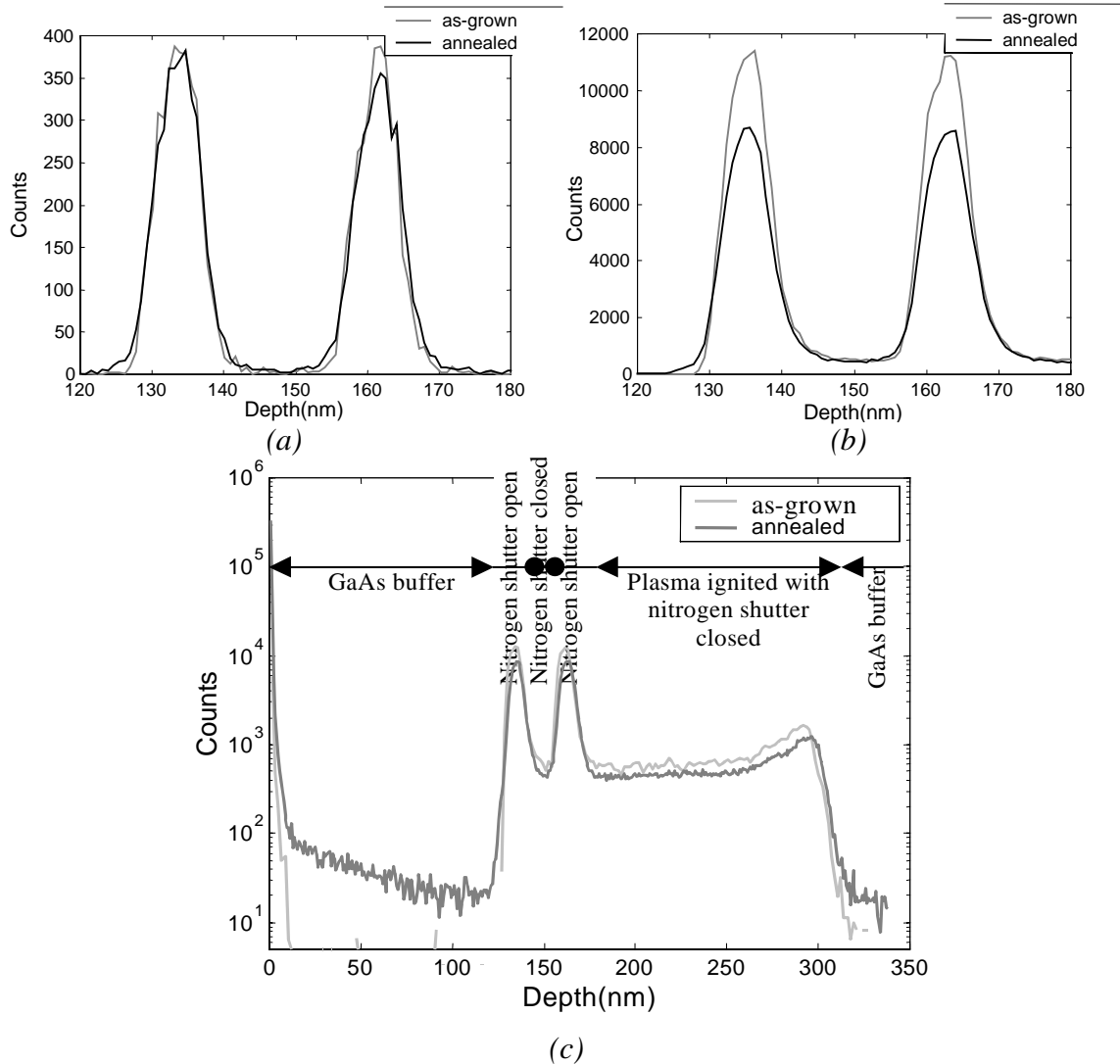


Figure 56: SIMS profile of (a) indium, (b) nitrogen and (c) nitrogen in 70\AA $Ga_{0.7}In_{0.3}N_{0.02}As_{0.98}/GaAs$ quantum wells with structure shown in Figure 45(a). The sample was proximity capped and annealed for 1 min at $760\text{ }^\circ\text{C}$ under N_2 ambient.

Figure 58 shows that the blue shift of the PL spectrum depends on the indium concentration. As expected from the presented model for nitrogen and arsenic interdiffusion through kick-out, a larger lattice parameter (i.e. more indium) results in more diffusion and hence greater shift in the emission spectra. The spectra are plotted

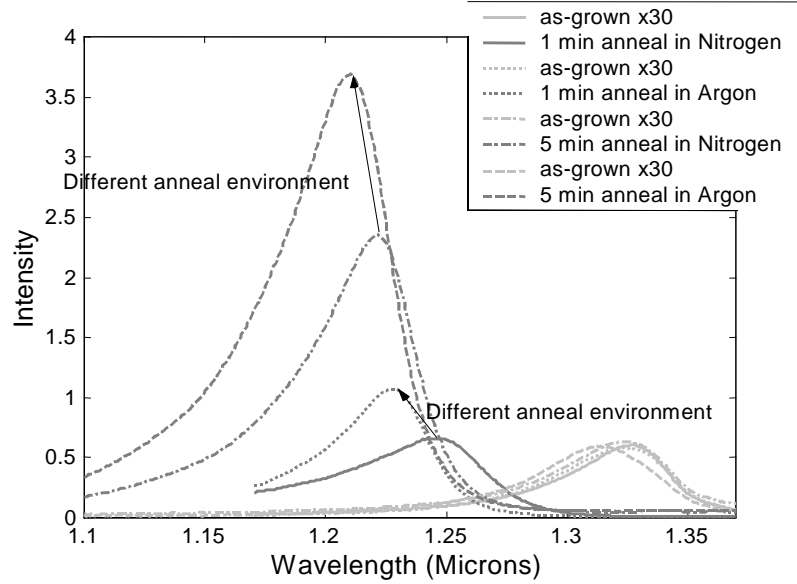


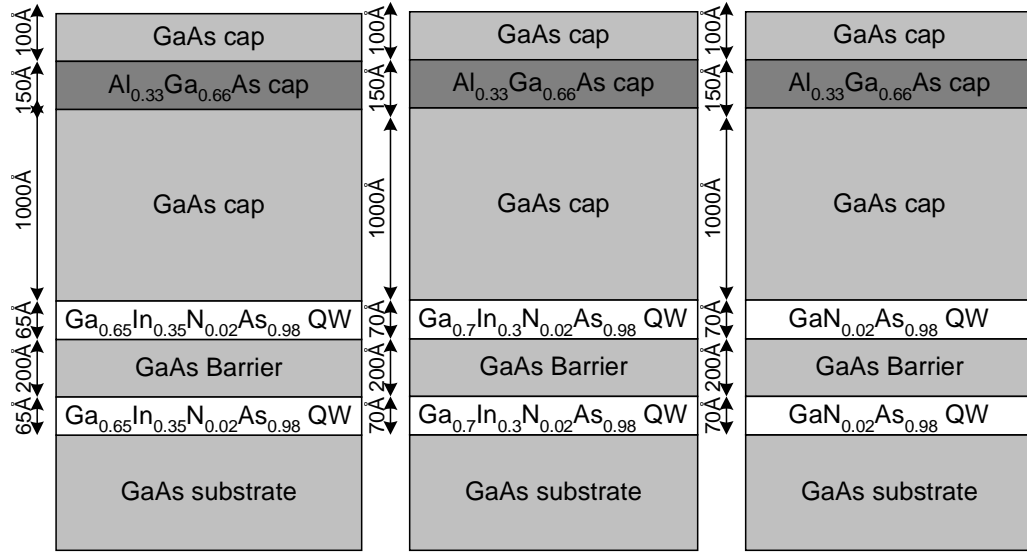
Figure 57: Photoluminescence spectrum of as-grown and annealed 70 \AA $\text{Ga}_{0.7}\text{In}_{0.3}\text{N}_{0.02}\text{As}_{0.98}$ QWs with GaAs barriers with structure shown in Figure 45(a). The samples were proximity capped and annealed for 1 min or 5 min at $760 \text{ }^\circ\text{C}$ under a N_2 or argon ambient.

with respect to energy because energy is a more direct measure for the properties of the QW than wavelength. Assuming a square quantum well with unchanged width, one can calculate (see section 3.2.2) that the nitrogen composition reduces from 1 at % to 0.61 at % for the $\text{Ga}_{0.65}\text{In}_{0.35}\text{N}_{0.02}\text{As}_{0.98}$ QW, from 1 at % to 0.675 at % for the $\text{Ga}_{0.7}\text{In}_{0.3}\text{N}_{0.02}\text{As}_{0.98}$ QW, and from 1 at % to 0.84 at % for the $\text{GaN}_{0.02}\text{As}_{0.98}$ QW. As the valence band energy barely changes when adding nitrogen to GaAs (see section 3.2.2), we assumed that only the conduction band offset and the bandgap energy change due to nitrogen diffusion. We used the effective mass of the closest InGaAs concentration because the effective mass of nitride-arsenides are unknown. The fact that the wavelength shift during anneal increases with indium composition makes achieving $1.3 \mu\text{m}$ emission by adding indium difficult. Comparison of QWs with 15 at % and 17.5 at % indium shows that the emission peak of the two samples after anneal is very close, despite a peak emission of the as-grown 17.5 at % indium QW at much longer wavelength than the as-grown 15 at % indium QW.

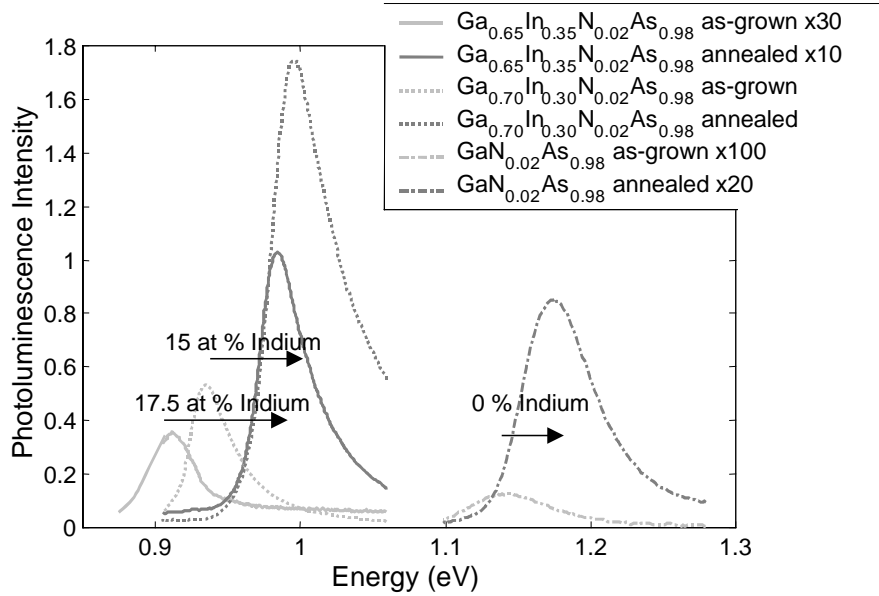
3.2.6 Conclusion

In this section on photoluminescence, we have shown that nitride-arsenides must be annealed to improve the luminescence efficiency. The same anneal also shifts the emission spectrum to shorter wavelengths. We have shown that as-grown nitride-

arsenide alloys contain interstitial nitrogen and that the interstitial nitrogen concentration is reduced after anneal. We have postulated that this interstitial nitrogen is the origin of the non-radiative recombination centers that disappear, at least partially, after anneal. We have also demonstrated that nitrogen and arsenic interdiffusion is responsible for the shift of the emission spectrum.



(a)



(b)

Figure 58: (a) Sample structure and (b) photoluminescence spectrum of as-grown and annealed GaInNAs QWs with GaAs barriers. The samples were proximity capped and annealed for 60 seconds at 760 °C under a N_2 ambient.

The fact that the shift of the emission spectrum and the increase of the luminescence efficiency occur simultaneously supports the described kick-out

mechanism for nitrogen and arsenic diffusion. Nitrogen diffusion and the resulting shift of the emission spectrum require the presence of interstitial nitrogen, which is a possible non-radiative recombination center decreasing the luminescence efficiency. We expect that the wavelength shift during the first stages of the anneal is faster as the interstitial nitrogen concentration is larger; once most of the interstitial nitrogen is annealed out and the peak luminescence intensity is reached, the shift occurs at a much slower rate.

We also showed that it is extremely difficult to get 1.3 μm emission from nitride-arsenides without major changes to the structure. To get the peak emission to longer wavelengths, one could add nitrogen or indium to the QW. But the addition of nitrogen results in a degradation of the optical properties. As the addition of indium increases the shift of the emission spectrum during the anneal necessary to get device quality material, the resulting emission spectrum after anneal is almost not shifted with respect to that of a sample with slightly lower indium composition.

3.3 Conclusion

This chapter has presented the optical properties of GaNAs and GaInNAs. Absorption measurements predicted a range of compositions yielding 1.3 μm emission. Photoluminescence measurements showed that nitride-arsenide alloys must be annealed to improve the luminescence efficiency. A typical annealing condition is a 1 minute anneal at 760°C, but shorter higher temperature or longer lower temperature anneals have the same effect. Unfortunately, this anneal shifts the emission spectrum to shorter wavelengths making 1.3 μm peak wavelengths hard to achieve after anneal. We have also shown that interstitial nitrogen is most likely responsible for both the non-radiative recombination in as-grown material and the fast diffusion of nitrogen during anneal. This diffusion of nitrogen also causes the blue shift in the emission spectrum after anneal.

Chapter 4: New active layer design enabling emission at 1.3 μm .

The previous chapter described the optical properties of nitride-arsenides. We have shown that 1.3 μm emission is hard to achieve because reasonable photoluminescence efficiency is only obtained after anneal, which also blue shifts the emission spectrum. The previous chapter also showed that the shift during anneal can be limited by providing a compensating source of nitrogen that reduces the nitrogen out-diffusion from the QWs.

Understanding the mechanism of this blue shift allows the design of a new active region enabling emission at 1.3 μm and beyond. We first demonstrate this new design using PL measurement. We then discuss the advantages of the new design. Finally, we demonstrate broad-area edge emitting lasers with this modified active region that emit at 1.3 μm and exhibit excellent thermal properties.

4.1 Photoluminescence from GaInNAs QWs with GaNAs and GaAs barriers

From section 3.2.5, it is clear that out-diffusion of nitrogen and the resulting shift of the emission spectrum can be reduced by supplying a source of nitrogen which limits the amount of nitrogen diffusing out of the QW. This can easily be done by modifying the active region, surrounding the GaInNAs QWs with GaNAs rather than GaAs barriers as shown in Figure 59(a). This provides a nitrogen source adjacent to the GaInNAs QWs that limits the nitrogen out-diffusion during anneal. The nitrogen concentration of the

barriers is fixed by the chosen nitrogen concentration of the QW; for our growth conditions, the nitrogen concentration is inversely proportional to the total group III growth rate (see section 2.3). When the gallium and the indium shutter are open (i.e. when growing $\text{In}_{0.35}\text{Ga}_{0.65}\text{As}$), the group III growth rate is 1.5 times the group III growth rate for growing GaAs. Hence, the nitrogen concentration in the barriers is 1.5 times higher than the nitrogen concentration in the QWs.

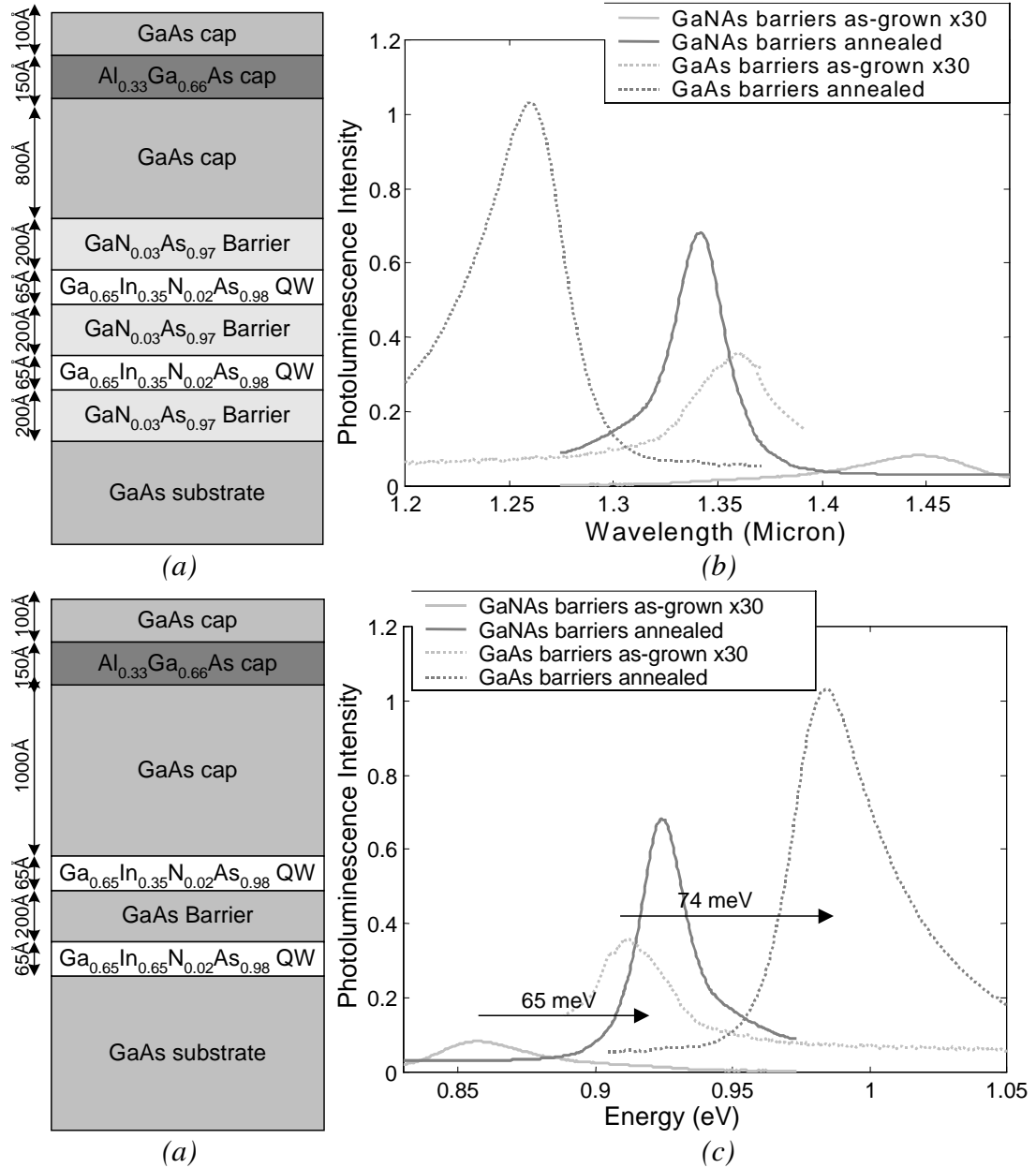


Figure 59: (a) Sample structure, (b) and (c) photoluminescence spectra of as-grown and annealed 65 Å $\text{Ga}_{0.65}\text{In}_{0.35}\text{N}_{0.02}\text{As}_{0.98}$ QWs with GaAs or GaNAs barriers. The samples were proximity capped and annealed for 60 seconds at 760 °C under a N_2 ambient.

Figure 59(b) shows that the photoluminescence occurs at significantly longer wavelengths when using GaNAs vs. GaAs barriers for the same nominal GaInNAs QW thickness and composition. The emission is at longer wavelengths for both the annealed and the as-grown samples. Even the annealed sample results in emission beyond 1.3 μm . However, the use of GaNAs barriers results in slightly lower photoluminescence efficiency for the as-grown sample. Figure 59(c) shows the same spectra as a function of energy because energy is a more direct measure for the properties of the QW. The shift of the emission spectrum during anneal is reduced from 74 meV to 65 meV when using GaNAs barriers instead of GaAs barriers.

4.2 Comparison of GaNAs and GaAs barriers

An obvious advantage of using GaNAs barriers is the ability to get emission from annealed material at 1.3 μm and beyond. Two effects are responsible for that:

1. The GaNAs barriers reduce the conduction band offset and therefore, reduce the confinement for electrons. This reduced electron confinement results in lower energy levels for electrons in the QW with finite barriers. As shown in Figure 43, the solutions for the wavevector k and the energy E decrease with decreasing electron confinement. This results in emission at longer a wavelength for the as-grown material (see Figure 60).
2. The GaNAs barriers are a source of nitrogen that reduces the total nitrogen out-diffusion from the QWs. The reduced nitrogen concentration drop in the QW during anneal decreases the shift of the peak emission energy during anneal from 74 meV to 65 meV, as shown in Figure 59(c).

Another advantage of the GaNAs barriers is the ability to grow strain compensated structures on GaAs substrates: GaNAs is tensilely strained on GaAs and the GaInNAs alloys are compressively strained on GaAs to maximize the gain (see section 1.1). When choosing the appropriate thickness for the layers, the overall structure has no macroscopic strain. The absence of macroscopic strain allows growing thicker structures without excessive lattice distortion or generation of misfit dislocations [77]. These thicker structures are necessary when fabricating detectors, modulators, and lasers with

higher light output power. The thickness of the GaNAs barriers compensating the strain of the 65 Å $\text{Ga}_{0.65}\text{In}_{0.35}\text{N}_{0.02}\text{As}_{0.98}$ QWs can be calculated as follows. The lattice parameter of the $\text{Ga}_x\text{In}_{1-x}\text{N}_y\text{As}_{1-y}$ QW with thickness t_{QW} can be calculated using Vegard's law as:

$$a_{\text{Ga}_x\text{In}_{1-x}\text{N}_y\text{As}_{1-y}} = (1-y)xa_{\text{GaAs}} + (1-y)(1-x)a_{\text{InAs}} + yxa_{\text{GaN}} + y(1-x)a_{\text{InN}}$$

When assuming that the $\text{Ga}_x\text{In}_{1-x}\text{N}_y\text{As}_{1-y}$ is not relaxed, the strain in this QW is defined as:

$$\varepsilon = \frac{a_{\text{Ga}_x\text{In}_{1-x}\text{N}_y\text{As}_{1-y}} - a_{\text{GaAs}}}{a_{\text{Ga}_x\text{In}_{1-x}\text{N}_y\text{As}_{1-y}}}$$

As the $\text{GaN}_z\text{As}_{1-z}$ barrier composition is related to the $\text{Ga}_x\text{In}_{1-x}\text{N}_y\text{As}_{1-y}$ QW composition:

$$z = \frac{y}{x},$$

the barrier thickness (for the case of 3 barriers and 2 QWs) should be:

$$t = \frac{2t_{\text{QW}}(ya_{\text{GaN}} + (x-y)a_{\text{GaAs}})((1-y)xa_{\text{GaAs}} + (1-y)(1-x)a_{\text{InAs}} + yxa_{\text{GaN}} + y(1-x)a_{\text{InN}} - a_{\text{GaAs}})}{3y(a_{\text{GaN}} - a_{\text{GaAs}})((1-y)xa_{\text{GaAs}} + (1-y)(1-x)a_{\text{InAs}} + yxa_{\text{GaN}} + y(1-x)a_{\text{InN}})}$$

This results in a thickness of 143 Å for the $\text{GaN}_{0.03}\text{As}_{0.97}$ barriers with 2 65 Å $\text{Ga}_{0.65}\text{In}_{0.35}\text{N}_{0.02}\text{As}_{0.98}$ QWs. Finally, it is worth mentioning that strain compensation only results in a structure without macroscopic stress when the compliances do not vary over the structure. Under this biaxial strain condition the in-plane stress is equal to:

$$\sigma = \frac{(C_{11} + 2C_{12})(C_{11} - C_{12})}{C_{11}} \varepsilon.$$

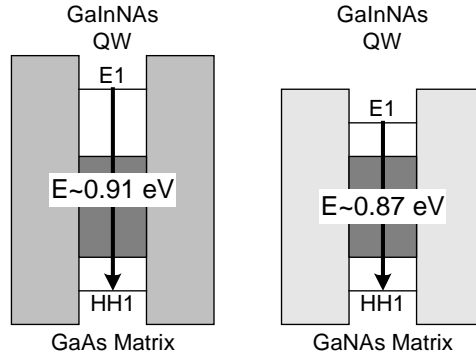


Figure 60: Schematic of the QW structure for (a) GaAs and (b) GaNAs barriers.

A disadvantage of GaNAs barriers over GaAs barriers is that the photoluminescence efficiency of an annealed sample with GaNAs barriers is slightly lower compared to an annealed sample with GaAs barriers (see Figure 59(b) and (c)). This can be due to the trapping of carriers at defects associated with nitrogen in the barriers or due to reduced electron confinement caused by the decreased conduction band offset.

By replacing the GaAs barriers with GaNAs barriers, the electron confinement is reduced and the thermal properties of lasers based on GaInNAs QWs are changed. In section 1.1 we explained that one of the advantages of the GaInNAs material system over the GaInPAs material system is the increased conduction band offset between GaInNAs and GaAs resulting in a better electron confinement and better thermal performance of GaInNAs lasers. When using GaNAs vs. GaAs barriers the conduction band offset is reduced and the electrons seem less confined. However, it is still possible to embed this modified active region within a larger confined structure with GaAs barriers. As such the thermal properties might not deteriorate. The thermal performance of this structure will be studied in section 4.3.

4.3 Broad area edge-emitting laser at 1.3 μm using GaNAs barriers

4.3.1 Introduction broad area edge-emitting laser operation

The structure of a broad area laser has briefly been introduced in section 1.2.1. It consists of a hetero-structure laser diode that confines electrons and holes in the QW region, lower index cladding layers to provide an optical waveguide, and cleaved-facet mirrors that provide photon feedback. The epitaxial layer structure typically has dimensions of a few microns.

A good overview on characterization of broad area edge-emitting lasers is given in [78]. The most fundamental characteristic of a diode laser is the light output power versus input current (L-I) characteristic. From a measured L-I characteristic one can immediately determine the experimental threshold current, I_{th} , from the intercept of the threshold curve with the abscissa (see Figure 61). High quality devices do not need a lot

of current to achieve inversion and the threshold current is small. The differential quantum efficiency, which is related to the fraction of the current that generates carriers in the active region, the reflectivity of the mirrors, and the loss of the optical wave, can be calculated from the slope of the curve above threshold. By measuring the L-I characteristic of lasers with different length, these important parameters can be determined.

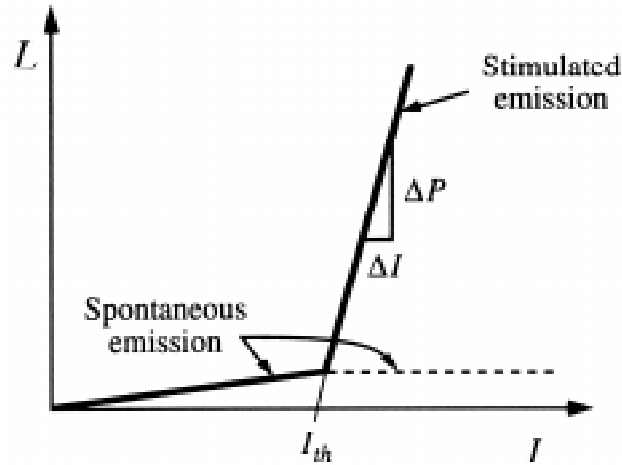


Figure 61: Illustration of output power vs. current for a diode laser (L-I curve). Below threshold only spontaneous emission is important; above threshold the stimulated emission power increases while the spontaneous emission is clamped at its threshold value [78].

4.3.2 Description of laser structure and room temperature performance

The new active region design was incorporated into a broad area edge-emitting laser. The emission spectrum, the light output versus input current, and the thermal properties were measured. The structure of the broad area laser is shown in Figure 62(a). The separate confinement for the photons is achieved by surrounding the GaNAs with GaAs and the GaAs with top and bottom 2 μm thick AlGaAs cladding layers with a lower index of refraction than the rest of the structure. The active region is effectively annealed in-situ during the growth of the top cladding layer as AlGaAs must be grown at high temperature to avoid incorporation of oxygen impurities. The growth temperature of this cladding was 720 $^{\circ}\text{C}$. The upper cladding is p-doped and the bottom cladding is n-doped to achieve a p-i-n hetero-structure diode. The tested device is 800 μm long and 20 μm wide.

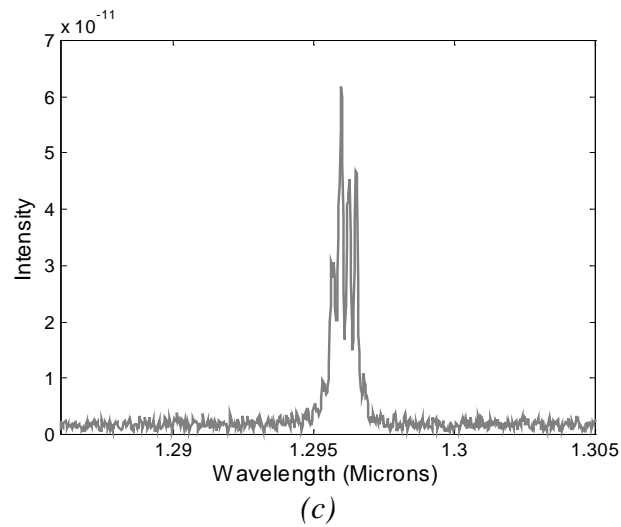
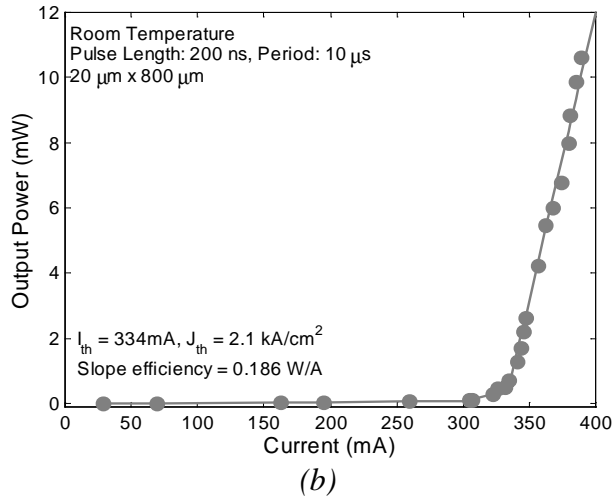
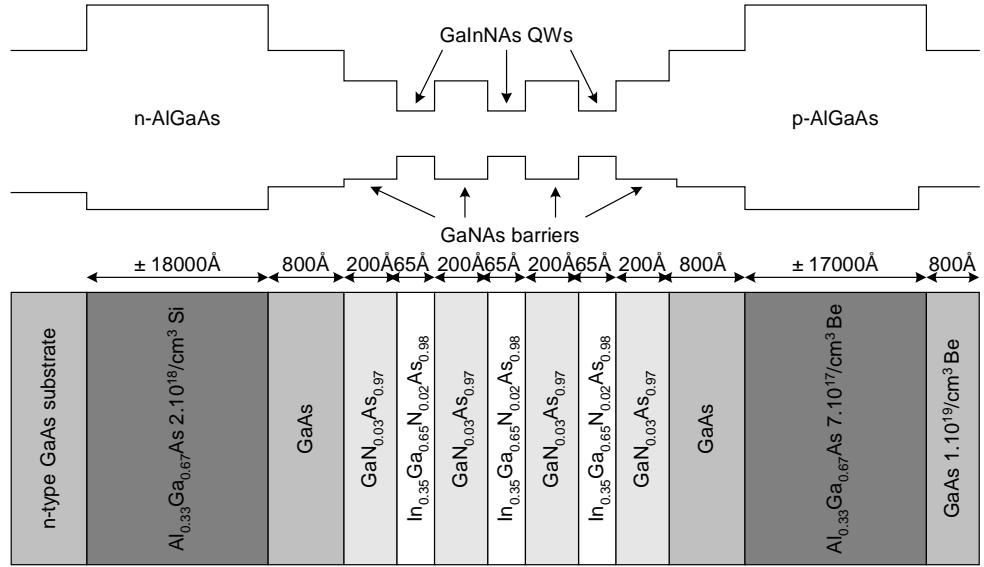


Figure 62: (a) Structure, (b) L-I curve and (c) emission spectrum of a broad area edge-emitting laser with GaNAs barriers and GaInNAs QWs.

The L-I curve and the emission spectrum of this device are given in Figure 62(b) and Figure 62(c). This device lases at 1.3 μm . The emission peak from broad area lasers with the same QWs and GaAs barriers was around 1.25 μm [26]. The emission wavelength of the laser is still shorter than the emission wavelength of the corresponding PL sample because the anneal during the growth of the upper cladding layer was much longer than the RTA anneal of the PL sample. As expected from the lower photoluminescence efficiency (see section 4.1) the threshold current density of this device is slightly higher than the threshold current density of the laser with the same QW composition but GaAs barriers; the threshold current density of this last device was approximately 2 kA/cm^2 .

4.3.3 Thermal properties of broad area edge-emitting laser with GaNAs barriers

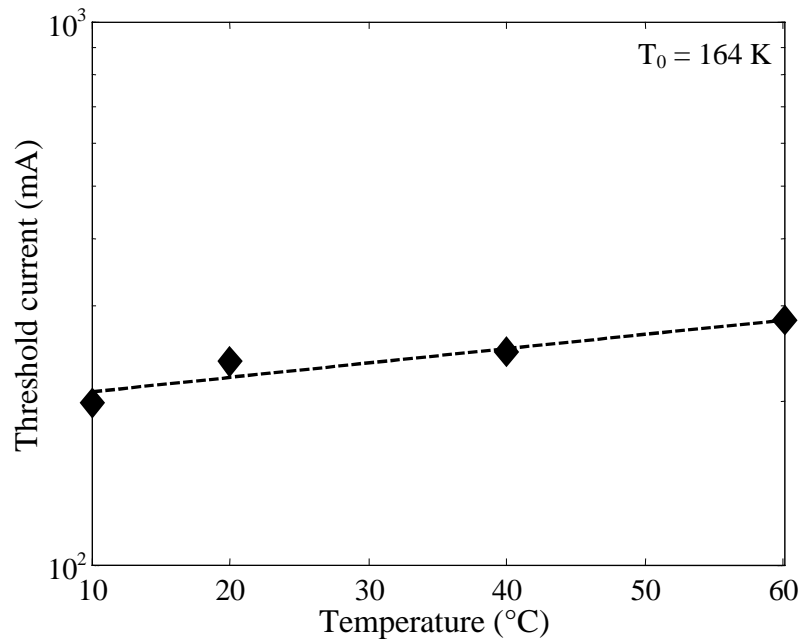


Figure 63: Threshold current as function of temperature for the device shown in Figure 62(a). The measured value for T_0 is 164 K.

The thermal performance of lasers is characterized by their increase in threshold current, I_{th} , versus temperature from the following expression:

$$I_{\text{th}}(T) = I_{\text{th}}(300^\circ\text{K}) \exp(T/T_0)$$

T_0 -measurements on the broad area laser with GaNAs barriers are shown in Figure 63. The T_0 is 164 K (while the lasers with GaAs barriers have a T_0 of 105 K [26]). The structure with GaNAs barriers and GaAs surrounding the GaNAs barriers might have

better thermal performance because the probability of an electron traveling across the QW without getting trapped is reduced when there is a significantly wider secondary well GaNAs region surrounding the QWs in which electrons get captured.

4.4 Conclusion

A structure consisting of GaNAs barriers with GaInNAs QW allows fabrication of devices emitting at 1.3 μm . The decreased conduction band offset and the decreased nitrogen out-diffusion from the QWs during anneal enabled this emission at longer wavelength. We also demonstrated that broad area lasers with this modified active region have superior thermal properties.

Chapter 5: Summary and Future Work

5.1 Summary

Semiconductor materials emitting at 1.3 μm have important applications in optoelectronic devices for metropolitan-area and data communication networks. We have shown that GaInNAs alloys have tremendous potential in this field because they can be grown on GaAs substrates and can hence benefit from the well developed AlAs/GaAs distributed Bragg reflector (DBR) technology.

We have developed the MBE growth of nitride-arsenides and demonstrated that MBE is currently the most suitable deposition technique to grow these alloys. The nitrogen composition control is robust and phase segregation is easy to avoid. The optimization of the rf plasma operation is critical to realize materials useful for optoelectronics.

We predicted a range of compositions for GaInNAs alloys yielding 1.3 μm emission. Nitride-arsenides must be annealed to achieve the luminescence efficiency necessary for optoelectronic devices. Unfortunately, this anneal also shifts the emission to shorter wavelengths which makes 1.3 μm emission hard to achieve. We have shown that interstitial nitrogen is most likely responsible for the non-radiative recombination in as-grown material and the significant blue shift due to the fast diffusion of nitrogen.

We were able to build devices emitting at 1.3 μm by surrounding the GaInNAs QWs with GaNAs barriers.

5.2 Suggestions for future work

We have shown that GaInNAs alloys have tremendous potential in the field of data communication and metropolitan area communication. As is the case for many research projects developing new technologies, this one has created more interesting questions than it has solved and generated many avenues for future investigations. There are four broad areas in which more work can be done: growth, characterization, simulation, and devices.

5.2.1 Exploring the growth of nitride-arsenides

There is certainly room to improve the MBE growth of nitride-arsenides. Two issues need work: avoiding interstitial nitrogen incorporation to improve luminescence efficiency and limiting the amount of nitrogen bypassing the shutter to avoid defects associated with the incorporation of non-atomic nitrogen species. Further progress may be made by careful control of substrate temperature, use of surface surfactants, improved plasma ignition and operation. PL, DLTS, NRA can be used to characterize effects from these changes. These improvements may even allow emission out to 1.55 μm from nitride-arsenides.

Another interesting topic related to the growth of nitride-arsenides is ordering. Ordering in GaInAsP alloys has been studied extensively. TEM, XRD, Raman, and RHEED can be used to verify if the same ordering mechanisms occur in GaInNAs alloys.

Most of commercial opto-electronic devices are grown by MOCVD because it allows higher throughput. Therefore, it might well be that commercialization of nitride-arsenides will go hand in hand with the ability to grow them by MOCVD. This development of MOCVD growth of nitride-arsenides has already proven to be difficult and requires significant work to be successful.

5.2.2 Investigating the properties of nitride-arsenides

In terms of characterization, there are also many challenges.

The final word about nitrogen interstitials is not yet said. TEM, XRD, and NRA can be used to determine the exact nature and position of the interstitial nitrogen species.

It would also be interesting to determine some of the fundamental properties of this new alloy system: going from electrical properties and optical properties to mechanical properties and thermal properties. Some issues have already surfaced. A major debate is going on about the electron mobility in nitride-arsenides. Alloy scattering may be more important when mixing occurs on the group V-sublattice. During this research, we also noticed silicon is not an effective n-type dopant for nitride-arsenides.

An important area in which little research has been done so far is evaluation of the long term stability and reliability of nitride-arsenides. This research will be necessary to enable application of nitride-arsenides in commercial devices in optical networks.

5.2.3 Contributing to better understanding of nitride-arsenides through computer simulation

As mentioned in the introduction, the nitride-arsenides are an unique III-V material system because the significant size and electro-negativity differences between nitrogen and arsenic atoms. There is great opportunity for simulation research in this new material system: incorporation dynamics of the nitrogen, more accurate prediction of electrical, optical, thermal, mechanical properties, as well as others.

5.2.4 Building opto-electronic devices operating at 1.3 μm

Finally, our development of GaInNAs emitting at 1.3 μm has opened the playground for electrical engineers wanting to make opto-electronic devices (VCSELS, tunable VCSELS, modulators, waveguide devices, anti-resonant reflective optical waveguide (ARROW) devices...) with 1.3 μm active regions on GaAs substrates. GaAs technology enables the fabrication of a huge range of devices based on quarter wave distributed Bragg reflectors (DBRs), which can only be reasonably achieved in GaAs/AlAs alloys. It is expected that these micromachined opto-electronic devices will be promising components in future communications systems.

Chapter 6: References

- [1] M. Weyers, M. Sato, and H. Anod, “Red shift of photoluminescence and absorption in dilute GaAsN alloy layers”, *Jpn. J. Appl. Phys.*, Vol. 31 (1992), p. L853-855.
- [2] S. Wei, and A. Zunger, “Giant and composition-dependent optical bowing coefficient in GaAsN alloys”, *Phys. Rev. Lett.*, Vol. 76 (1996), p. 664-667.
- [3] J. Neugebauer, and C. G. Van de Walle, “Electronic structure and phase stability of GaAs_{1-x}N_x alloys”, *Phys. Rev. B*, Vol. 51 (1995), p. 10568-10571.
- [4] S. L. Chuang, “Physics of optoelectronic devices”, John Wiley & Sons Inc., 1995, p. 85-97,227,339-340,372,440-445,710.
- [5] M. Kondow, K. Uomi, A. Niwa, T. Kitatani, S. Watahiki, Y. Yazawa, “GaInNAs: A novel materials for long-wavelength-range laser diodes with excellent high-temperature performance”, *Jpn. J. Appl. Phys.*, Vol. 35 (1996), p. 1273-1275.
- [6] P. Krispin, S. G. Spruytte, J. S. Harris, and K. H. Ploog, “Electrical depth profile of p-type GaAs/Ga(As, N)/GaAs heterostructures determined by capacitance–voltage measurements”, *J. Appl. Phys.*, Vol. 88 (2000), p. 4153-4158.
- [7] I. Ho, and G. B. Stringfellow, “Solubility of nitrogen in binary III-V systems”, *J. Cryst. Growth*, Vol. 178 (1997), p. 1-7.
- [8] K. S. Giboney, L. R. Aronson, and B. E. Lemoff, “The ideal light source for datanets”, *IEEE Spectrum*, Vol. 35 (1998), p. 43-53
- [9] J. Walrand, “Communication networks: A first course”, WCB/McGraw-Hill (1998), p. 215.
- [10] E.A. Lee, and D. G. Messerschmitt, “Digital communication”, Kluwer Academic Publishers (1994), p. 132.

- [11] L. Kazovsky, S. Benedetto, A. Willner, “Optical fiber communication systems”, Artech House, Inc. (1996), p. 40.
- [12] G. Patriarche, F. Jeannès, J.-L. Oudar, and F. Glas, “Structure of the GaAs/InP interface obtained by direct wafer bonding optimised for surface emitting optical devices”, *J. Appl. Phys.*, Vol. 82 (1997), p.4892-4903.
- [13] L. Goldstein, C. Fortin, C. Starck, A. Plais, J. Jacquet, J. Boucart, A. Rocher, and C. Poussou, “GaAlAs/GaAs metamorphic Bragg mirror for long wavelength VCSELs”, *Electron. Lett.*, Vol. 34 (1998), p. 268-270.
- [14] S. Uchiyama, and S. Kashiwa, “GaInAsP/InP SBH surface emitting lasers with Si/Al₂O₃ mirror”, *Electron. Lett.*, Vol. 31 (1995), p. 1449-1451.
- [15] G. Almuneau, F. Genty, L. Chusseau, N. Bertru, B. Fraisse, and J. Jacquet, ‘Molecular beam epitaxy growth of 1.3 μm high-reflectivity AlGaAsSb/AlAsSb Bragg mirror”, *Electron. Lett.*, Vol. 33 (1997), p. 1226-1227.
- [16] G. B. Stringfellow, “Organometallic vapor-phase epitaxy: theory and practice”, Boston: Academic Press (1989), p. 66-75,123.
- [17] C.-E. Zah, R. Bhat, B. N. Pathak, F. Favire, W. Lin, M. C. Wang, N. C. Andeadakis, D. M. Hwang, M. A. Koza, T.-P. Lee, Z. Wang, D. Darby, D. Flanders, and J.J. Hsieh, “High-performance uncooled 1.3- μm Al_xGa_yIn_{1-x-y}As/InP strained-layer quantum-well lasers for subscriber loop applications”, *IEEE J. Quantum Electron.*, Vol. 30 (1994), p. 511-521.
- [18] A. E. Zhukov, V. M. Ustinov, A. R. Kovsh, A. Y. Egorov, N. A. Maleev, N. N. Ledentsov, A. F. Tsatsul’nikov, M. V. Maximov, Y. G. Musikhin, N. A. Bert, “Control of the emission wavelength of self-organized InGaAs Quantum Dots: main achievements and present status”, *Semicond. Sci. Technol.*, Vol. 14 (1999), p. 575-581.
- [19] G. Ungaro, G. Le Roux, R. Teissier, and J.C. Harmand, “GaAsSbN: a new low-bandgap material for GaAs substrates”, *Electron. Lett.*, Vol. 35 (1999), p. 1246-1248.
- [20] C. H. P. Lupis, “Chemical thermodynamics of materials”, Elsevier Science Publishing Co., Inc. (1983), p. 76-82.
- [21] K. H. Hellewege, O. Madelung, M. Schulz, and H. Weiss, “Landolt-Börnstein numerical data and functional relationships in science and technology, New Series,

- Group III: Crystal and solid state physics, Physics of group IV elements and III-V compounds”, Vol. 17a, Springer-Verlag (1982), p. 350,181-183,218,234,237-238,248,278-280,297,300,302,306, Vol 17d, p. 16.
- [22] J. C. Bailar, H. J. Emeleus, R. Nyholm, and A. F. Trotman-Dickenson, “Comprehensive inorganic chemistry”, Pergamon Press (1973), p. 159,555-556.
- [23] J. R. Arthur, ”Interaction of Ga and As₂ molecular beams with GaAs surfaces”, *J. Appl. Phys.*, Vol. 39 (1968), p. 4032-4034.
- [24] A. Y. Cho, and J. R. Arthur, “Molecular beam epitaxy”, *Progress in Solid-State Chemistry*, Vol. 10 (1975), p. 157-191.
- [25] M. A. Herman, and H. Sitter, “Molecular beam epitaxy: Fundamentals and current status”, Springer-Verlag (1982), p 186,305-313.
- [26] C. W. Coldren,” Group III-nitride-arsenide laser diodes grown by elemental source molecular beam epitaxy”, Ph. D. Thesis.
- [27] M. H. Hablani, “High-vacuum technology: a practical guide”, Marcel Dekker, Inc (1997), p. 319-321,533.
- The vapor pressure of N₂ at 77 K (the cryoshroud temperature) is significant compared to the pressure of CO, O₂, As₄, H₂O, In, Ga, and Al.
- [28] G. C. Osbourn, “Strained-layer superlattices from lattice mismatched materials,” *J. Appl. Phys.*, Vol. 53 (1982), p. 1586-1589.
- [29] J. W. Matthews and A. E. Blakeslee, "Defects in epitaxial multilayers. I. Misfit dislocations", *J. Cryst. Growth*, Vol. 27 (1974), p. 118-125.
- [30] R. Hull, and J. C. Bean, “Misfit dislocations in lattice-mismatched epitaxial films”, *CRC Solid State and Mat. Science*, Vol. 17 (1992), p. 507-546.
- [31] V. Kirchner, H. Heinke, U. Birkle, S. Einfeldt, D. Hommel, H. Selke, and P.L. Ryder, "Ion-induced crystal damage during plasma-assisted MBE growth of GaN layers", *Phys. Rev. B*, Vol 58 (1998), p.15749-15755.
- [32] R. M. Park, “Low-resistivity p-type ZnSe:N grown by molecular beam epitaxy using a nitrogen free-radical source”, *J. Vac. Sci. Technol. A*, Vol. 10 (1992), p. 701-704.
- [33] R. R. LaPierre, B. J. Robinson, and D. A. Thompson, “Group V incorporation in InGaAsP grown on InP by gas source molecular beam epitaxy”, *J. Appl. Phys.*, Vol. 79 (1996), p. 3021-3027.

- [34] T. L. Lee, J. S. Liu, and H. H. Lin, "Incorporation of group V elements in $\text{Ga}_x\text{In}_{1-x}\text{As}_y\text{P}_{1-y}$ grown by gas source molecular beam epitaxy", *J. Electron. Mater.*, Vol. 25 (1996), p. 1469-1473.
- [35] B.E. Warren, "X-Ray diffraction", Dover Publication, Inc. (1990), p. 18-21.
- [36] K. T. Faber, and K. J. Malloy, "The mechanical properties of semiconductors, semiconductors and semimetals Volume 37", Academic press, Inc. (1992), p. 31.
- [37] P. F. Fewster, and C. J. Curling, "Composition and lattice-mismatch measurements of thin semiconductor layers by x-ray diffraction", *J. Appl. Phys.*, Vol. 62 (1987), p. 4154-4158.
- [38] J. C. Vickerman, "Surface analysis: The principal techniques", John Wiley & Sons (1997), p.106-108,188-189,215-266.
- [39] L. G. Ferreira, S. H. Wei, and A. Zunger, "First principles calculation of alloy phase diagrams: the renormalized-interaction approach", *Phys. Rev. B*, Vol. 40 (1989), p. 3197-3231.
- [40] J. Y. Tsao, "Materials fundamentals of molecular beam epitaxy", Academic press, Inc. (1993), p. 49-56, 93-149.
- [41] G. B. Stringfellow, "Calculation of regular solution interaction parameters in semiconductor solid solutions", *J. Phys. Chem. Solids*, Vol. 34 (1973), p. 1749-1750.
- [42] V.A. Elyukhin, and S. A. Nikishin, "Internal stress and superstructures in $\text{GaAs}_x\text{N}_{1-x}$ solutions", *Tech. Phys. Lett.*, Vol. 21 (1995), p. 695-696.
- [43] Y. Qui, S. A. Nikishin, H. Temkin, N. N. Faleev, and Y. A. Kudriavtsev, "Growth of single phase $\text{GaAs}_{1-x}\text{N}_x$ with high nitrogen concentration by metal-organic molecular beam epitaxy", *Appl. Phys. Lett.*, Vol. 70 (1997), p. 3242-3245.
- [44] Y. Qui, S. A. Nikishin, H. Temkin, V. A. Elyukhin, and Y. A. Kudriavtsev, "Thermodynamic considerations in epitaxial growth of $\text{GaAs}_{1-x}\text{N}_x$ solid solutions", *Appl. Phys. Lett.*, Vol 70 (1997), p. 2831-2833.
- [45] D. R. Lide, "CRC Handbook of chemistry and physics", CRC Press (1996), p. 5-2-5-21.
- [46] A. S. Jordan, and M. Ilegems, "Solid-liquid equilibria for quaternary solid solutions involving compound semiconductors in the regular solution approximation", *J. Electrochem. Soc.*, Vol. 119 (1972), p. 123-124.

- [47] M. Ilegems, and M. B. Panish, "Phase equilibria in III-V quaternary systems-application to Al-Ga-P-As", *J. Phys. Chem. Solids*, Vol.35 (1974), p. 409-20.
- [48] I. Ho, and G. B. Stringfellow, "Solid phase immiscibility in GaInN", *Appl. Phys. Lett.*, Vol. 69 (1996), p. 2701-2703.
- [49] M. B. Panish, and M. Ilegems, "Phase equilibria in ternary III-V systems", *Prog. Solid State Chem.*, Vol. 7 (1972), p. 39-83.
- [50] R. D. Jones, and K. Rose, "Liquidus calculations for III-N semiconductors", *Calphad*, Vol. 8 (1984), p. 343-354.
- [51] S. B. Zhang, and A. Zunger, "Surface-reconstruction-enhanced solubility of N, P, As, and Sb in III-V semiconductors", *Appl. Phys. Lett.*, Vol. 71 (1997), p. 677-679.
- [52] Z. Z. Bandic, R. J. Hauenstein, M. L. O'Steen, and T. C. McGill, " Kinetics of nitrogen in GaAsN layers during GaAs overgrowth", *Mat. Res. Soc. Symp. Proc.*, Vol. 449 (1997), p. 209-214.
- [53] J. W. Cahn, "On spinodal decomposition in cubic crystals", *Acta Metall.*, Vol. 10 (1962), p. 179-183.
- [54] R. E. Nahory, M. A. Polack, E. D. Beebe, J. C. DeWinter, and M. Ilegems, "The liquid phase epitaxy of $\text{Al}_y\text{Ga}_{1-y}\text{As}_{1-x}\text{Sb}_x$ and the importance of strain effects near the miscibility gap", *J. Electrochem. Soc.*, Vol. 125 (1978), p.1053-1058.
- [55] D. Schlenker, T. Miyamoto, Z. Pan, F. Koyama, K. Iga, "Miscibility gap calculation for $\text{Ga}_{1-x}\text{In}_x\text{N}_y\text{As}_{1-y}$ including strain effects", *J. Cryst. Growth*, Vol 196 (1999), p. 67-70.
- [56] M. Ichimura, and A. Sasaki, "Short-range order in III-V ternary alloy semiconductors", *J. Appl. Phys.*, Vol 60 (1986), p. 3850-3855.
- [57] A. Ougazzaden, Y. Le Bellego, E. V. K. Rao, M. Juhel, L. Leprince, and G. Patriarche, "Metal organic vapor phase epitaxy growth of GaAsN on GaAs using dimethylhydrazine and tertiary butylarsine", *Appl. Phys. Lett.*, Vol. 70 (1997), p. 2861-2863.
- [58] H. Saito, T. Makimoto, N. Kobayashi, "MOVPE growth of strained InGaAsN/GaAs quantum wells", *J. Cryst. Growth*, Vol. 195 (1998), p. 416-420.
- [59] F. Höhnsdorf, J. Koch, C. Agert, and W. Stolz, "Investigations of (GaIn)(Nas) bulk layers and (GaIn)(Nas)/GaAs multiple quantum well structures grown using

- tertiarybutylarsine (TBAs) and 1,1-dimethylhydrazine (UDMHy)", *J. Cryst. Growth*, Vol. 195 (1998), p. 391-396.
- [60] M. Weyers, M. Sato, "Growth of GaAsN alloys by low-pressure metalorganic chemical vapor deposition using plasma-cracked NH₃", *Appl. Phys. Lett.*, Vol. 62 (1993), p. 1396-1398.
- [61] J. I. Pankove, "Optical processes in semiconductors", Dover Publications, Inc. (1971), p. 104.
- [62] R. K. Willardson, and A. C. Beer, "Semiconductors and semimetals Volume 8 Transport and optical phenomena", Academic press (1972), p. 200-207,229-238.
- [63] M. D. Sturge, "Optical absorption of gallium arsenide between 0.6 and 2.75 eV", *Phys. Rev.*, Vol. 127 (1962), p. 768-773.
- [64] B. M. Clemens, "Coursenotes for MSE 325", Fall 1999, p.98
- [65] C. R. Brundle, C. A. Evans, S. Wilson, "Encyclopedia of materials characterization", Butterworth-Heinemann (1992), p. 375.
- [66] D. A. Miller, "Coursenotes for MSE 243", Winter 1998, p. 64.
- [67] E. V. Rao, A. Ougazzaden, Y. Le Bellego, and M. Juhel, "Optical properties of low band gap GaAs_(1-x)N_x layers: Influence of post-growth treatments", *Appl. Phys. Lett.*, Vol 72 (1998), p. 1409-1411.
- [68] H. P. Xin, K. L. Kavanagh, M. Kondow, and C. W. Tu, "Effects of rapid thermal annealing on GaInNAs/GaAs multiple quantum wells", *J. Cryst. Growth*, Vol. 201-202 (1999), p. 419-22.
- [69] P. Blood and J. W. Orton, "The electrical characterization of semiconductors: majority carriers and electron states", Academic press (1992).
- [70] H. P. Xin, C. W. Tu, and M. Geva, "Annealing behavior of p-type Ga_{0.892}In_{0.108}N_xAs_{1-x} (0≤x≤0.024) grown by gas-source molecular beam epitaxy", *Appl. Phys. Lett.*, Vol. 75 (1999), p. 1416-1418.
- [71] J. F. Geisz, D. J. Friedman, J. M. Olson, S. R. Kurtz, and B. M. Keyes, "Photocurrent of 1 eV GaInNAs lattice-matched to GaAs", *J. Cryst. Growth*, Vol. 195 (1998), p. 401-408.
- [72] A. A. Allerman, S. R. Kurtz, E. D. Jones, N. R. Modine, R. M. Sieg, "InGaAsN for high efficiency solar cells", MRS Fall meeting 1999 Boston, OO3.8.

- [73] T. Miyamoto, T. Kageyama, S. Makino, D. Schlenker, F. Koyama, K. Iga, "CBE and MOCVD growth of GaInNAs", *J. Cryst. Growth* (2000), Vol. 209, p. 339-344.
- [74] G. Terwagne, D. D Cohen, G. A. Collins, "Cross-section measurement of the $^{14}\text{N}(^3\text{He},\text{p})^{16}\text{O}$ and $^{14}\text{N}(^3\text{He},\alpha)^{13}\text{N}$ reactions between 1.6 and 2.8 MeV", *Nucl. Instrum. Methods B*, Vol. 84 (1994), p. 415-420.
- [75] G. Bösker, N. A. Stolwijk, J. V. Thordson, U. Södervall, and T. G. Andersson, "Diffusion of nitrogen from a buried doping layer in gallium arsenide revealing the prominent role of As interstitials", *Phys. Rev. Letters*, Vol. 81 (1998), p. 3443-3446.
- [76] N. Yamada, and J. S. Harris, "Strained InGaAs/GaAs single quantum well lasers with saturable absorbers fabricated by quantum well intermixing", *Appl. Phys. Lett.*, Vol. 60 (1992), p. 2463-2465.
- [77] K. Hiramoto, M. Sagawa, T. Toyonaka, "Strain-compensation effect on the reduction of lattice distortion in InGaAs/(In)GaAs(P) strained quantum-well structures on GaAs substrates", *Jpn. J. Appl. Phys.*, Vol.36 (1997), p. L1632-1633.
- [78] L. A. Coldren, and S. W. Corzine, "Diode lasers and photonic integrated circuits", John Wiley and Sons (1995), p. 52-54.